TECHNISCHE
UNIVERSITÄT
WIEN
Vienna University of Technology

THESIS

Innovative measurement of solids residence time distribution in circulating fluidized beds – application to a cold flow model

ausgeführt zum Zwecke der Erlangung des akademischen Grades eines

Diplom-Ingenieurs

unter der Leitung von

Univ. Prof. Dipl.-Ing. Dr. Hermann Hofbauer

Dipl.-Ing. Dr. Tobias Pröll

Dipl.-Ing. Diana Carolina Guío Pérez

Institut für Verfahrenstechnik, Umwelttechnik und Technische Biowissenschaften

eingereicht an der Technischen Universität Wien

Fakultät für Maschinenwesen und Betriebswissenschaften

von

Simon Hinterhuber

Matr. Nr.: 0526217

Malfattigasse 18/21

1120 Wien

Wien, am (Simon Hinterhuber)

DANKSAGUNG

An dieser Stelle möchte ich beim Institut für Verfahrenstechnik, Umwelttechnik und Technische Biowissenschaften und ganz besonders bei Univ. Dipl.-Ing. Dr. techn. Hermann Hofbauer für die Ermöglichung dieser Diplomarbeit bedanken.

Meinem Betreuer Dipl.-Ing. Dr. techn. Tobias Pröll möchte ich ebenfalls für die richtungsweisenden und hilfreichen Ratschläge danken, welche er mir immer zum richtigen Zeitpunkt mitgab.

Für die gute Zusammenarbeit und stete Unterstützung bedanke ich mich bei Dipl.-Ing. Diana Carolina Guío Pérez sehr herzlich, die mir neue Einblicke in das wissenschaftliche Arbeiten gab, wodurch ich viel dazulernen konnte.

Ebenso möchte ich auch ganz besonders den Kollegen der Arbeitsgruppe Zero Emission Technologies danken, die mir bei ganz spontanen Fragenstellungen immer wieder weitergeholfen haben. Danke für die schöne Arbeitsatmosphäre ☺

Ich möchte mich ebenfalls bei Ao.Univ.Prof. Dipl.-Ing. Dr.techn. Johann Wassermann und seinem Team für die Unterstützung bei der Signalverarbeitung recht herzlich bedanken.

Ganz besonders möchte ich mich bei meinen Eltern bedanken, die mir das langjährige Studium überhaupt erst ermöglichten und bei meinen Großeltern, die mich ebenfalls immer wieder unterstützten, vielen Dank!

Last but not least möchte ich mich bei meiner sehr geduldigen, mich immer unterstützenden Freundin De´ Yahira bedanken. Ohne ihr mentales Gut-Zureden würde ich heute noch an der Diplomarbeit schreiben ☺

ABSTRACT

Chemical looping combustion (CLC) is a novel combustion process based on fluidized bed technology. A CLC power plant (120 kW) was built at Vienna University of Technology. The main parts of the CLC plant are two tubular reactors (the so called air and fuel reactor) and two cyclones. The reactors operate as fluidized beds and are connected by means of a lower and an upper loop seal to avoid a gas exchange between the reaction zones. A metal oxide (bed inventory) is circulated between the air reactor (AR) and the fuel reactor (FR). In the latter reactor, the metal oxide is reduced by methane (fluidization fluid), leading to the main gaseous products H_2O and CO_2 in the case of full conversion. The gas stream is separated from the reduced metal in a downstream cyclone and can be condensed afterwards to obtain an almost pure CO_2 stream. Therefore CLC shows high potential as carbon capture and storage (CCS) technology. In the air reactor the reduced metal oxide is re-oxidized with air (fluidization fluid). The air reactor exhaust gas, mainly consisting of Nitrogen and excess Oxygen, is separated in a downstream cyclone from the circulating solids.

Since conversion proceeds with time, the residence time of particles in reactors is of interest, in consideration of plant efficiency. The particle residence time depends on the fluid-dynamic behaviour of a reactor. For better understanding of the fluid-dynamic behaviour of the chemical looping combustion pilot plant, a cold flow model (CFM) with a scale of 1:3 to the hot unit was built. The CFM operates at ambient conditions and is made out of acrylic glass. Thus, the CFM is easy to handle and to modify. The bed material (bronze particles) is fluidized with air, according to the Glicksman criteria. In this thesis, the mean residence time of the fluidized particles in the fuel reactor of the CFM was investigated, with respect to the ULS fluidization, the global solids circulation rate and the fluidization rate of the fuel reactor.

The measuring system for the particle residence time was designed and built at the Vienna University of Technology for the cold flow model and works in conformity with the principle of magnetic fields: An electric conductor is winded to a coil and creates, when a current is applied, a magnetic field. At the time when ferromagnetic particles pass through the coil, the magnetic field of the coil changes and affects the inductance of the coil. For this purpose, ferromagnetic particles that exhibit nearly equal fluid-dynamic properties like the paramagnetic bronze particles are used. The change of the inductance is proportional to the mass of the ferromagnetic particles passing the coil at a certain time point. The thereby measured signals are recorded with a program created in LabVIEW. To determine the residence time distribution in the fuel reactor it is necessary to know the concentration of the magnetic particle in the streams that enter and leave the reactor at a certain time. Therefore two coils are fixed at the upper and lower loop seal of the cold flow model, to obtain an input and an output signal of the passing particles through the fuel reactor.

The mean residence time of the particles in the FR is then evaluated as a function of the variation of the solids circulation rate, the FR and the ULS fluidization velocities. The influence of the solids circulation rate showed the expected behaviour, according to Levenspiel, 1999, as well as the fuel reactor fluidization velocity. The ULS fluidization velocity had no significant influence on the particle residence time.

In addition, the vessel dispersion number (VDN) is evaluated for different fluidization conditions. The ULS fluidization variation had no significant influence. Whereas the vessel numbers decreased with increasing solids circulation rates, which indicates that the flow pattern slightly tend to the plug flow model. The experiments carried out at the lower fluidization rate of the fuel reactor lead to higher VDN. This is probably due to the higher particle mass found in the fuel reactor at the investigated conditions, what increases the relative share of the well-mixed FR zone compared to the flow-reactor-like loop seal ducts.

Furthermore the input signals obtained from the measurement were introduced into a simulation model, which was based on an assumed configuration of a connection in series of an ideal plug flow reactor (PFR) and an ideal continuous stirred tank reactor (CSTR). The model calculated the corresponding output signals. It has shown that the assumed model characterizes the system for the conditions studied very well.

From the obtained results it can be concluded that the applied residence time distribution measurement method based on magnetic properties is suitable for investigation of gas-solid systems.

KURZFASSUNG

Chemical Looping Combustion (CLC) ist eine neuartiges Verbrennungsverfahren, basierend auf der Wirbelschichttechnologie. Eine CLC Anlage mit einer Leistung von 120 kW wurde an der Technischen Universität Wien erbaut. Sie besteht unter anderem aus zwei zylindrischen Wirbelschichtreaktoren (dem sogenannten „air reactor“ (AR) und „fuel reactor“ (FR)), die als zirkulierende Wirbelschichten betrieben werden. Diese sind über einen oberen und unteren Siphon miteinander verbunden, um den gegenseitigen Gasaustausch zu verhindern. Normalerweise wird ein Metalloxid zwischen den beiden Reaktoren im Kreislauf zirkuliert. Im FR wird das Oxid mittels eines gasförmigen Brennstoffes reduziert. Als Brennstoff kommt meist Erdgas (Methan) zum Einsatz, wobei bei vollständigem Umsatz hauptsächlich H_20 und CO_2 entstehen, welche in einem nachgeschaltetem Zyklon vom Metalloxid abgeschieden werden. Der austretende Gasstrom kann kondensiert werden, um annähernd einen reinen CO_2 Gasstrom zu erhalten. Deswegen weist CLC ein hohes Potential auf, um Kohlenstoff effizient abscheiden zu können. Im AR wird das reduzierte Metalloxid mittels Luft wieder re-oxidiert. Das dadurch entstandene Gas, welches hauptsächlich Stickstoff und Sauerstoff (Überschusssauerstoff der Oxidation) enthält, wird in einem nachgeschaltetem Zyklon von dem zirkulierenden Metalloxid getrennt. Der oxidierte Sauerstoffträger gelangt über den oberen Siphon in den FR.

Da jede chemische Reaktion eine bestimmte Zeit für ihre Umsetzung braucht, ist die Verweilzeit eines Stoffes in einem Reaktor von großem Interesse, um eine Anlage mit dem höchst möglichen Wirkungsgrad betreiben zu können. Um die fluid-dynamischen Eigenschaften der CLC Anlage besser verstehen zu können, wurde ein Kaltmodell (CFM) im Maßstab 1:3 zur Heißanlage gebaut. Das Kaltmodell wird bei Raumtemperatur betrieben und besteht aus Acrylglas, was eine leichtere Handhabung sowie rasche Umbauten ermöglicht. Zur Fluidisierung des Kaltmodells wird Luft eingesetzt und die verwendeten Partikel bestehen aus Bronze. In dieser Diplomarbeit wurde die Verweilzeit im FR des Kaltmodells in Abhängigkeit der ULS und FR Fluidisierung, sowie des globalem Partikelumlaufs bestimmt.

Zur Messung der Verweilzeit wurde ein Messsystem entworfen und am Kaltmodell installiert, welches nach dem Prinzip des Elektromagnetismus arbeitet: Eine stromdurchflossene Spule erzeugt ein Magnetfeld, welches durch die Präsenz ferromagnetischer Partikel beeinflusst wird. Bei der Änderung des magnetischen Feldes ändert sich proportional zu der Masse der durchströmenden Partikel die Induktivität der Spule. Zu diesem Zweck wurden ferromagnetische Partikel verwendet, die ähnliche fluid-dynamische Eigenschaften wie die paramagnetischen Bronzepartikel aufwiesen. Um auf die Verweilzeit im FR schließen zu können, ist es notwendig die Menge der ein- und austretenden ferromagnetischen Partikel zu kennen. Hierfür wurden zwei stromdurchflossene Spulen am oberen und untern Siphon angebracht. Die dadurch erhaltenen Signale wurden mittels eines in National Instruments LabVIEW erstellten Programms aufgenommen und die mittleren Verweilzeiten in Abhängigkeit der oben genannten Fluidisierungsvariationen bestimmt.

Die Variation des globalen Partikelumlaufs zeigte den zu erwartenden Einfluss auf die Verweilzeit, nach Levenspiel, 1999, ebenso die Variation der FR Fluidisierung. Die Fluidisierung des oberen Siphons hingegen hatte keinen signifikanten Einfluss auf die Verweilzeit.

Außerdem wurden die Dispersionszahlen des FR für die verschiedenen Fluidisierungsvariationen ermittelt. Die Variation der ULS Fluidisierung hatte keinen signifikanten Einfluss auf die Dispersionszahlen. Wohingegen bei sinkendem globalen Partikelumlauf die Dispersionszahlen sanken, was für eine Annäherung des Strömungsverhaltens an eine Pfropfenströmung spricht. Die durchgeführten Experimente mit dem geringer fluidisierten FR führten zu höheren Dispersionszahlen. Der Grund hierfür könnte in der höheren Partikelmasse liegen, die im FR unter den untersuchten Bedingungen vorherrschte.

Des Weiteren wurden die erhaltenen Messsignale in einem erstellten Programm bearbeitet, welches die Verweilzeit und ein Austrittssignal unter Annahme einer Reihenschaltung eines Rohrreaktors und eines kontinuierlichem idealen Rührkessels anstelle des FR simulierte. Das angewandte Modell beschrieb das Verhalten des FR sehr gut und die simulierten paßten mit den berechneten Verweilzeiten ebenfalls zusammen.

Aus den Ergebnissen kann geschlossen werden, daß sich die gewählte Methode gut zur Verweilzeitverteilungsbestimmung von Gas-Feststoff-Systemen eignet.

TABLE OF CONTENTS

LIST OF FIGURES

LIST OF TABLES

1 INTRODUCTION

Fluidized bed reactors are used in different industrial processes, for instance in energy generation, carbon capturing processes like chemical looping combustion, gasification or in other chemical processes like fluid catalytic cracking, calcium looping, etc. In these operations a fluid, gas or liquid, is fed from the bottom of a cylindrical vessel (riser), fluidizing the particles contained in the vessel. At higher fluidization velocities of the fluid, a fluid-like state of the material and the gas is obtained. The entrained particles and the gas are separated in a downstream cyclone, where the former flow through the subsequent downcomer. At the lower end of the downcomer, a loop seal connects the downcomer with the riser and prevents a reciprocal gas exchange.

Different processes, for example the regeneration of a catalyst in a fluid catalytic cracking operation or the conditioning of flue gas with calcium oxide, exhibit different reaction rates and since conversion increases with time, the fluidized particles require different times to react with the fluid. Thus the residence time of the fluidized particles in a reactor is an important economic parameter of plant efficiency.

In the literature various methods can be found for measuring the residence time distribution of the particles in CFBs but all of them exhibit some limitations for the application: several use a riser with open boundaries, the tracer particles are sometimes harmful, the detection system needs high equipment expense or the injection system works with pressurised air which may perturb the flow conditions.

Based on the circulating fluidized bed technology, a dual circulating fluidized bed system for generating energy (120 kW) was built at the Vienna University of Technology. Kolbitsch (Kolbitsch, 2009) described the system. For better understanding of the fluid dynamic behaviour, a cold flow model (CFM) was built (Rupanovits, 2007) and operated at ambient conditions.

The aim and scope of the present work is the investigation i.a. of the usage of ferromagnetic particles as tracer for particle residence time measurement in gas-solid fluidized bed systems and the applicability of simple coils as primary sensors. Furthermore this inductance-based measurement system is applied to a dual circulating fluidized bed cold flow model, where the residence time of the particles in the secondary fluidized bed reactor (fuel reactor) is determined. For the evaluation of the residence time, the operating parameters (fluidization velocities and solids circulation rate) are varied. Thereafter the obtained residence time signals are fitted to a combination of ideal reactor models (a plug flow and a continuous stirred tank reactor in series).

2 BACKGROUND

2.1 Fluid-dynamics in fluidized beds

Kunii et al., 1991, described the phenomenon of fluidization with the following words:

> *"Fluidization is the operation by which solid particles are transformed into a fluidlike state through suspension in a gas or liquid."*

A fluidized bed is achieved, when a fluid, gas or liquid, flows through a porous basement of a cylindrical vessel containing a granular material. Depending on the velocity of the fluid, different fluidization regimes are possible. *Figure 2-1* shows different fluidization regimes, obtained with increments in fluidization velocity, assuming that the density of the fluid is smaller than the solid material.

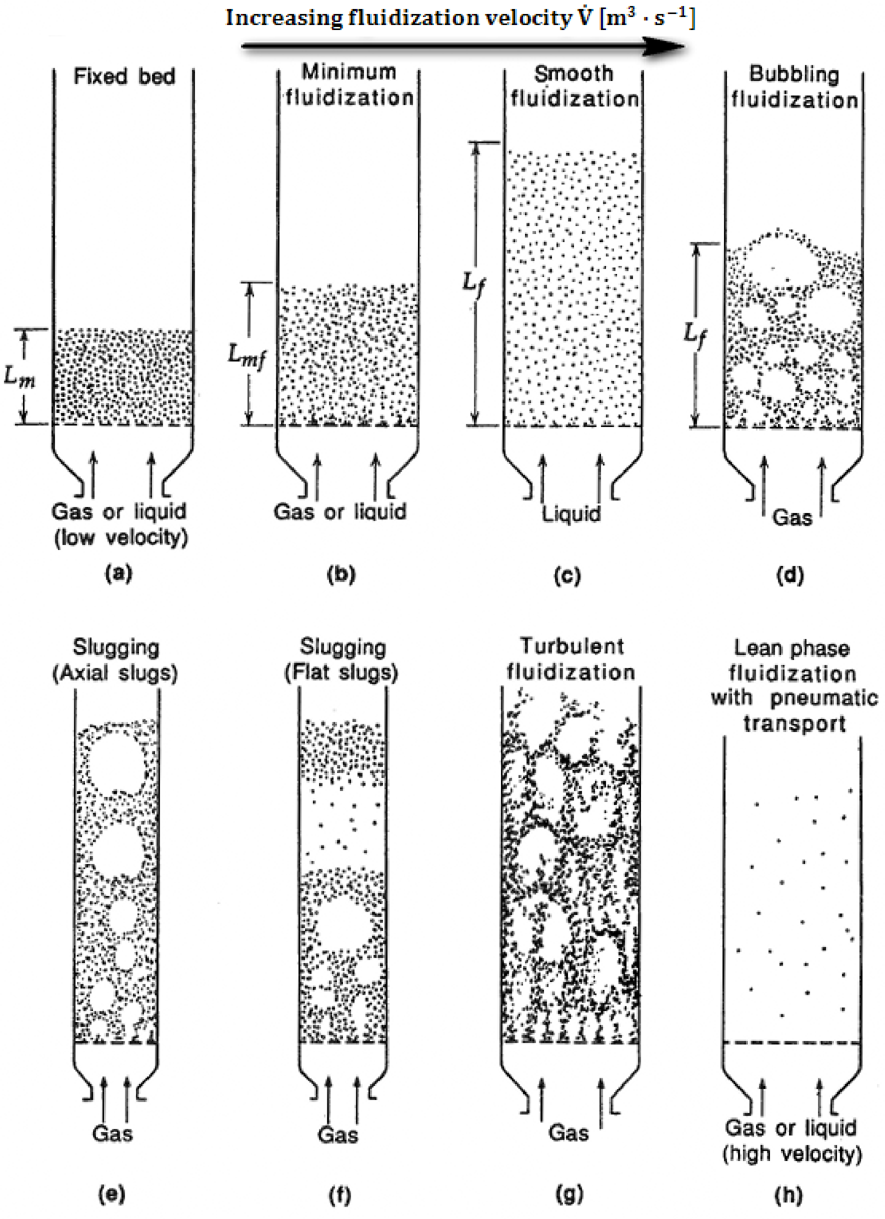

Figure 2-1: Fluidization regimes of solids fluidized by fluids (from Kunii et al., 1991).

The cases from *d)* to *g)* are observable mostly in gas-solid systems, the rest also in liquid-solid systems.

a) Fixed bed: At low velocity flow rates the fluid permeates through the void spaces between the stationary fine particles. There is no particle movement determinable.

b) Minimum fluidization: If the fluidization flow rate increases, the particles start to move in restricted zones and the fixed bed starts to expand. The minimum fluidization is reached when the frictional force between fluid and particles counterbalances the weight of the bed. At this stage, the pressure drop equals the weight of the particles in the fluid – this state is called the expanded bed. Until the state of the pneumatic transport, the pressure drop stays nearly the same, even when the fluidization velocity is increased.

c) Smooth fluidization: A smoothly fluidized bed is obtained in liquid-solid systems, when the fluidization flow rate increases slightly above the minimum fluidization. In gas-solid systems, this regime appears only under special conditions, for instance, when light fine particles are fluidized with dense gas at high pressure.

d) Bubbling fluidization: By increasing the fluidization flow rate in gas-solid systems above the minimum fluidization velocity, bubbles are formed. Near the bottom small bubbles are formed and with increasing height they merge to bigger ones. Furthermore large instabilities with channelling of gas and rising bubbles are observed. The volume of the bed stays nearly the same like at minimum fluidization but the fluctuation and the movement of the particles in the bed becomes more vigorous. Very rarely the bubbling fluidization regime appears also in liquid-solid systems, for instance when a very dense bed is fluidized with a liquid of low density.

e) Slugging (axial slugs): Gas bubbles tend to coalesce and grow while they are rising. In a bed of small diameter and large bed-height it might happen that the bubbles spread across the vessel and the fine particles flow down near the wall.

f) Slugging (flat slugs): Flat slugs occur when coarse particle are used in a narrow fluidized bed. The particles are pushed upward above a bubble and some flow downward through the flat slug. At a certain height the slug collapses and at about the same time, another slug is formed. This unstable periodical motion is repeated.

g) Turbulent fluidization: So far, a surface or upper limit of the bed was observable. But by increasing the fluidization velocity above slugging in a bed with fine particles, the obvious level of the gas-solid bed disappears and entrainment becomes visible. The high velocity causes a turbulent motion of solids, which tend to stick together in so called clusters of different shapes and sizes.

h) Pneumatic transport: At this state, the buoyancy force rise above the weight of the particles and makes the solids to be carried away with the fluid.

As mentioned above, there are different fluidization regimes possible. They lead to advantages when using them for industrial operations. Some of them are:

- The operations are easy to control due to the smooth, liquid-like behaviour of the suspension.
- As a result of the rapid mixing of the inventory, the reactor conditions are nearly isothermal.
- Once the fluidized bed reaches the operating conditions (what means no temperature gradient all over the bed, quasi steady flow conditions), the large inventory acts as a thermal buffer, which is able to resist against rapid temperature changes.
- In comparison with other contacting systems the mass and heat transfer rates between particle and gas are high.
- The heat transfer between submerged objects and fluidized beds is also high. Therefore, heat exchangers require comparatively smaller surface areas.

If the fluidization velocity is lower than the pneumatic transport velocity, the fluidized bed behaves like a liquid and hence, following phenomena can be observed (*Figure 2-2*):

a) If a relative light object is put into the fluidized bed, it floats on the surface.
b) If the fluidized bed is tipped, the surface remains horizontal.
c) The solids will stream out of a hole, whenever the later is located at a level lower than the suspension surface.
d) If two fluidized beds are connected together, the levels of the surfaces will equalize to reach similar pressure drops, assuming similar bed material, fluid and outlet pressure for both beds.
e) There is a pressure drop between different vertical levels.

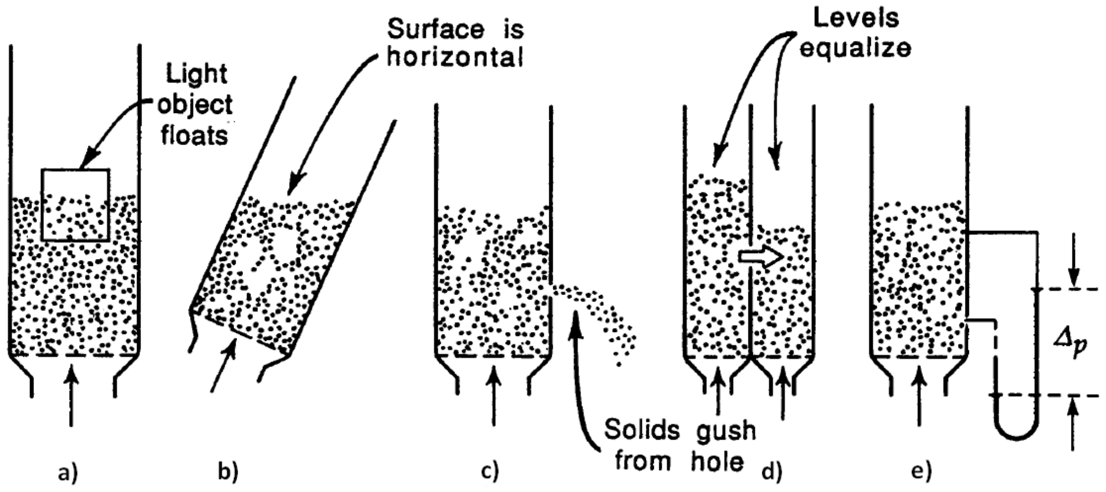

Figure 2-2: Liquid like behaviour of fluidized beds (from Kunii et al., 1991).

2.2 Fluid-dynamics of circulating fluidized beds (CFBs)

In this chapter, only gas-solid systems of circulating fluidized beds are described. In these systems the particle inventory, starting from the bottom of the riser, is fluidized with a gas (*Figure 2-3*). At higher fluidization velocities of the gas, a fluid-like state of the material and the gas is obtained. The entrained particles and the gas are separated in a downstream cyclone, where the former flow through the subsequent downcomer. At the lower end of the downcomer, a loop seal connects the downcomer with the riser and prevents a reciprocal gas exchange.

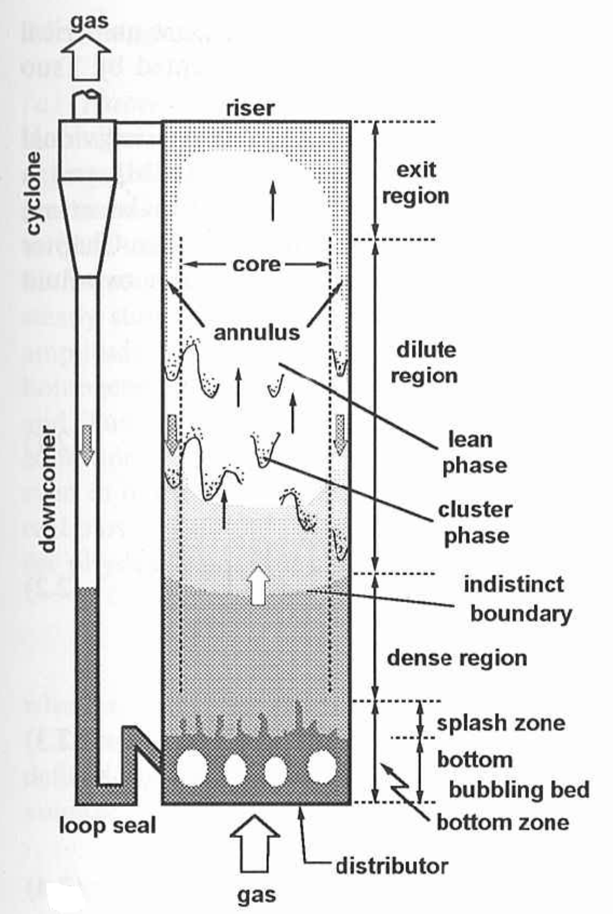

Figure 2-3: Regions and phases of gas-solid systems in a CFB (from Reh, 1971).

When particles are fluidized with gas in a circulating fluidized bed, they pass through the following configuration parts of the unit (*Figure 2-3*):

- Distributor: Is located at the bottom of the riser and disperse the gas flow for homogeneous fluidization.
- Riser: Is the area where particles and gas are contacting.
- Cyclone: The particles are separated from the gas by means of a centrifugal force separator.

- Downcomer: If the gas stream flows upward relative to the downward flowing solid stream, the solids are transferred against this pressure gradient by gravity and generate a frictional pressure drop. In *Figure 2-4* the two possible cases of the gas (v_g) and particles (v_s) flow directions are shown. Both cases exhibit a relative velocity (v_r).

- Loop seal: Works in analogy to a siphon and prevents the gas of flowing back into the downcomer, due to the high pressure zone in the riser and make the recirculation of the particles possible.

In the riser different regions with different solid fractions and flow structures can be identified (*Figure 2-3*):

- Bottom zone: Voids are formed after the gas entry near the bottom (bottom bubbling bed) and as the voids brake (splash zone) the solids are ejected. The voids carry the solids through the bottom zone to the so called dense region.

- Dense region: The weight of the particles counterbalances the weight of the gas, what leads to an indistinct boundary between the dense and the dilute region. The former is usually the so called fluidized bed. At the indistinct boundary the particle concentration decreases and a more dilute region is obtained.

- Dilute region: Usually circulating fluidized beds work at fluidization rates many times higher than minimum fluidization. In this case, particles with a smaller diameter start being elutriated in the space above the dense region. In the dilute region are two different phases prevailing: The cluster phase, where the smaller particles stick together and form clusters and the lean phase, where are fewer particles present. Additionally, the region near the riser wall (annulus) consists of a slow downward flowing dense suspension and the region in the core of a rapid upward flowing dilute suspension, where the concentration of solid particles is usually a magnitude lower than in the annulus.

- Exit region: In general it can be a smooth or an abrupt exit. The former has no influence on the flow regime of the riser, accomplished with a smooth bend from the top of the riser to the cyclone entry. The latter is shown in *Figure 2-3* and leads to an increase of the solids concentration at the top of the riser, due to the back flowing of the particles at the abrupt exit.

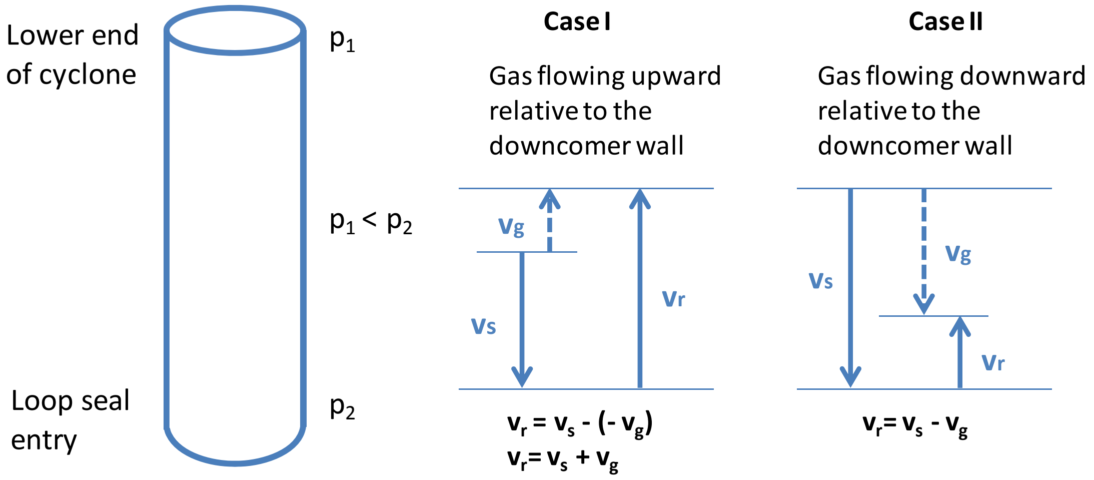

Figure 2-4: Relative gas-solid velocity in a downcomer (from Grace et al., 1997).

Li et al. (Li et al., 1980) presented for the first time the voidage distribution of particles in a CFB riser (D = 0,09 m, H = 8 m). Their experimental data are shown in *Figure 2-5*. The axial voidage distribution shifts from the dense to the dilute region with a gradual concentration changeover. This characteristic of the fast fluidized beds is found in columns of large and small diameters. Additionally, Li et al. (Li et al., 1980) fitted the equation (2.1) for the solids distribution.

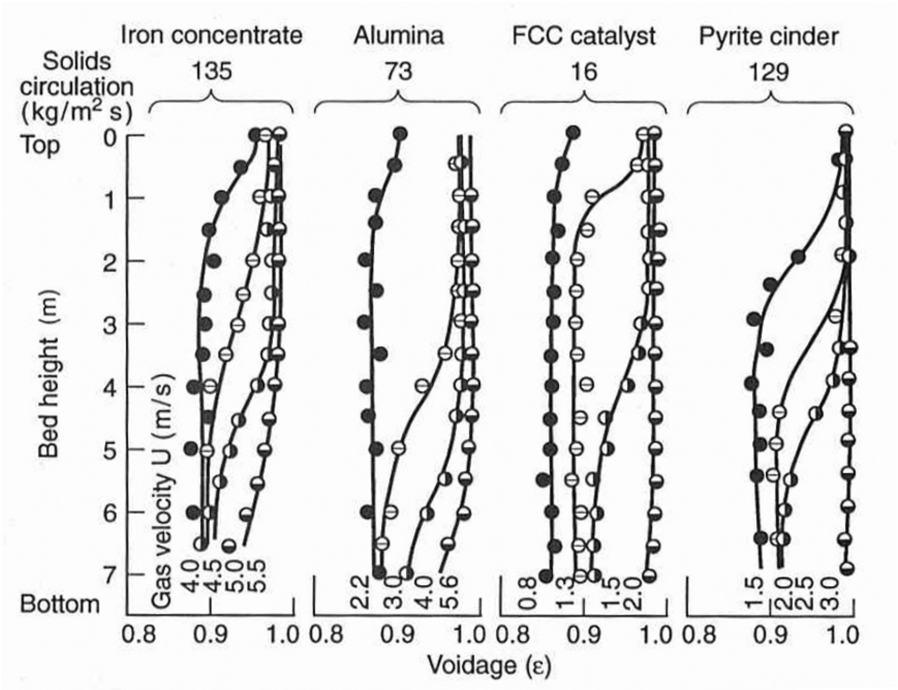

Figure 2-5: Typical S-shaped voidage distribution in a riser (D = 0.09 m) (Li et al., 1980).

$$\frac{\varepsilon_s - \varepsilon_s^*}{\varepsilon_{sd} - \varepsilon_s} = e^{-(z - z_i)/z_o} \qquad (2.1)$$

The corresponding curve is sketched in *Figure 2-6*. Near the bottom, in the dense region, the solid fraction has a value of ε_{sd}. This value varies depending on the regime (bubbling, turbulent or fast fluidization). At the exit of the column the value reaches ε_{se}. ε_s^* is the saturation carrying capacity of the gas and is smaller than ε_{se}. The change of the concentration takes place in a height of z_0.

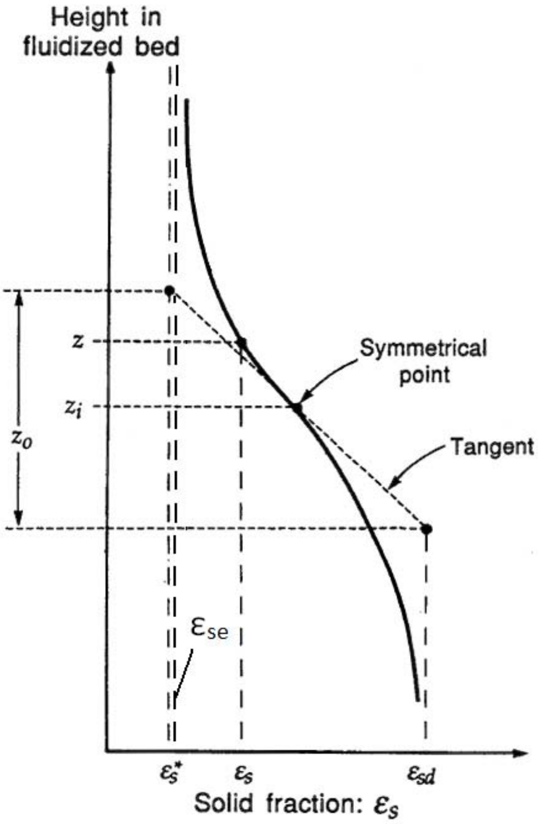

Figure 2-6: Solid fraction distribution with the height in a CFB according to (2.1) (Kunii et al., 1991).

2.3 Cold flow model studies

In general, a cold flow model (CFM) is an instrument for optimizing and better understanding of the fluid-dynamics of a process. CFMs are downscaled copies of hot units and are easy to handle because they normally work at room temperature and atmospheric pressure, so there is no need for isolations or other laborious devices. They are usually made out of an easy modifiable material, in the case that additional parts or measurement instruments are necessary.

In the case of fluidized beds, Glicksman (Glicksman, 1984) described independent dimensionless parameters that characterize a bed. If hot and cold unit have nearly equal dimensionless numbers, it is possible to conclude on the behaviour of the hot unit, based on the results from the CFM.

In Table 2-1 the important dimensionless parameters are listed.

Table 2-1: Scaling relationships by Glicksman (Glicksman, 1984).

Dimensionless numbers	**Equations**
Reynolds number (Re_P)	$\frac{d_P \cdot U \cdot \rho_G \cdot \Psi}{\eta_G}$
Froude number (Fr_P)	$\frac{U^2}{g \cdot d_P}$
Ratio of solid to fluid density	$\frac{\rho_P}{\rho_G}$
Ratio of bed height to particle diameter	$\frac{h_B}{d_P}$
Ratio of column diameter to particle diameter	$\frac{D}{d_P}$
Sphericity	Ψ
Particle size distribution	-

Another dimensionless number for the characterization of fluidized beds is the so called Archimedes number (Ar), which can be interpreted as the ratio of the buoyancy and the inertial forces that act on the particles and is defined as

$$Ar = \frac{(\rho_P - \rho_G) \cdot \rho_G \cdot d_P^3 \cdot g}{\mu^2}, [-]. \tag{2.2}$$

The buoyancy force acts upward and is the weight of the displaced fluid. The inertial force is a pseudo force that maintains the current state of the particle movement.

2.4 Residence time distribution

2.4.1 Space-time and exit age distribution in ideal reactor systems

In each chemical process, a raw material is treated by means of physical and chemical operations to manufacture a desired product. The main transformation takes place in a reactor, whereby the reactor design plays a decisive role. Therefore the understanding of chemical kinetics, thermodynamics, heat and mass transfer, fluid mechanics and degree of efficiency is needed to create a proper reactor (*Figure 2-7*).

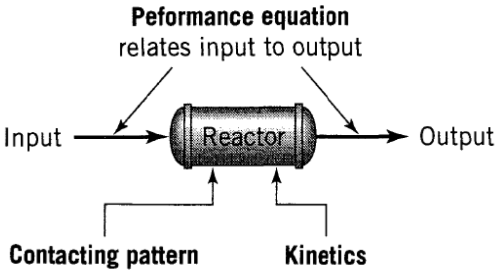

Figure 2-7: Information needed to predict how a reactor will perform (Levenspiel, 1999).

Depending on how many phases are involved in a chemical reaction, a distinction is made between homogeneous and heterogeneous systems and also a classification among catalytic and noncatalytic systems. Table 2-2 shows different classifications of chemical reactions.

Table 2-2: Classification of chemical reactions useful in reactor design (Levenspiel, 1999).

	Noncatalytic	Catalytic
Homogeneous	Most gas-phase reactions	Most liquid-phase reactions
	Fast reactions such as burning of a flame	Reactions in colloidal systems Enzyme and microbial reactions
Heterogeneous	Burning of coal	Ammonia synthesis
	Rosting of ores	Oxidation of ammonia to produce nitric acid
	Attack of solids by acid	Cracking of crude oil
	Gas-liquid absorption with reaction	Oxidation of SO_2 to SO_3
	Reduction of iron ore to iron and steel	

For instance, two reactants A and B form a desired product C, with the reaction rate r_C:

$$A + B \rightarrow C \tag{2.3}$$

Every chemical reaction proceeds with a reaction rate which is defined by the equation (Levenspiel, 1999),

$$r_i = \frac{1}{V} \cdot \frac{dn_i}{dt} = \frac{moles\ i\ formed}{(volume\ of\ fluid)(time)}\ , \tag{2.4}$$

where the reaction rate of the component *i* changes in number of moles per time, according to a unit volume *V* of the reacting fluid. Typically real reactions differ from this simple equation, because of their varying reaction rates due to thermal gradients or other influences. Three different types of ideal reactor systems are normally used to approach the conditions as closely as possible to the real reactors (*Figure 2-8*). They are the ideal batch reactor, the steady-state mixed flow reactor and the steady-state plug flow reactor. In this chapter only the last two models of ideal flow systems are described. As the CFB is typically a continuous process, the batch reactor as a discontinuous system is not discussed.

Furthermore the space-time τ is defined as the ratio between the volume of the reactor and the volumetric feed:

$$\tau = \frac{V_R}{\dot{V}}\ . \tag{2.5}$$

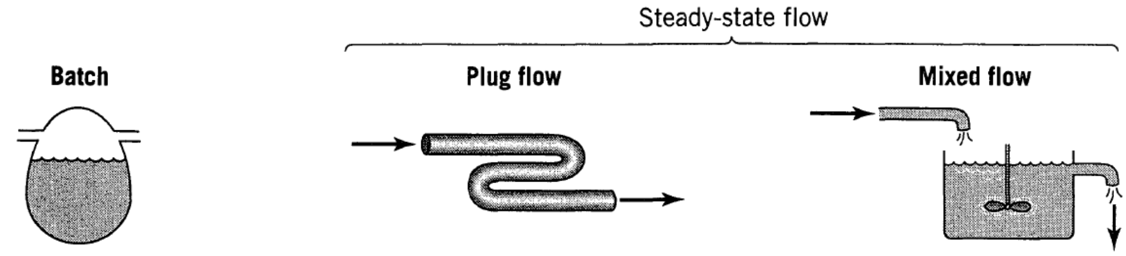

Uniform composition everywhere in the reactor, but of course the composition changes with time.

Fluid passes through the reactor with no mixing of earlier and later entering fluid, and with no overtaking. It is as if the fluid moved in single file through the reactor.

Uniformly mixed, same composition everywhere, within the reactor and at the exit.

Figure 2-8: Ideal reactor models (Levenspiel, 1999).

- ***Space-time and exit age distributions of continuous flow systems***

It is evident, that real reactors may differ from those with ideal flow conditions. *Figure 2-9* shows some deviations from the ideal flow patterns – recycling and channelling of the fluid or creation of dead regions can occur.

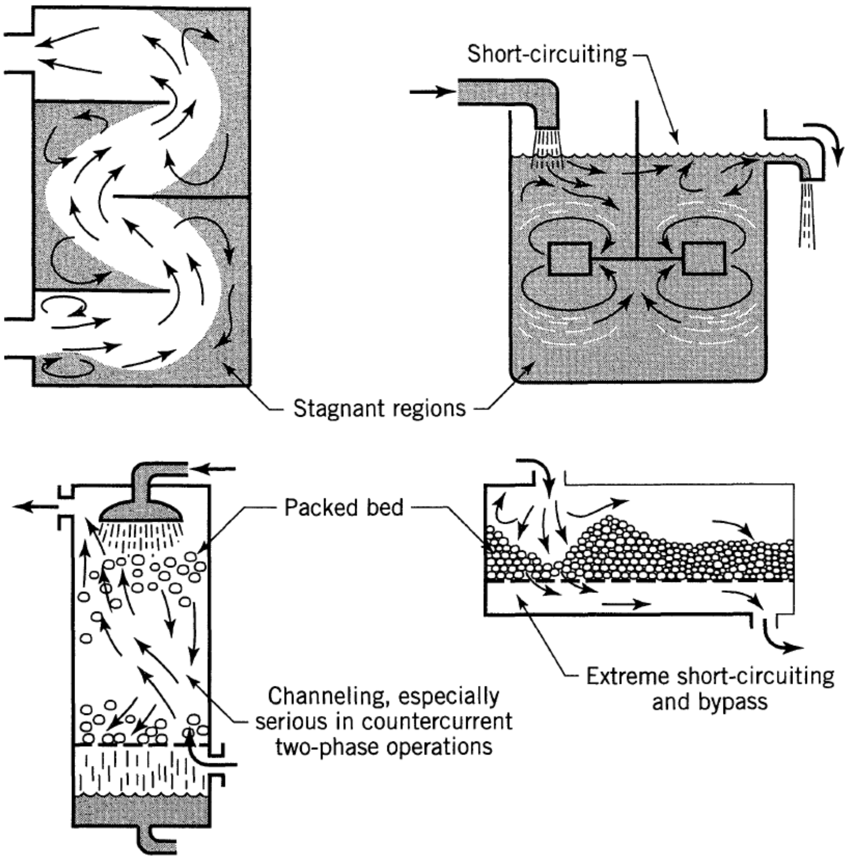

Figure 2-9: Nonideal flow patterns that may exist in real reactors (Levenspiel, 1999).

One of the important factors for describing the deviation of a real reactor from an ideal flow system is the residence time distribution (RTD) or the exit age distribution **E**, which illustrate the time that the elements need to flow through the vessel. The mean residence time should not be mistaken with the space-time τ, which is a parameter that gives the mean time required to process one reactor volume of feed. In a system of no reaction and constant density, the space-time τ is equal to the mean residence time. As the CFM is such a system, the concept of space-time τ will be used.

There are a few methods, how to find the **E** curve of a real process, one of them is the use of a tracer material. The concentration of the tracer (which presents a distinctive property) is measured at the output of the reactor (C_{pulse} curve) and for easy interpretation of this signal a pulse or a step signal at the input of the reactor is advantageous.

For the evaluation of the **E** curve in the case of a sharp pulse input signal similar to a Dirac delta function, it is also necessary to know the total amount of tracer material introduced and the flow velocity of the fluid (the particle flow velocity is assumed to be the same) and the volume of the reactor.

The area under the output curve is the integral of the measured concentration:

$$A = \int_0^\infty C \cdot dt \cong \sum_i C_i \cdot \Delta t_i = \frac{M}{\dot{V}} \ , \qquad \left[\frac{kg * s}{m^3}\right] . \tag{2.6}$$

The equation for the mean residence time based on the C_{pulse} curve is found by:

$$\tau = \frac{\int_0^\infty t \cdot C \cdot dt}{\int_0^\infty C \cdot dt} \cong \frac{\sum_i t_i \cdot C_i \cdot \Delta t_i}{\sum_i C_i \cdot \Delta t_i} = \frac{V_R}{\dot{V}} \ , \qquad [s] \ , \tag{2.7}$$

also shown in *Figure 2-10*.

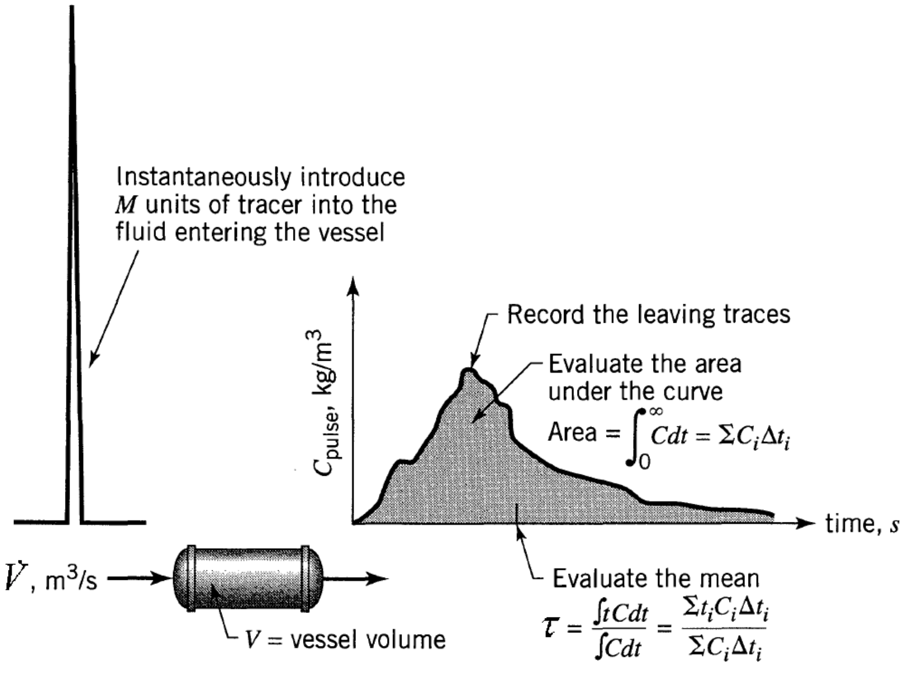

Figure 2-10: Information obtainable from the pulse tracer experiment (Levenspiel, 1999).

The variance of a signal in general is calculated by

$$\sigma^2 = \frac{\int_0^{\infty} (t-\tau)^2 \cdot C \cdot dt}{\int_0^{\infty} C \cdot dt}\ , [s^2]. \tag{2.8}$$

The dimensionless variance of the RTD for a pulse input signal according to Levenspiel, 1999 is given by the following equation:

$$\sigma_\theta^2 = \frac{\int_0^{\infty} (t-\tau)^2 \cdot C \cdot dt}{\tau^2 \cdot \int_0^{\infty} C \cdot dt}\ , [-]. \tag{2.9}$$

In the case of a Dirac delta input function, the area under the ***E*** curve gets unity, as every C_{pulse} signal of the concentration scale is divided by the Area *A*. For that reason the equations for ***E*** and τ_E change to

$$\boldsymbol{E} = \frac{C_{pulse} \cdot \dot{\mathrm{V}}}{M}\ , [\mathrm{s}^{-1}] \tag{2.10}$$

and

$$\tau_E = \frac{\sum_i t_i \cdot \boldsymbol{E}_i \cdot \Delta t_i}{\sum_i \boldsymbol{E}_i \cdot \Delta t_i}\ , [s]. \tag{2.11}$$

For the dimensionless exit age distribution function $\boldsymbol{E}_\theta$, the ***E*** curve is multiplied with τ and the time axis is illustrated with

$$\theta = \frac{\mathrm{t}}{\tau}\ , [-], \tag{2.12}$$

as shown in *Figure 2-11*.

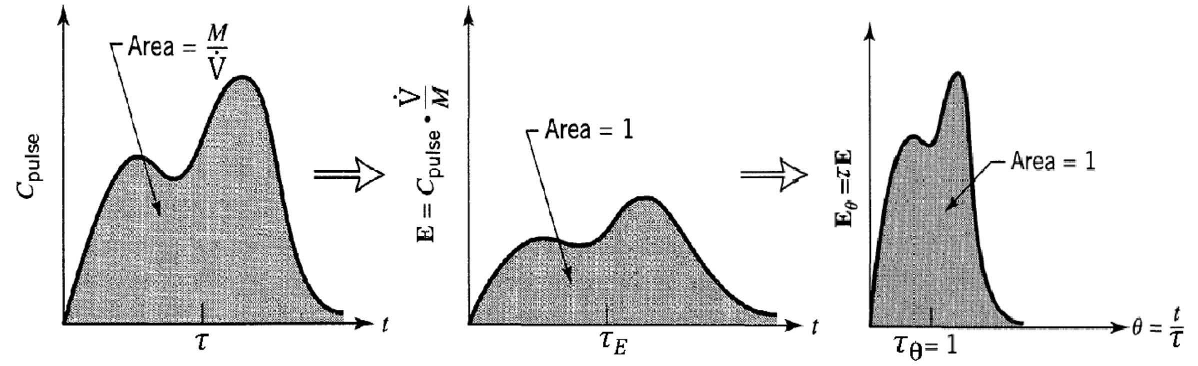

*Figure 2-11: Transformation of an experimental C_{pulse} curve into an **E** and an $\boldsymbol{E}_\theta$ curve (Levenspiel, 1999).*

Levenspiel, 1999 characterized the behaviour of the components in a continuous flow stirred tank reactor (CSTR). For this type of reactor a uniform composition is assumed in every moment. *Figure 2-12* shows the notation for a mixed reactor.

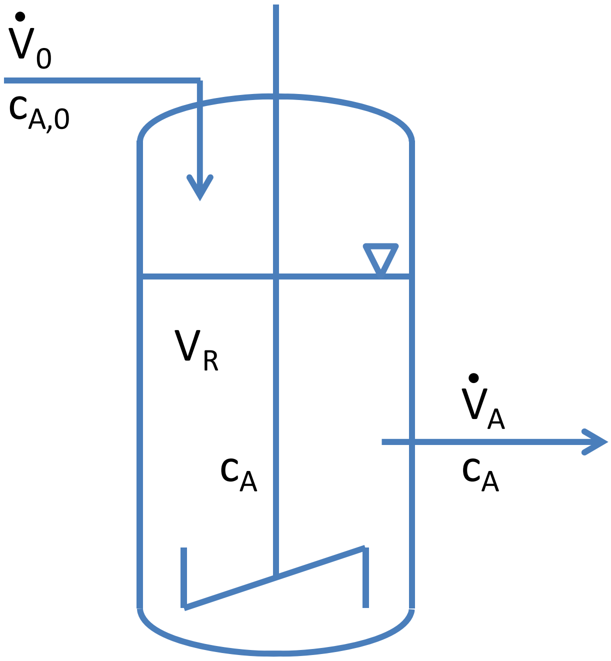

Figure 2-12: Mass balance in an ideal mixed continuous stirred tank reactor.

For a tracer A the mass balance is given for a continuous stirred tank reactor with

$$\frac{dn_A}{dt} = \dot{n}_{A,0} - \dot{n}_A - \dot{n}_{A,R}. \tag{2.13}$$

Following assumptions with respect to the CFM are made:

- The tracer particles have no reaction rate: $-r_A = 0$.
- The volumetric flow does not change: $\dot{V}_0 = \dot{V}$ = const.

Therefore equation (2.13) can be written with

$$V_R \cdot \frac{dc_A}{dt} = \dot{V} \cdot c_{A,0} - \dot{V} \cdot c_A\,. \tag{2.14}$$

After rearrangement, the equation shown above becomes a differential equation of first order:

$$\frac{dc_A}{dt} + \frac{\dot{V}}{V_R} \cdot c_A = \frac{\dot{V}}{V_R} \cdot c_{A,0}\,, \tag{2.15}$$

where the time constant is the reciprocal space-time.

The exit age distribution of a CSTR is shown in *Figure 2-13*, with the equation deduced from Levenspiel, 1999:

$$\boldsymbol{E}(t) = \frac{1}{\tau} \cdot e^{\frac{-t}{\tau}}\,(CSTR\ model) \tag{2.16}$$

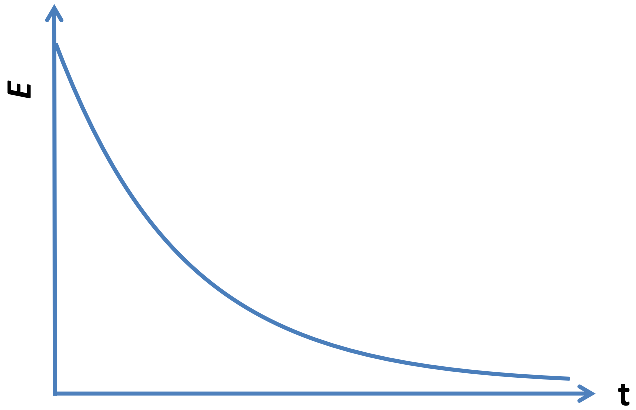

Figure 2-13: Exit age distribution of a CSTR.

The exit age distribution for a plug flow reactor (PFR) is shown in *Figure 2-14*. This reactor supposes an equal fluid element velocity; therefore the space-time for every element is equal as well. Furthermore there is no backmixing of the fluid in the flow direction but across the flow direction the mixing process become infinitely large. Deduced from Nauman (Nauman, 2008), the exit age distribution is described with

$$E(t) = \delta \cdot (t - \tau). \tag{2.17}$$

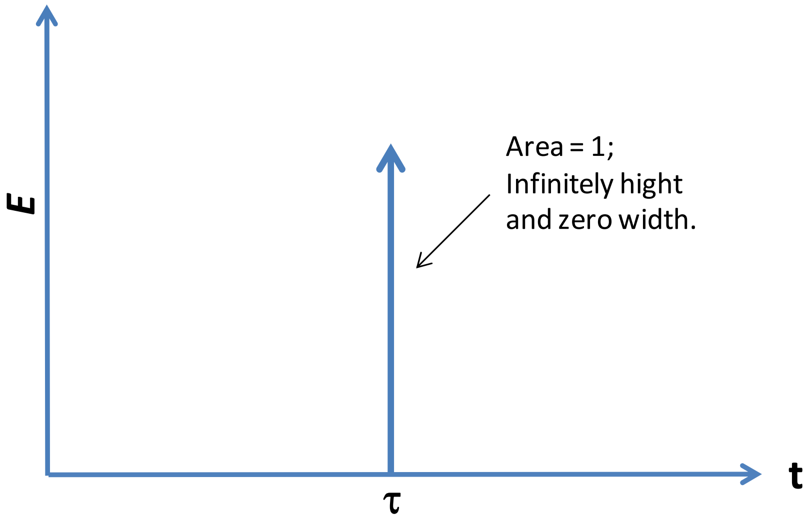

Figure 2-14: Exit age distribution of a PFR.

δ is the so called Dirac delta function, what means that for the parameter t all corresponding **E** values are zero, except at τ. Any input signal of a tracer A with a certain concentration c_A flows through a PFR without distortion but with a time delay of τ (*Figure 2-15*).

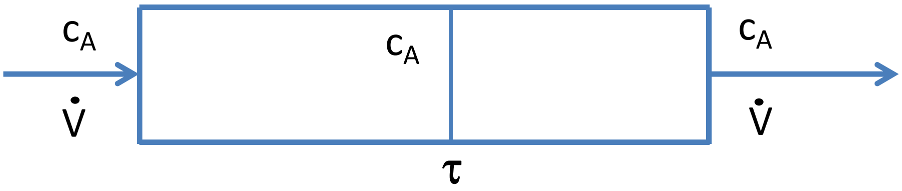

Figure 2-15: Plug flow reactor

In general real input signals differ from a Dirac delta function. The injection of the tracer is usually done in the input stream of a reactor. Before the tracer enters the reactor, the concentration is measured (C_{in}) and shows a variance as well as the measured output signal (C_{out}) (*Figure 2-16*):

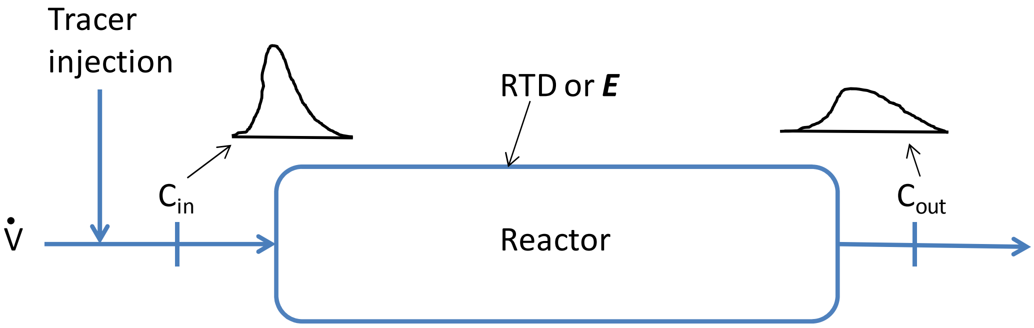

Figure 2-16: Input and output tracer signals of a reactor.

The correlation between the input and output signal is given by the exit age distribution ***E*** and according to Levenspiel, 1999 by the equation

$$C_{out}(t) = \int_0^t C_{in}(t') \cdot \boldsymbol{E}(t - t')dt', \tag{2.18}$$

where the tracer material enters the reactor t’ or τ seconds earlier. The output signal C_{out} is the convolution of ***E*** with the input signal C_{in}. In *Figure 2-17* an input and output signal curve of a tracer is shown. An element needs t’ seconds to pass through the reactor.

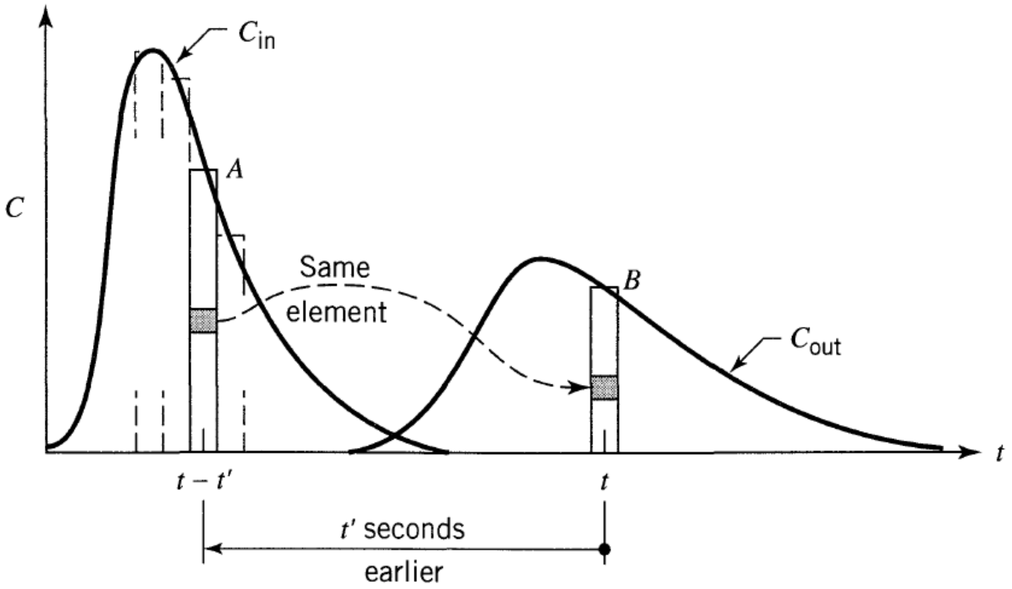

Figure 2-17: Graphical representation of input and output curves of an impulse tracer measurement (Levenspiel, 1999).

According to Levenspiel, 1999, for an input signal with a variance different than a Dirac delta function, the dimensionless variance of the ***E*** curve is given by the equation

$$\sigma_\theta^2 = \frac{\sigma_{out}^2 - \sigma_{in}^2}{(\bar{t}_{out} - \bar{t}_{in})^2} = \frac{\sigma_{RTD}^2}{(\tau)^2}, [-]. \tag{2.19}$$

Furthermore Levenspiel assumed a coefficient ***D***, which is a parameter for the longitudinal dispersion of a tracer in a reactor and is correlated to the dimensionless variance as follows:

$$\sigma_\theta^2 = 2 \cdot \left(\frac{\boldsymbol{D}}{\mathrm{u} \cdot L}\right), \tag{2.20}$$

where the so called vessel dispersion number $\left(\frac{\boldsymbol{D}}{\mathrm{u} \cdot L}\right)$ is a dimensionless parameter for the extent of the axial dispersion:

$$\left(\frac{\boldsymbol{D}}{\mathrm{u} \cdot L}\right) \to \infty \Longrightarrow mixed\ flow, large\ dispersion.$$

$$\left(\frac{\boldsymbol{D}}{\mathrm{u} \cdot L}\right) \to 0 \Longrightarrow plug\ flow, negligible\ dispersion.$$

The reciprocal value of the vessel dispersion number (VDN) is usually called Péclet number (e.g. Pröll et al., 2007). However, according to Levenspiel, 1999 the reciprocal value of the vessel dispersion number is not the Péclet number. ***D*** gives the movement by longitudinal dispersion and the coefficient $\mathfrak{D}$ used in the Péclet number is the coefficient for the molecular mass transfer. In

Figure 2-18 the dimensionless exit age distribution $\boldsymbol{E}_\theta$ for different VDN in accordance to the time unit θ are shown.

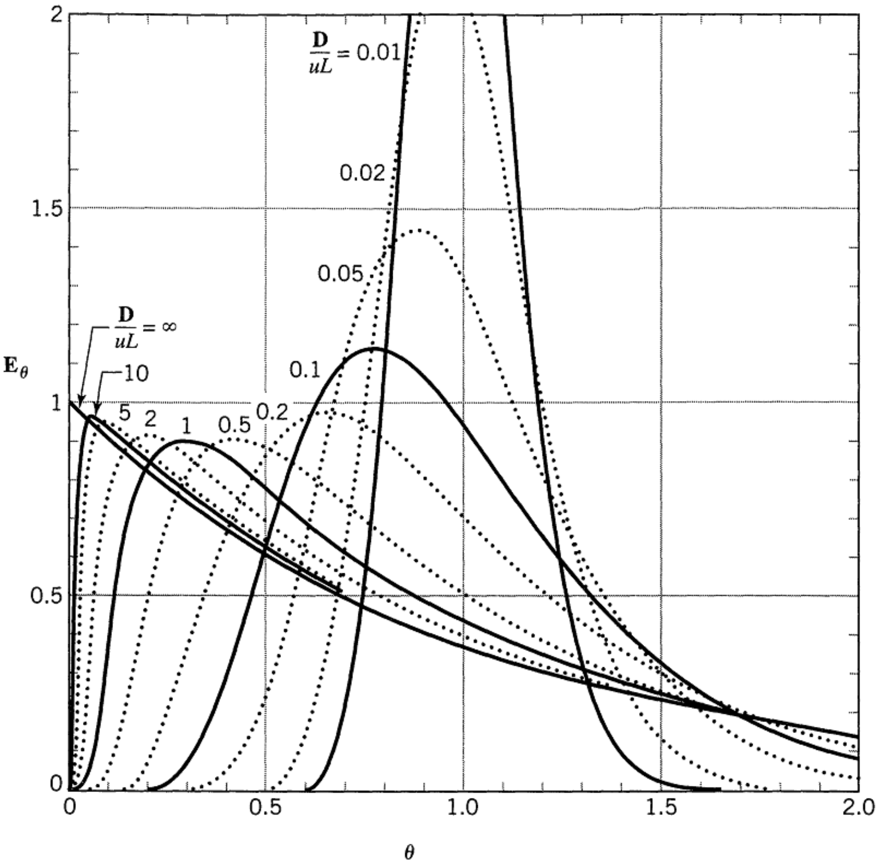

Figure 2-18: ***E***$_\theta$ *for different vessel dispersion numbers (Levenspiel, 1999).*

Equation (2.20) applies in the range from $0 < \text{VDN} < 0.01$. In this range the error is about 5%. For higher values of the VDN it should be distinguished between vessels with open or closed boundaries. The former assume same flow conditions at the vessel boundaries as in the vessel. Whereas the model with closed boundaries supposes a change of the flow patterns at the entrance and the exit of the vessel. To obtain a proper RTD curve with a tracer measurement, a vessel with close-close (cc) boundaries is required. Then the ***E*** curve is identical to the RTD curve. In other cases (close-open, open-close, open-open) the RTD curve deviates from the ***E*** curve. The equation for the dimensionless variance in a closed-closed vessel for a dispersion number higher than 0.01 and lower than 1 is given by:

$$\sigma_{\theta cc}^2 = 2 \cdot \left(\frac{\boldsymbol{D}}{u \cdot L}\right) - 2 \cdot \left(\frac{\boldsymbol{D}}{u \cdot L}\right)^2 \cdot \left[1 - e^{-\frac{u \cdot L}{\boldsymbol{D}}}\right]. \qquad (2.21)$$

For a vessel dispersion number higher than 1, the assumption of the model does not meet the vessel conditions and Levenspiel hesitates the application of the model discussed.

2.4.2 Exit age distribution in circulating fluidized beds

In a gas-solid reactor, the residence time of the gas is usually different as for the solid particles. The former is well described in the literature (e.g. Mahmoudi et al., 2010) and uncomplicated to detect. For example He, Ar, CO_2, CH_4, Propane and other tracer gases have been introduced in a riser and were continuous detected. For measuring the residence time distribution of solid particles, there are many methods described in the literature as well, but all of them exhibit some limitations that bring some problems with it:

- It is difficult not to interrupt the global flow of the circulating fluidized bed when taking or injecting the tracer particles.
- Tracer particles which behave like the bed material and have nearly the same fluid dynamic properties are difficult to find.
- The used tracer material should not be harmful. This would lead to an extreme increment in safety measures.
- The equipment should be kept within economic limits.
- The measurements should be done in closed boundaries to obtain the true residence time.

To get a brief overview on the experimental methods for evaluating the solids exit age distribution, the following classification of the techniques reported in literature is done, according to Harris et al., 2002. The techniques are classified in disruptive and non-disruptive techniques, depending on whether the measuring system influences the flow conditions.

- **Disruptive techniques**

  In general the tracer injection system has influence on the flow conditions and before the measurement can be repeated it is necessary to stop the fluidization and/or to separate the bed material from the tracer particles.

  - Radioisotope tracers:

    In the literature many experiments can be found for determining the residence time with radioactive tracer particles (e.g. Harris et al., 2002), which were injected by means of a pressurised air pulse and identified at the output of the reactor using scintillation detectors. The time response of these systems is fast and the reproducibility is also given. But on the other hand, the potential health risk should not be underestimated, the needed equipment and the treatment of the particles after an experiment are economic factors that limit their utilisation.

  - Chemically different tracers:

    The use of tracer salt particles is an appropriate method and the evaluation can be easily performed but requires prolonged time, because of the sample preparation. In the experiment of Smolders et al. (Smolders et al., 2000), the injection of the tracer material was accomplished at the bottom of the riser, with the use of pressurised air. The mixture of bed material (sand) and the injected salt was collected at the axis of the exhaust pipe at the top of the riser. After sampling, the mixtures were dissolved in water and the conductivity was measured and transformed into a corresponding concentration.

- Thermal methods:

  Westphalen et al. (Westphalen et al., 1995) developed a method using preheated tracer particles, which were injected into the bed. An array of thermal resistors measured the distribution of the particles in the bed. The spread of the tracer particles was described by mathematical models. The indirect evaluation of the tracer concentration by the temperature measurement is a disadvantage of this method and leads to uncertainty of the results.

- Magnetic tracers:

  Avidan et al. (Avidan et al., 1985) used ferromagnetic tracer particles in an expanded fluidized bed. When the particles passed through a section where a copper wire was wrapped around the fluidized bed, the inductance was detected via a bridge circuit system. This fluidized bed had no closed boundaries and the injection of the tracer particles was placed in the middle of the bed for evaluating the mixing behaviour of the solids. Goldblatt (Goldblatt, 1990) described in his thesis the measurement of the RTD in a circulating fluidized bed, using compressed air to introduce tracer particles at the bottom of the riser. The bed and the tracer material had not the same fluid dynamic properties, they had different densities and mean particle diameters.

- **Non-disruptive techniques:** The flow conditions are not influenced by the measuring and/or injection system.

  - Optical methods:

    Harris et al. (Harris et al., 2003) designed a cold flow model of a circulating fluidized bed with closed boundaries, where the bed material had phosphorescent properties. For the fast measurement a batch of particles was activated by means of a light flash at the entry of the riser and they were detected by a photomultiplier at the exit of the riser. The mean particle size was under the limit of 40 µm, what could have lead to agglomeration of the particles. The activation is problematic in dense fluidized beds as well.

2.5 Selection of the tracer method

In the present work, ferromagnetic tracer particles were used for the measurement of the exit age distribution, considering the following advantages:

- The tracer particles are not harmful and no special safety precautions are necessary.
- The particle size distribution of the ferromagnetic tracer particles can be provided similar to the size distribution of the bed material.
- Only small amounts of the tracer particles (about 0.5% of the bed material, according to Avidan et al., 1985) are necessary for the measurement.
- The particle concentrations are directly correlated to the measurement.
- The measurement preparation requires no prolonged time.

2.6 Inductance

2.6.1 General basics of inductance

Metals usually present a crystalline structure, which consists of fixed positive charged atoms (ions) and freely, moveable valence electrons in the metal matrix. These electrons reside normally in the ultimate atom shell and are easy to release in the metal structure, to the so called electron gas.

An electric current ***I*** is obtained, if an amount of charge carriers *Q* are constantly moving in the time t through a cross-sectional area A of a conductor under the influence of an electric field.

$$\boldsymbol{I} = \frac{Q}{t} \ . \tag{2.22}$$

In every conductor of an electric current, a resistance subtends the charge carriers. This resistance depends on the material (specific resistance P), the geometrical dimensions (l_c, A_c) of the conductor and physical conditions, for instance the temperature and is calculated with:

$$R = P \cdot \frac{l_c}{A_c}. \tag{2.23}$$

If a current moves through an electrical conductor, a magnetic field with the corresponding magnetic field intensity *H* is formed. This intensity is arranged in concentric circles and acts clockwise around the electrical conductor (*Figure 2-19*). This effect is the so called electro magnetism.

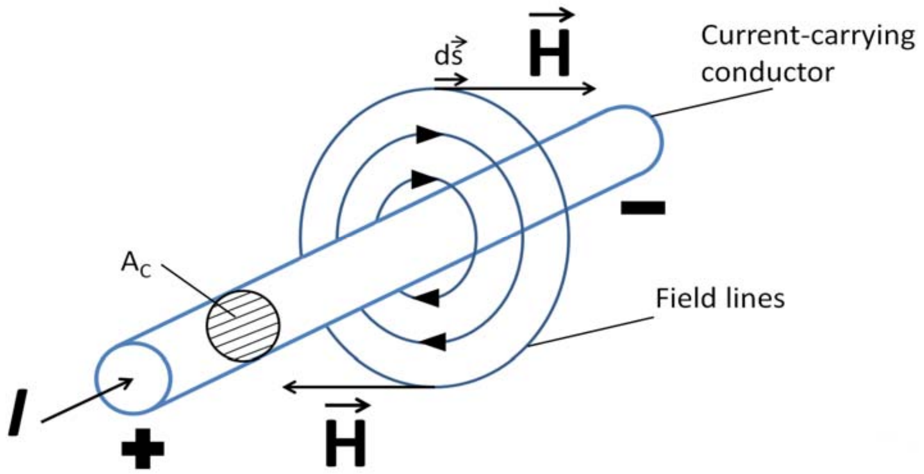

Figure 2-19: Magnetic fields of an electric conductor, "electro magnetism".

The interrelationship between the electrical current and the magnetic field intensity is given by the closed loop integral of the magnetic field intensity and the differential distance d$\vec{s}$:

$$\boldsymbol{I} = \oint \vec{H} \cdot d\vec{s} \ , [V]. \tag{2.24}$$

An electrical conductor which is winded into a coil, creates also a homogeneous magnetic field inside the coil with a north and south pole, as shown in *Figure 2-20*.

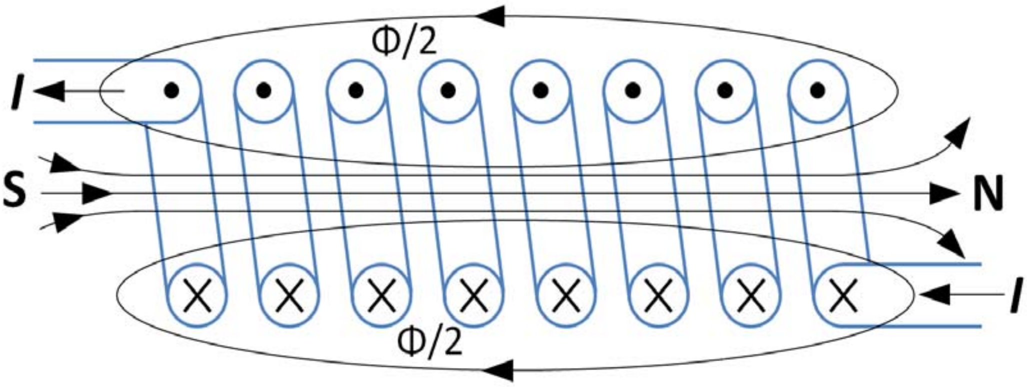

Figure 2-20: Magnetic field of a coil.

The correlation between $\vec{H}$ and the magnetic flux density $\vec{B}$ in a homogeneous and isotropic medium is given by the equation

$$\vec{B} = \mu_0 \cdot \mu_r \cdot \vec{H} = \mu \cdot \vec{H} \ , [Wb], \tag{2.25}$$

where µ is the magnetic permeability, which depends on the medium in the coil. Table 2-3 shows some examples for different kinds of materials:

Table 2-3: Magnetic permeability of different media.

Material	Magnetic permeability	Examples
Diamagnetic	$\mu_r < 1$	Bismuth
Paramagnetic	$\mu_r \approx 1$	Air, cooper, glass, etc.
Ferromagnetic	$\mu_r \gg 1$	Magnetic material

Another important parameter is the magnetic flux (*Figure 2-20*), which is calculated with:

$$\Phi = \int_A \vec{B} \cdot d\vec{A} \ , [Vs] \tag{2.26}$$

If the permeability is constant, the magnetic flux density is proportional to the electric current **I**. So the magnetic flux created by the electric current is as well directly proportional to the instantaneous electric current. The proportional factor at N coils is the so called inductance *L* and is calculated with

$$\mathrm{L} = \frac{N \cdot \Phi}{I} \text{ , } [H]. \tag{2.27}$$

The inductance *L* of a coreless inductor is given by the expression

$$L = N^2 \cdot \ \mu_0 \cdot \frac{A}{l + \frac{d}{2.2}} \tag{2.28}$$

and for an inductor with a core by

$$L = N^2 \cdot \ \mu_0 \cdot \mu_r \cdot \frac{A}{l + \frac{d}{2.2}} . \tag{2.29}$$

If the permeability µ in the coil varies, the inductance of the coil changes.

If an inductor is operated in an alternating current circuit, it has the complex resistance or so called impedance $\underline{Z}$. The effective resistance R is the real part of $\underline{Z}$ and the reactance X is the imaginary part of $\underline{Z}$, as shown in *Figure 2-21*. For a coil, the reactance can be calculated based on the inductance and the frequency of the applied alternating voltage, according to equation (2.30).

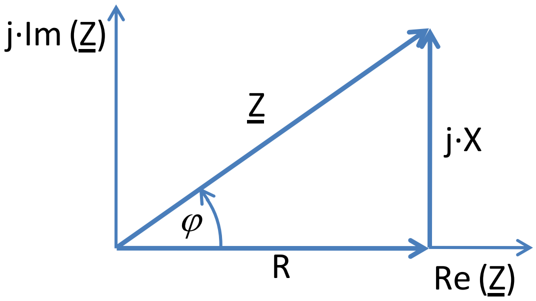

Figure 2-21: Impedance $\underline{Z}$, composing of an effective resistance R and an inductive reactance X_L.

$$X_L = 2 \cdot \pi \cdot f \cdot L. \tag{2.30}$$

The impedance $\underline{Z}$ of a coil is then the sum of the effective resistances and the inductive reactance and can be written with:

$$\underline{Z} = R + j \cdot X_L. \tag{2.31}$$

The impedance $\underline{Z}$ is the absolute value of the complex sum of R and X_L and can be calculated with:

$$|Z| = \sqrt{R^2 + X_L^2}. \tag{2.32}$$

The current and the electric potential exhibit a phase difference, which can be calculated with:

$$\varphi = \tan^{-1}\left(\frac{X_L}{R}\right). \tag{2.33}$$

2.6.2 Previous tests with LC resonator

An LC resonator consists of a capacitor connected to an inductor (*Figure 2-22*). This configuration is able to fulfil electrical oscillations.

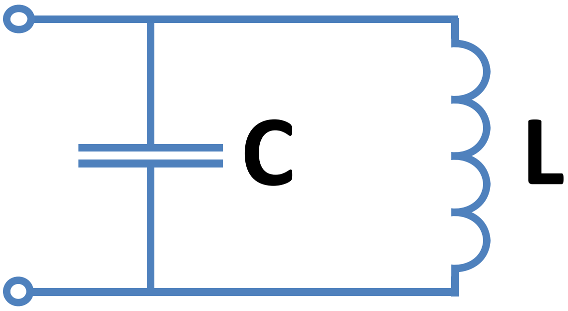

Figure 2-22: LC resonator.

These electrical oscillations exchange energy in form of the magnetic field of the inductor and the electric field of the capacitor and are characteristic for such systems. This happens with a certain frequency described by the Thomson equation:

$$f_0 = \frac{1}{2 \cdot \pi \cdot \sqrt{L \cdot \boldsymbol{C}}}\ . \tag{2.34}$$

Tobias Pröll and Diana Carolina Guío Pérez, from the Vienna University of Technology, carried out frequency measurement of an LC resonator for different core compositions. Ferromagnetic particles, homogeneously distributed with different concentrations in a bed of bronze particles and a capacitor of known capacitance were used, to calculate the inductance L_x with the rearranged Thomson equation

$$L_x = \frac{1}{4 \cdot \pi^2 \cdot \boldsymbol{C} \cdot {f_0}^2}\,. \tag{2.35}$$

A glass tube with an inner diameter of 0.02 m was filled with the tracer samples and wrapped by an inductor. Table 2-4 shows the compositions of the mixtures used with the measured frequencies and the calculated corresponding inductivities. *Figure 2-23* shows the calibration curve. The higher the steel content in the mixture, the larger was the obtained inductance.

Table 2-4: Steel particle compositions with corresponding frequencies and inductivities.

m% steel	C [µF]	f [Hz]	L [mH]
0	0.5	1854	14.74
1	0.5	1851	14.79
5	0.5	1833	15.08
10	0.5	1806	15.53
25	0.5	1721	17.10
50	0.5	1577	20.37
75	0.5	1450	24.10
100	0.5	1358	27.48

These initial tests have shown the general applicability of the method and have motivated the construction of a highly sensitive measurement device based on the measurement of the inductance of the coil through the impedance $\underline{Z}$ in an alternating voltage bridge, which will be introduced in Chapter 3.3.

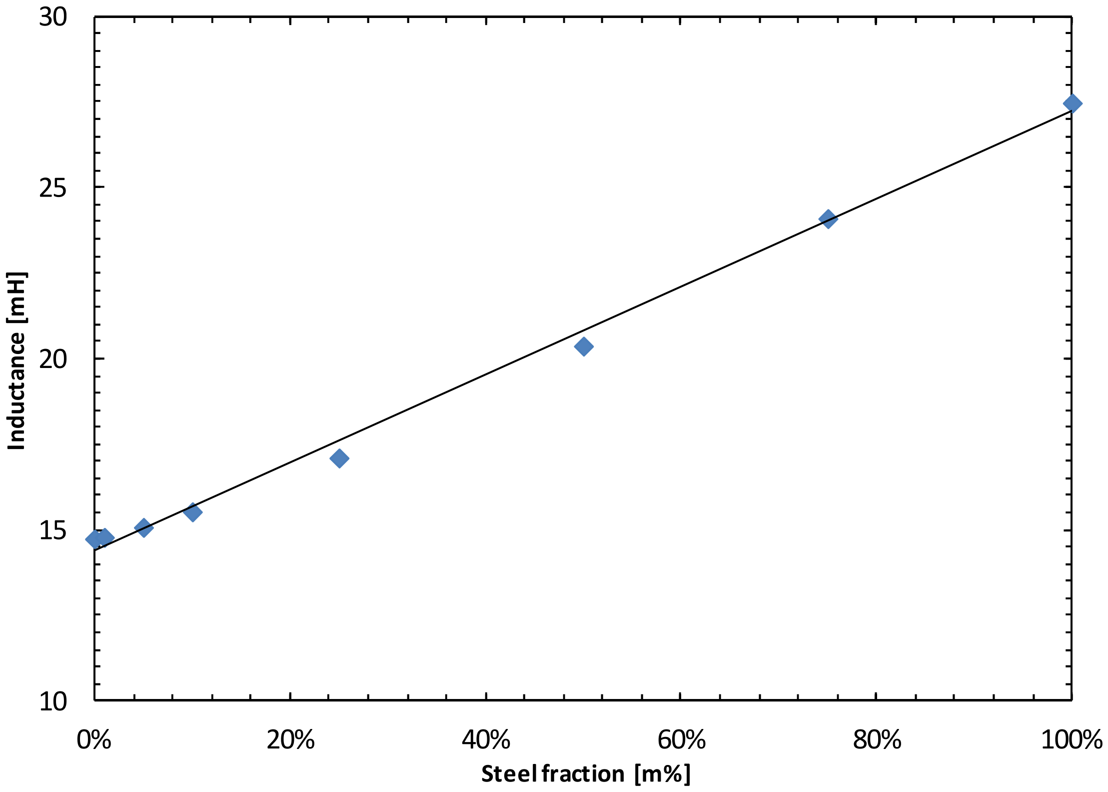

Figure 2-23: Calibration curve from the inductance in dependence of the steel fraction.

3 EXPERIMENTAL

3.1 Description of the cold model

- Hot 120 kW CLC pilot plant

Based on the circulating fluidized bed technology, a chemical looping combustion plant (120 kW) was built at the Vienna University of Technology. Kolbitsch (Kolbitsch, 2009) described the hot unit. For better understanding of the fluid dynamic behaviour, a cold flow model with a scale of 1:3 to the hot unit was built (Rupanovits, 2007). It works at ambient conditions and is made out of acrylic glass. The height is about 2 m and the air and fuel reactor have a diameter of about 0.05 m.

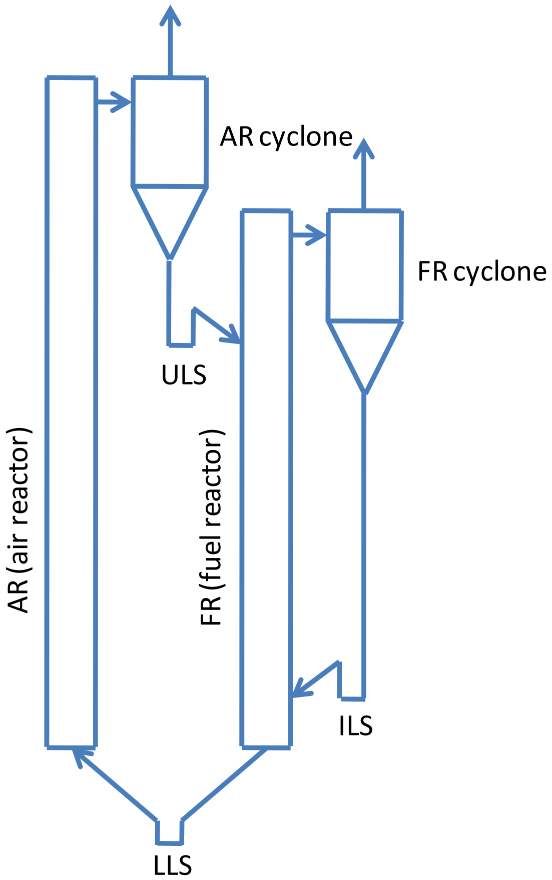

Figure 3-1: Dual circulating fluidized bed; Chemical looping combustion concept.

In the hot unit, a metal oxide (bed material) is circulated between the air reactor (AR) and the fuel reactor (FR). *Figure 3-1* shows the main parts of the CLC unit. The FR is fluidized with methane (fluidization fluid) and reduces the metal oxide. In the FR mainly the gaseous products H_2 and CO_2 are formed and separated from the reduced metal in the downstream cyclone (FR cyclone). In the AR the reduced metal is oxidized back again with air (fluidization fluid). The AR fluidization determines the global solids circulation. The gaseous stream that leaves this reactor contains mainly N_2 and excess oxygen from the oxidation. This flue gas is separated from the oxidized metal in the downstream cyclone (AR cyclone). The fluidized loop seals prevent the gaseous streams of following the metal particles in the next reactor. The LLS ensures the hydraulic communication between the two reactors and closes the global solids circulation loop.

- Cold flow model design

To reproduce the fluid dynamic behaviour of the 120 kW hot unit (h), a CFM (c) with a scale of 1:3 was built. The cold flow model operates at ambient conditions and is made out of acrylic glass. The dimensions of the CFM are shown in Table 3-1 and the CFM is graphically represented in *Figure 3-2*:

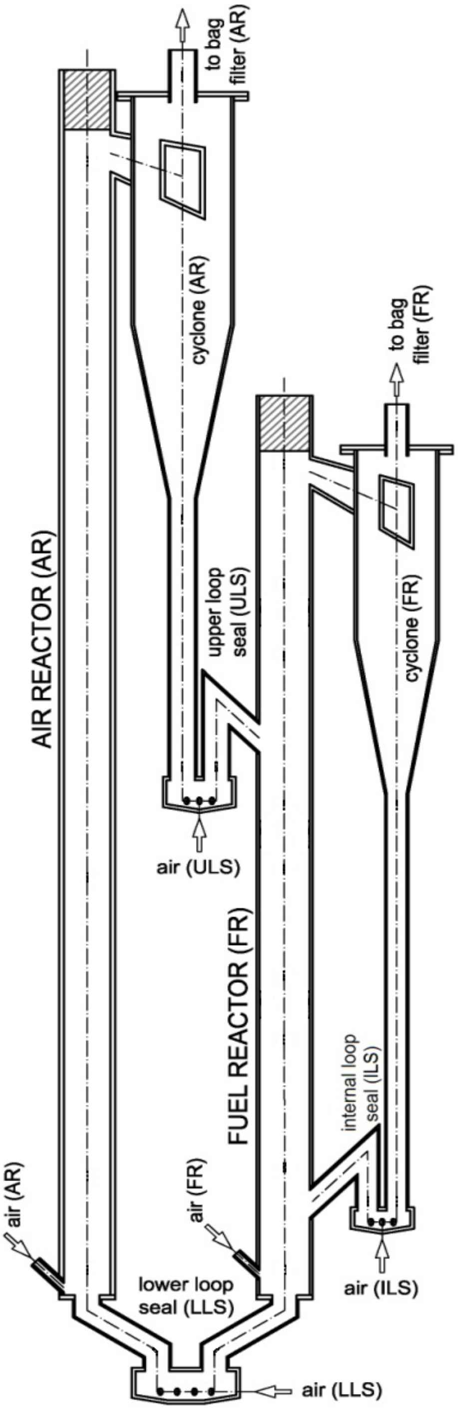

Figure 3-2: Sketch of a DCFB CFM (D. C. Guío-Pérez et al., 2011).

Table 3-1: Data of the cold and hot unit (Rupanovits, 2007).

Parameter	AR_h	FR_h	AR_c	FR_c	Dimension
η_G	$4.7 \cdot 10^{-5}$	$4.1 \cdot 10^{-5}$	$1.79 \cdot 10^{-5}$	$1.79 \cdot 10^{-5}$	Pa·s
ρ_G	0.3159	0.2884	1.22	1.22	$kg \cdot m^{-3}$
U	7.32	2.08	4.25	1.21	$m \cdot s^{-1}$
ρ_P	3200	3200	8900	8900	$kg \cdot m^{-3}$
d_P	123	123	41.5	41.5	µm
Ψ	0.99	0.99	1	1	-
D	0.15	0.1593	0.05	0.054	m

To achieve similar dimensionless numbers, bronze particles with an appropriate size distribution and air as fluidization fluid were chosen, according to the Glicksman criteria (Glicksman, 1984). The ratio between the dimensionless numbers of the two units should be approximately one to fulfil the scaling relationships of Glicksman. In Table 3-2 the parameters of the air and fuel reactors of the hot and cold units are listed and the ratios are chosen to approach the Glicksman criteria.

Table 3-2: Dimensionless numbers of the CFM and the hot unit (Rupanovits, 2007).

Parameter	AR_h	FR_h	AR_c	FR_c	$AR_h : AR_c$	$FR_h : FR_c$
Reynolds number (Re_P)	7.86	2.35	15.85	4.50	0.50	0.52
Froude number (Fr_P)	$3.4 \cdot 10^4$	$2.7 \cdot 10^3$	$3.4 \cdot 10^4$	$2.7 \cdot 10^3$	1	1
Ratio of solid to fluid density	$10.13 \cdot 10^3$	$11.10 \cdot 10^3$	$7.27 \cdot 10^3$	$7.27 \cdot 10^3$	1.39	1.53
Ratio of column diameter to particle diameter	1 260.5	1 338.7	1 250	1 350	1.01	0.99

3.2 Characterization of materials

The particle size distribution for the bronze particles is shown in *Figure 3-3*. For the measurement of the residence time distribution in the FR of the CFM, ferromagnetic particles with a similar particle size distribution (*Figure 3-4*) and a different relative permeability to the bronze particles were used as tracer material. In Table 3-3 some of the properties of the bronze and ferromagnetic particles are listed.

The agglomeration tendency of particles below a size of about 40 µm increases and may become crucial. Before the measurement could be started, the ferromagnetic particles had to be sieved because of the existence of a small amount of particles with a diameter smaller than 40 µm. *Figure 3-5* shows the particles before (a) and after (b) sieving.

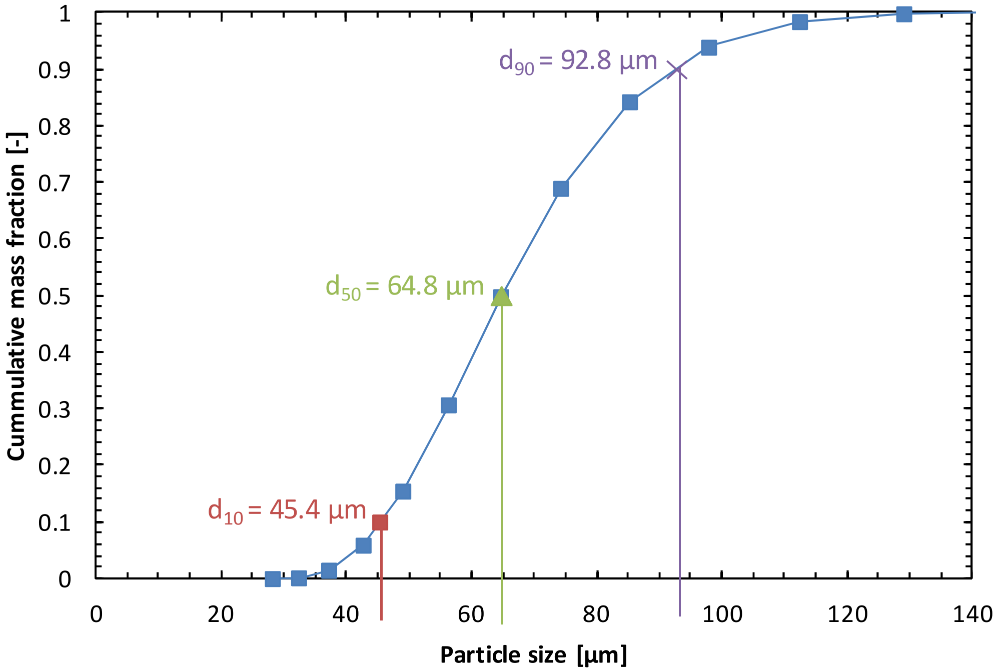

Figure 3-3 Particle size distribution of the bronze powder.

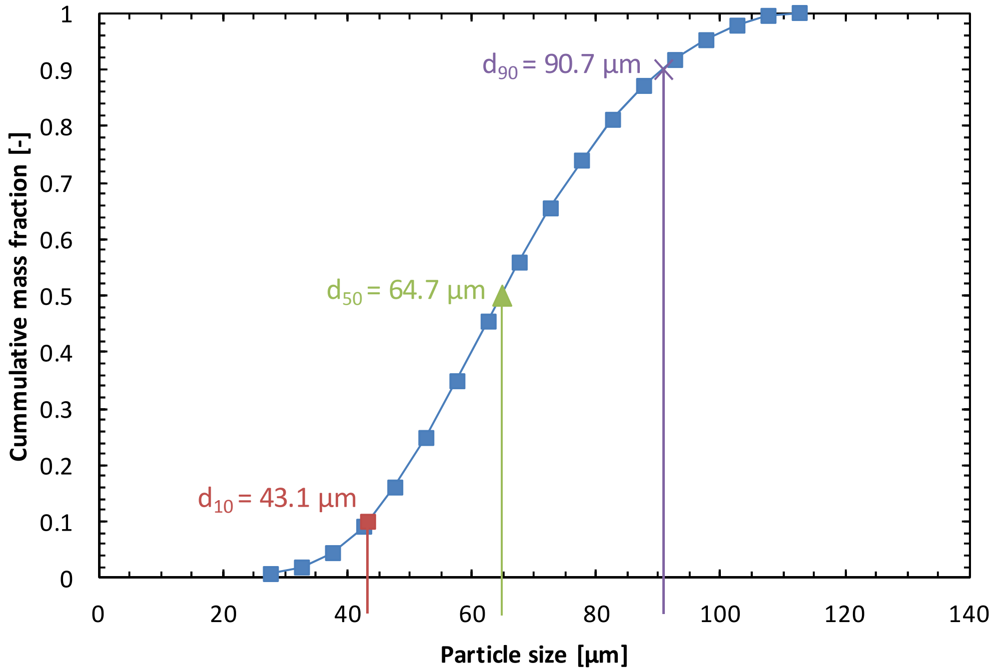

Figure 3-4: Particle size distribution of the steel powder.

Table 3-3: Comparison of steel and bronze particle properties.

Property	**Bronze**	**Steel**
Relative permeability μ_r (μ/μ_0) [-]	< 1.01	> 300
Particle density ρ [kg·m^{-3}]	8730	7560
Particle mean size d_p [µm]	72	68
Sphericity Ψ [-]	1	1
Archimedes number [-]	125	92

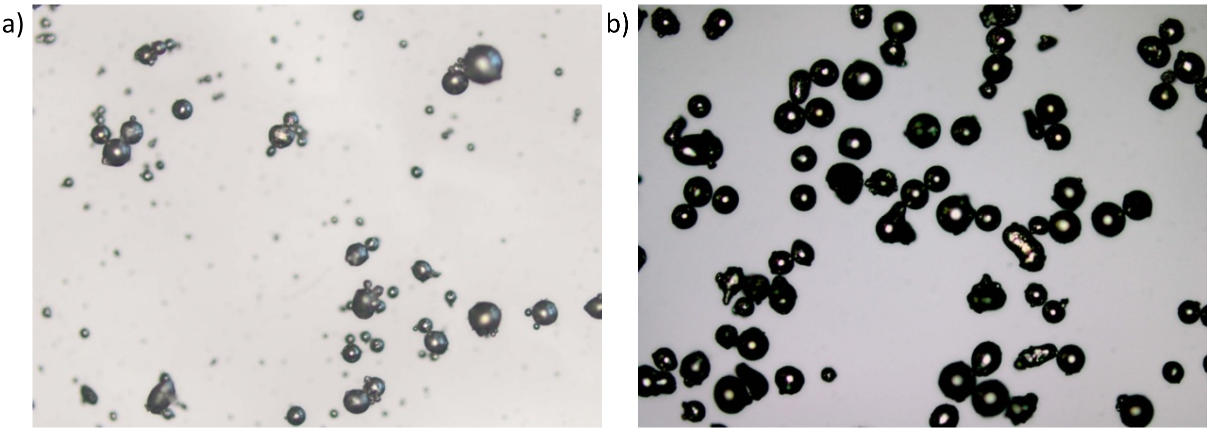

Figure 3-5: Steel particle images before (a) and after (b) the filtration (Magnification: 10x).

3.3 Description of the system for residence time measurement

For the measurement of the particle residence time in a reactor it is necessary to know the concentration of the particles in the streams that enter (input signal) and leave (output signal) the reactor at a certain time (Chapter 2.4). A step or pulse input signal of tracer particles as input signal is advantageous, due to the easy interpretation of the output signal. Other input signals are also possible (e.g. random or periodic input), but are harder to interpret and for this reason are not considered. A step input signal would need a sudden change of a property of the fluidized particles. Therefore a pulse input signal was chosen and it was generated by introducing ferromagnetic particles to the system. In this thesis, the residence time of the particles at moderate gas velocities in the FR is discussed, without fluidizing the internal loop (*Figure 3-6*).

The control volume for the input and output signals and the corresponding coils are shown in *Figure 3-7*. A third coil (ILS coil) is placed in the internal loop to detect the particles elutriated from the fuel reactor. The third coil is not discussed because this thesis covers only the fluidization of the main loop.

In Chapter 2.6 the measurement principle is discussed: An electric conductor is winded to a coil and exhibit, when a current is applied, a distinctive inductance. At the time when a ferromagnetic particle ($\mu_r >> 1$) passes through the coil, the inductance of the coil changes proportional to the mass of the particle passing. The detection system measures the change of the impedance of the coil by means of a carrier amplifier.

Before the CFM was fluidized and the measurement could be started, the magnetic tracer particles were added to the bed inventory (about 0.5 % of the mass of the bed inventory). During a fluidization operation permanent magnets, which are fixed outside at the air reactor cyclone (*Figure 3-7*) and negligibly change the flow conditions, separate the tracer particles from the mixture. *Figure 3-8* shows the permanent magnets in closed and opened position.

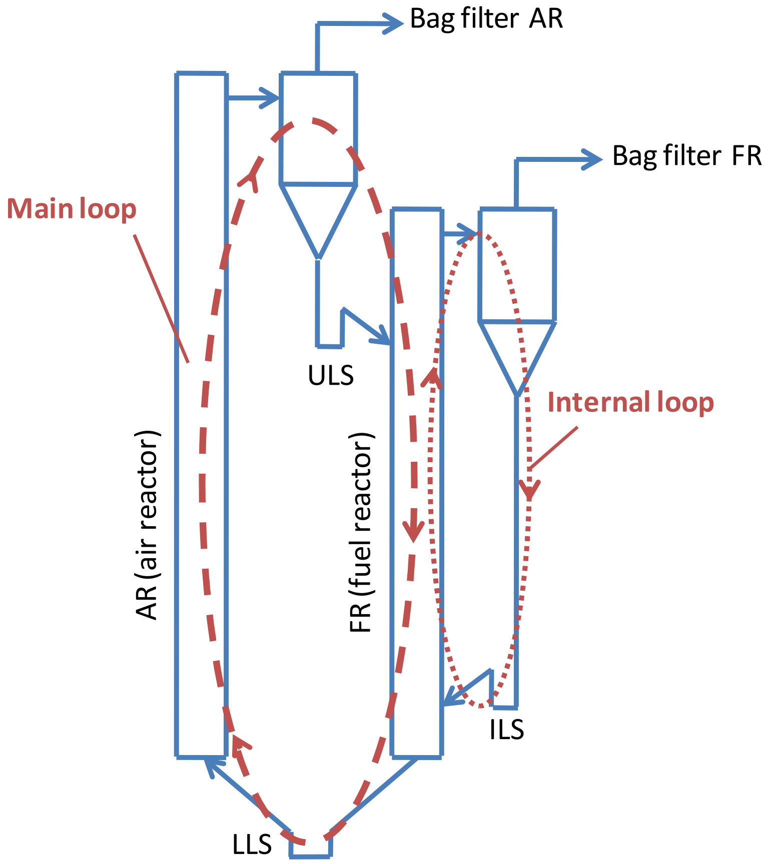

Figure 3-6: Main and internal loop of the CFM.

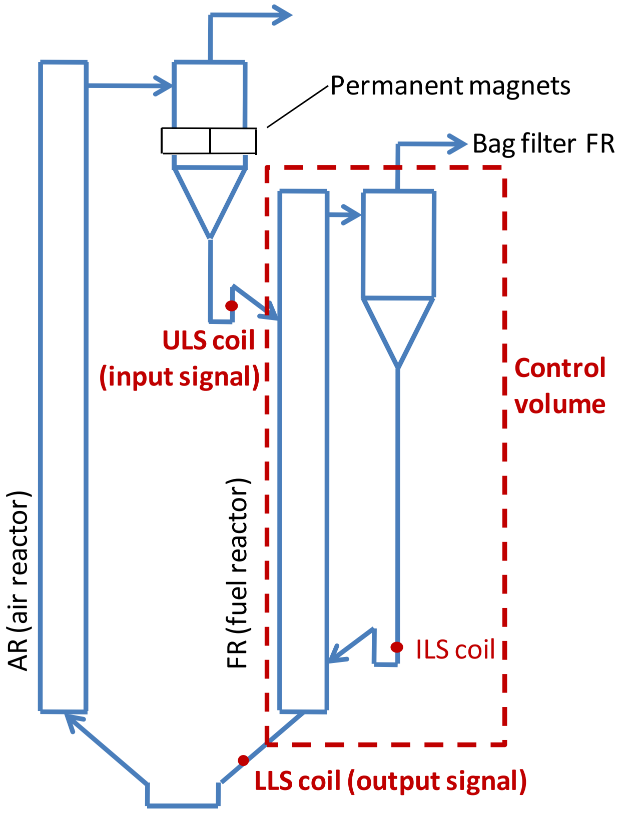

Figure 3-7: Control volume for RTD measurements, location of detections points.

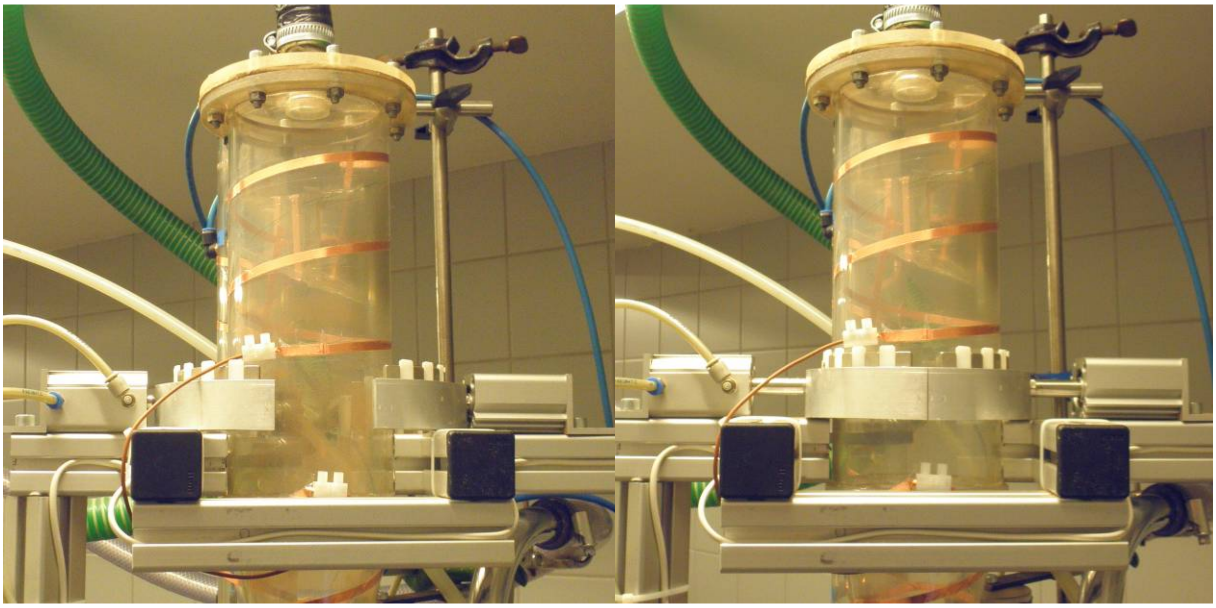

Figure 3-8: Permanent magnets in opened (left) and closed (right) position.

To achieve a pulse input signal, the permanent magnets were opened using hydraulic cylinders and released at a certain moment all the tracer particles. Then the particles entered the fuel reactor through the ULS, where the ULS coil detected the concentration signal of the ferromagnetic particles passing. This was taken as input signal. When the particles passed through the LLS, the signal of the LLS coil was detected as well and taken as output signal.

For the detection system a carrier amplifier was used, in connection to an alternating voltage impedance bridge (*Figure 3-9*). To get a result of the testing bridge, the complex calibration condition $\underline{Z}_1\cdot\underline{Z}_4=\underline{Z}_2\cdot\underline{Z}_3$, with the corresponding magnitude ($Z_1\cdot Z_4=Z_2\cdot Z_3$) and phase ($\varphi_1+\varphi_4=\varphi_2+\varphi_3$) conditions, had to be fulfilled. For this reason, the system had been adjusted with two modifiable components (magnitude/phase) before the measurement was started.

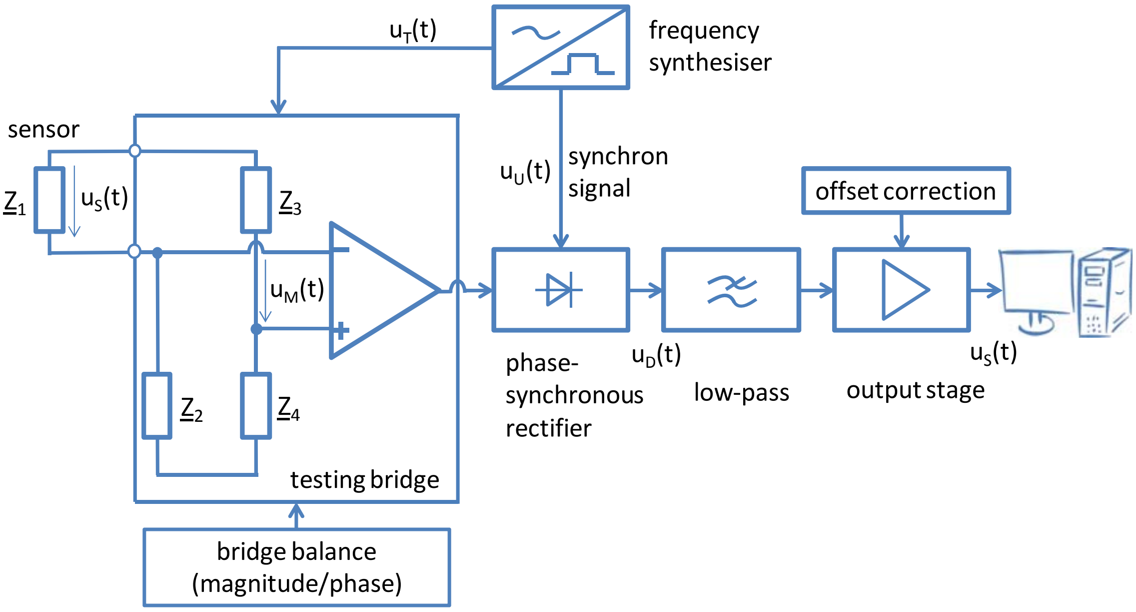

Figure 3-9: Used carrier amplifier for the signal processing.

At the time ferromagnetic particles pass through the coil, the impedance of the coil and the voltage drop changed proportional to the mass of the particles passing. For the low frequency signal of weak amplitude $u_S(t)$ detected by the sensor (namely, the coil) (*Figure 3-10*), the carrier signal $u_T(t)$ (*Figure 3-11*) of the frequency synthesiser multiplies the detected signal, in order to generate a modulated signal with a known carrier frequency and this signal $u_M(t)$ of the bridge circuit becomes the one shown in *Figure 3-12*.

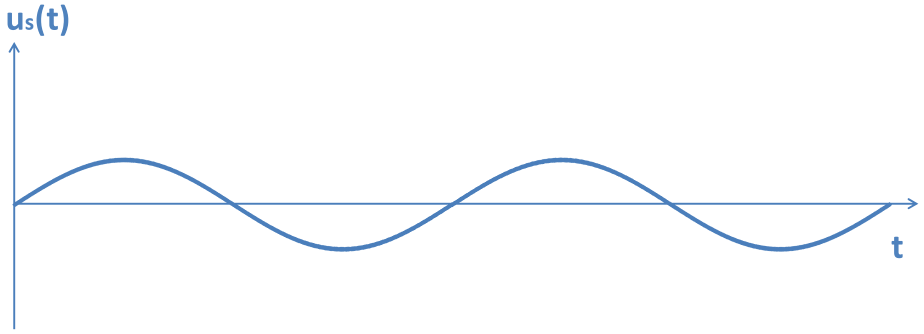

Figure 3-10: Assumed input signal $u_S(t)$.

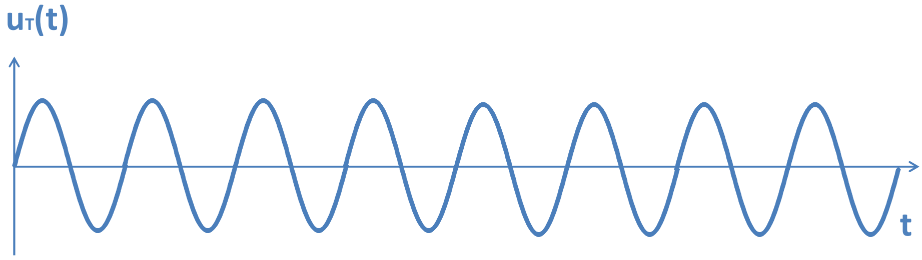

Figure 3-11: Carrier signal $u_T(t)$.

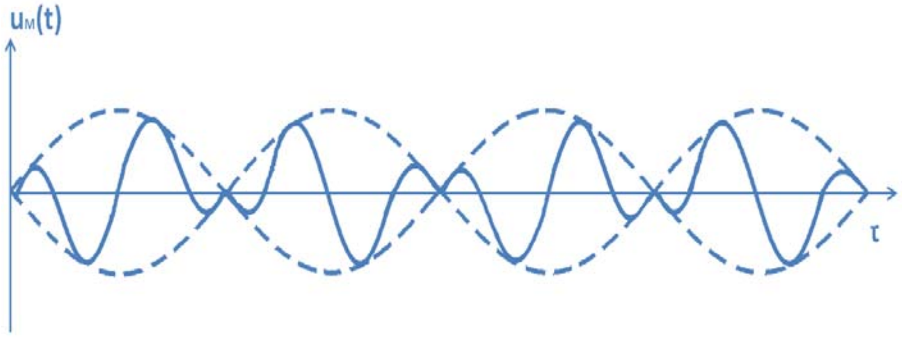

Figure 3-12: Combination of $u_S(t)$ and $u_T(t)$ to $u_M(t)$.

After the bridge circuit, the $u_M(t)$ signal is treated with a phase-synchronous rectifier, which is triggered by the synchronous signal $u_U(t)$ known (*Figure 3-13*). As $u_U(t)$ and $u_T(t)$ have the same frequency, the phases of the signal $u_M(t)$ are synchronised (inverted or not inverted), what leads to the signal $u_D(t)$, shown in *Figure 3-14*.

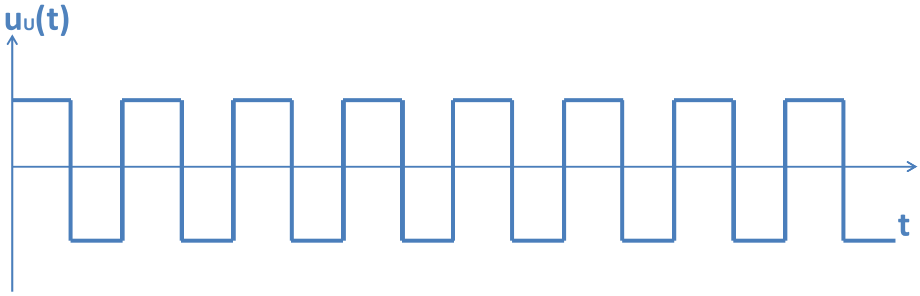

Figure 3-13: Synchronous signal $u_U(t)$.

Figure 3-14: Synchronised signal $u_D(t)$.

To obtain a clear signal $u_S(t)$, $u_D(t)$ was cut by a low-pass filter. This filter cuts the high frequencies and the measured low frequency signal of weak amplitude corresponding to the tracer concentration in the core of the coil (*Figure 3-10*) becomes the amplified signal shown in Figure 3-15.

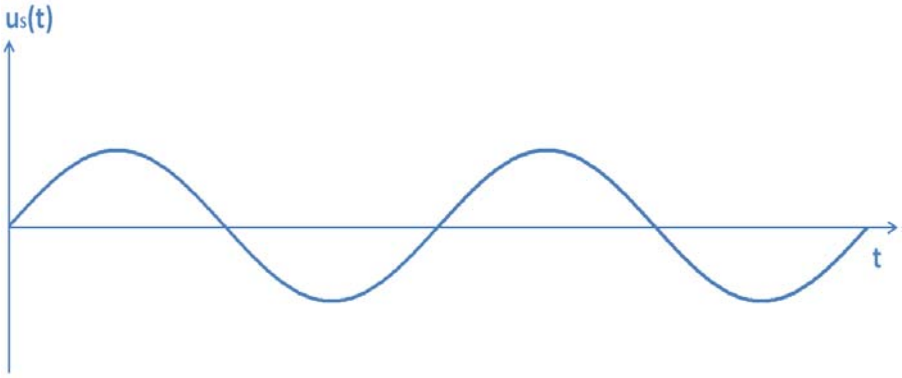

Figure 3-15: Amplified signal $u_S(t)$.

3.4 Data-acquisition system design

The amplified signal was recorded with a program created in National Instruments LabVIEW. The program is divided into two windows ("Front Panel" and "Block Diagram") and creates a file, where the fluidization rates and the measured signals of the coils are stored. After the measurement is finished, this file can be imported to the program Microsoft Excel. Therefore an add-in had been installed in Microsoft Excel, which was downloaded form the homepage of National Instruments. The "Front Panel" is the user interface and is divided into two cards, the *"Conditions of operation"* and an

“Operating card”. The conditions of the operations had been set in the appropriate card before the measurement was started, to store them in the generated file (*Figure 3-16*).

Value FR: 10

Value AR: 15

Value ULS: 1

Value LLS: 1

Value ILS: 0.8

Tracer Material [g]: 3

Saved File: %

Figure 3-16: “Front Panel” card for setting the operating conditions.

The *“Operating card”* showed the measured signals from the coils in a flow chart and the button for the opening and closing operation of the permanent magnets (*Figure 3-17*).

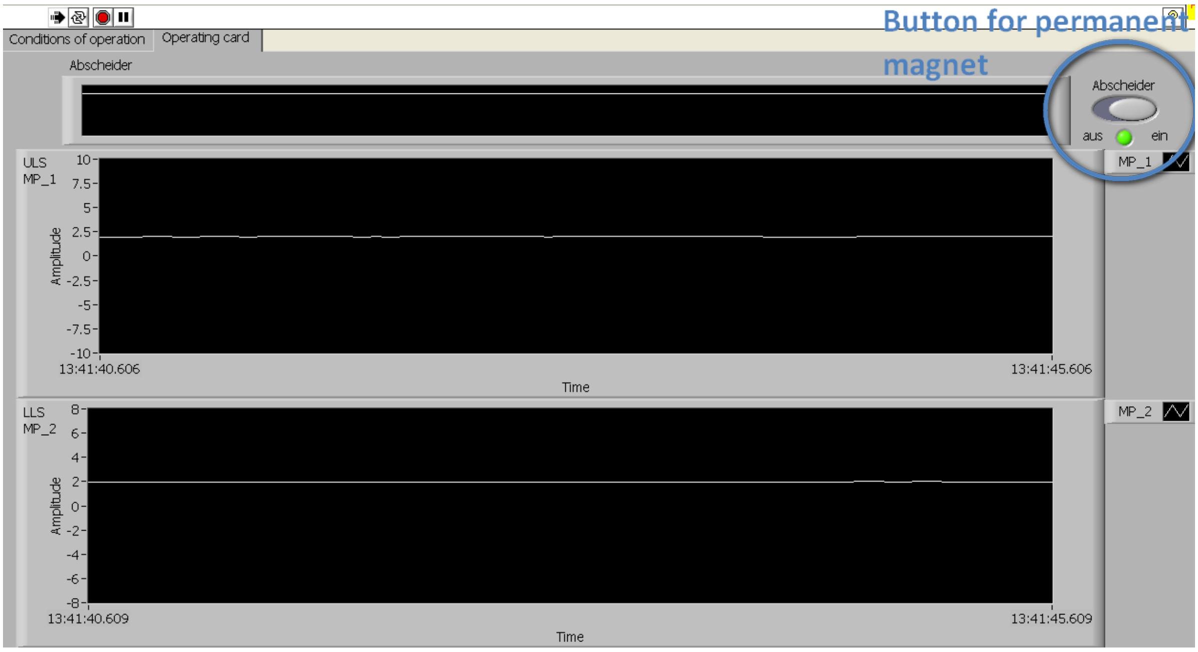

Button for permanent magnet

Figure 3-17: “Front Panel” card with the measured signals in a flow chart.

The “Block Diagram” is the background of the “Front Panel” and shows the analytic construction of the program. The “Block Diagram” of the actual program was divided into three groups: *“Conditions of operation”*, *“Generating a file path”* and *“Signal processing”*. *Figure 3-18* shows the connection scheme of the operating conditions. The conditions set in the “Front Panel” were transformed to SI units and stored in an extra sheet of the generated file in Microsoft Excel.

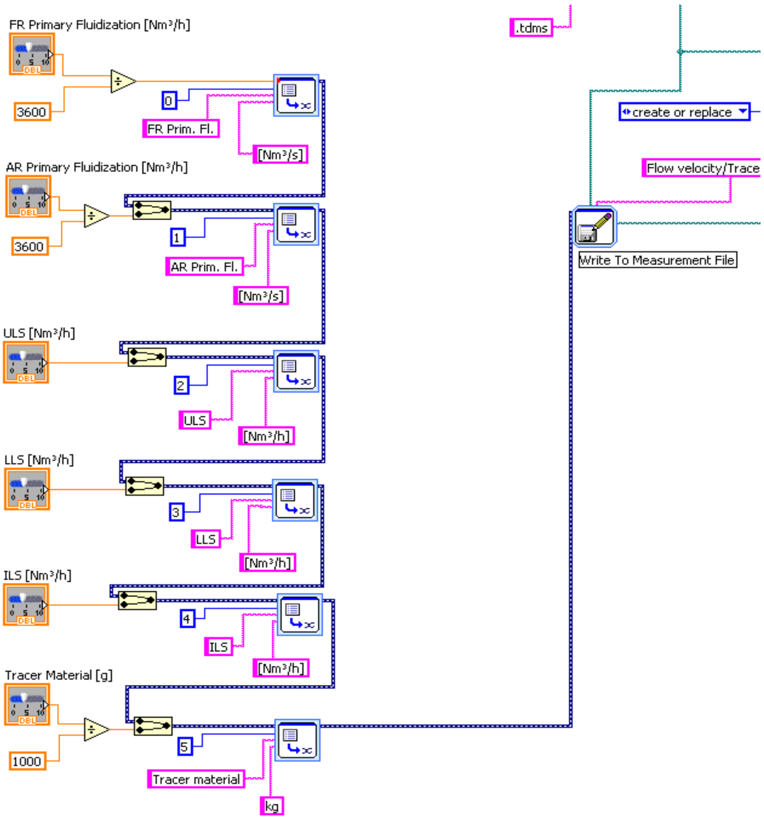

Figure 3-18: Connection scheme of the operating conditions in the “Block Diagram”.

To avoid homonymous file path names, the program created a distinct filename for each measurement. The file path name consists of the memory location, the storage time and the extension “.tdms”, shown in *Figure 3-19*.

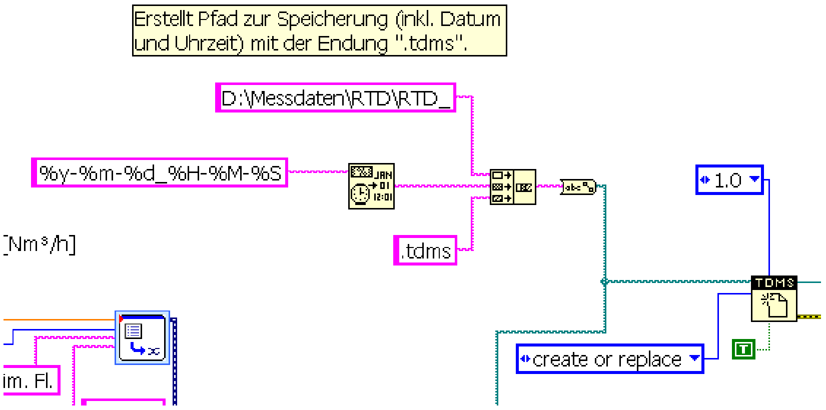
Erstellt Pfad zur Speicherung (inkl. Datum und Uhrzeit) mit der Endung ".tdms".

Figure 3-19: Connection scheme for the file path generation in the “Block Diagram”.

The signal processing unit included the *"Signal output"*, the *"Signal representation"* and the *"Signal recording"* units (*Figure 3-20*). The measured signals (*"Signal output"*) were transferred via the *"DAQ Assistant",* which creates, edits and runs tasks in LabVIEW, to the *"Signal representation*" and the *"Signal recording" units.* The representation unit used the output signals to create real time diagrams of the measured signals. The recording unit stored the output signals in the generated file with the ending ".tdms". After extracting this file to the program Microsoft Excel, the measured signals were then listed with the operating conditions in tabular form.

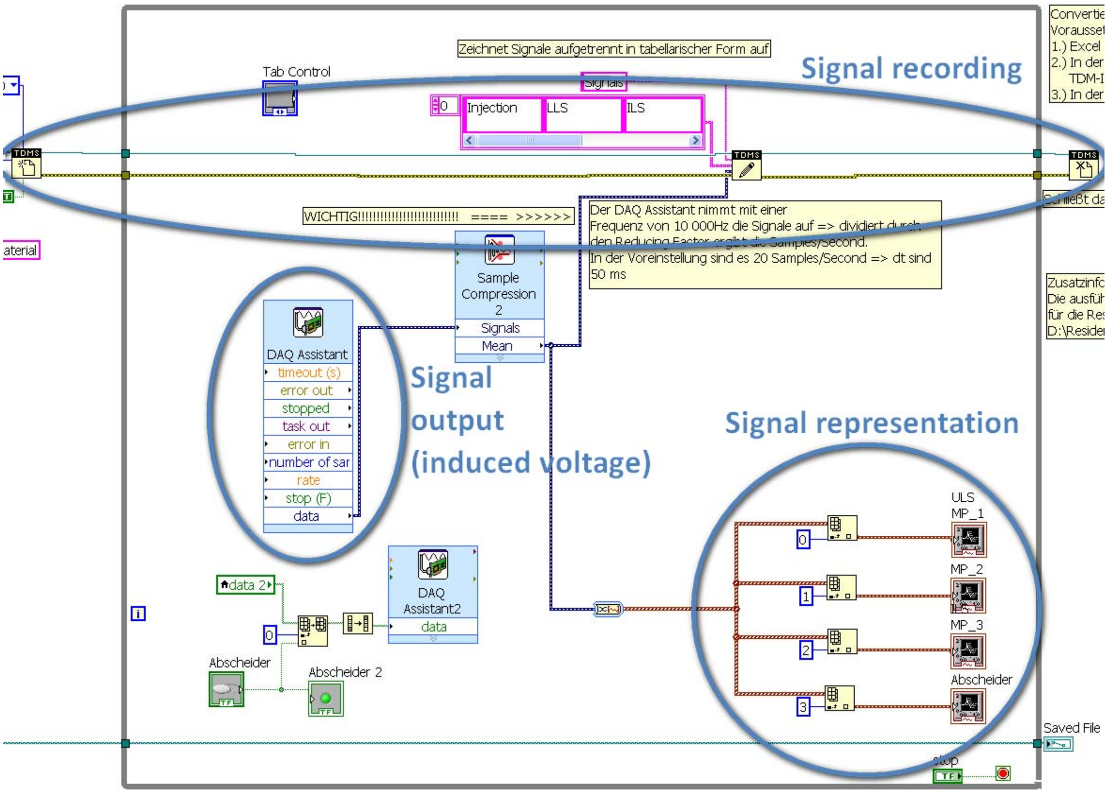

Zeichnet Signale aufgetrennt in tabellarischer Form auf

WICHTIG!!!!!!!!!!!!!!!!!!!!!!!!!!! ==== >>>>>>

Der DAQ Assistant nimmt mit einer Frequenz von 10 000Hz die Signale auf => dividiert durch den Reducing Factor ergibt die Samples/Second.
In der Voreinstellung sind es 20 Samples/Second => dt sind 50 ms

Figure 3-20: Connection scheme of the signal processing unit in the "Block Diagram".

3.5 Calibration of measurement

As described in Chapter 2.6.2, the inductance of a coil was evaluated by using an LC resonator with a known capacity and the linear calibration curve was determined for different ferromagnetic particle concentrations. On this basis the dependency of the measured signals of a coil of the CFM was evaluated in correlation to the mass of the ferromagnetic tracer particles passing. After a certain number of measurements the inventory is taken out of the model and the magnetic particles are separated. A complete separation is not possible therefore the expression "cleaned bronze particles" is used. The calibration of the measurement for the CFM was started with an addition of 0.5 g ferromagnetic particles to the cleaned bronze particles. Then the fluidization conditions, shown in Table 3-4, were set. After a time of circa 2 min, when the particles were assumed to be homogenously mixed, the permanent magnets were closed and started collecting the tracer particles. About 3 min later, when the tracer particles were collected together on the inside of the cyclone, the magnets were opened and the tracer particles flew through the ULS to the fuel reactor.

Table 3-4: Fluidization conditions for the calibration of the measurement.

Component	**Fluidization rate [Nm³·h⁻¹]**
AR	20
FR	10
ULS	1
LLS	1
ILS	0.7

To obtain a calibration curve, the amount of the ferromagnetic particles was increased in 0.5 g steps and the response curve of the measured signals of the coil placed at the ULS was stored. A section of the response curve of the ULS after an addition of 2 g ferromagnetic particles in total and an offset correction is shown in *Figure 3-21*.

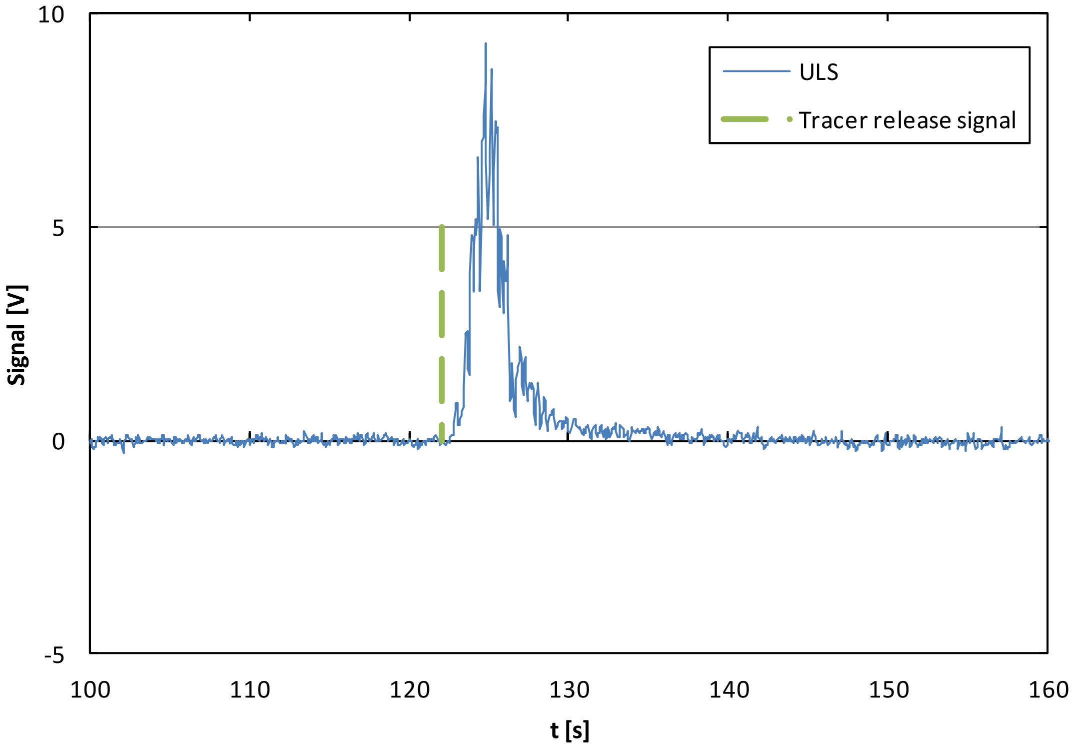

Figure 3-21: Section of the response curve of the ULS coil.

The calibration curve is shown in *Figure 3-22* and the corresponding voltage values with the associated added ferromagnetic particle mass in total are shown in Table 3-5. The greater the mass of the tracer particles passing the coil was the higher was the measured signal in the ULS. Due to the use of the cleaned bronze particles, a small amount of ferromagnetic tracer particles was present in the bronze particles before the calibration started. Therefore the extension of the calibration line does not start at the origin of the diagram.

Table 3-5: Evaluated ULS peak values with the corresponding added magnetic particle mass.

Total added ferromagnetic particles [g]	**Peak [V]**
0,5	2.91
1	5.21
1.5	7.76
2	9.31
2.5	11.13
3	13.40

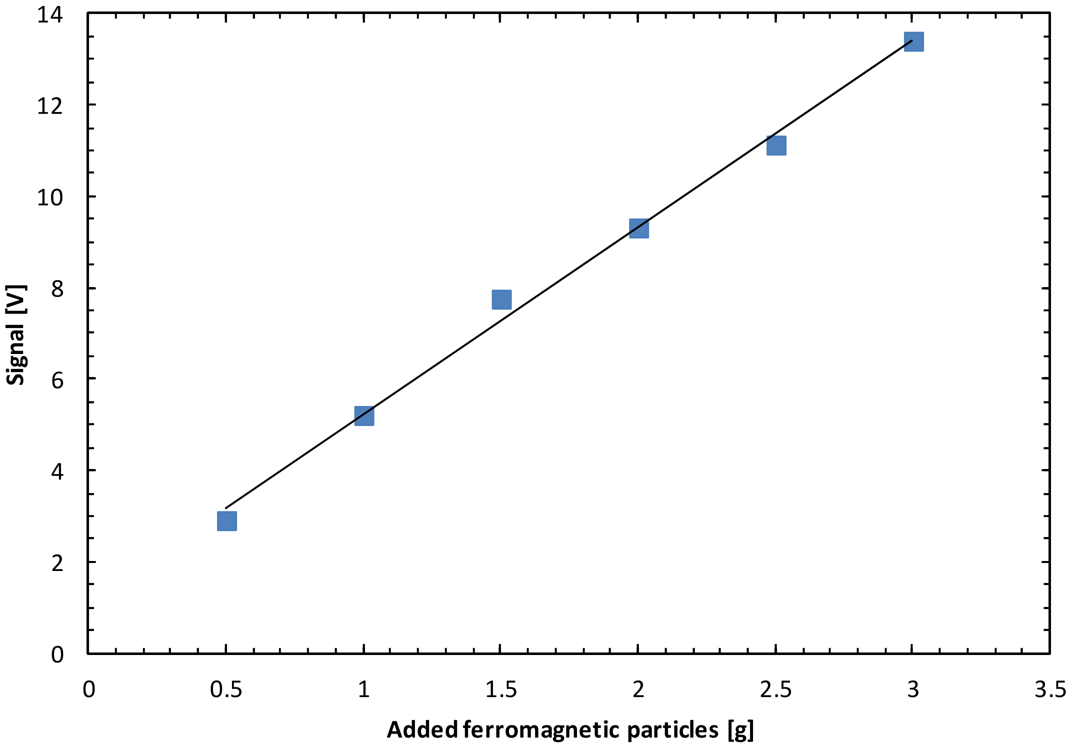

Figure 3-22: Calibration curve of the ULS peak values to the added magnetic particles.

Sometimes the magnetic particles were sticking on the internal side of the cyclone wall, when the permanent magnets were opened and had not been flown downwards against the ULS before the permanent magnets were closed again or they reached the ULS in only small quantities. Both cases were leading to a distorted signal and therefore the measurement had to be repeated until an appropriate, not distorted signal curve was achieved.

3.6 Experimental procedure

Before the measurement could be started, the devices had to reach the operating temperature, which was achieved, after a turn-on time of about 2 hours. Then the CFM was fluidized with air and the permanent magnets started collecting the ferromagnetic particles. At this stage, the loop seals were fluidized at higher rates than during normal operation, to shift the ferromagnetic particles out of the areas of difficult access. Thereafter the program created with National Instruments LabVIEW was started and the recording of the signals of the coils activated.

A certain time later (about 10 min), the desired fluidization regime was set and the permanent magnets were opened to release the ferromagnetic particles. In order to avoid an interference of the signals due to the ferromagnetic particles, that would pass the coil placed around the ULS again after a complete circulation loop, the permanent magnets were closed shortly after (about 5 seconds) they had been opened and started collecting again.

To achieve consistent results, only one parameter of the fluidization conditions was changed (e.g. the fluidization rate of the ULS) and the corresponding solids circulation rate for every variation of a parameter was calculated.

After every series of tests the weight of the filters of the air- and fuel reactor cyclones was determined and the amount of the particles that had been carried out during the experiment, were refilled.

The particles circulation rate for every fluidization condition was determined on the basis of the assumption, that the rate in the downcomer under the cyclone of the air reactor is equal to the rate in the air reactor itself. It was measured by closing the fluidization of the ULS and counting the time the particles needed to reach a certain level. Then the filled volume of the downcomer was calculated and divided by the measured time.

3.6.1 Variation of the ULS fluidization velocity

As one point of this thesis, the influence of the fluidization rate of the ULS on the residence time was investigated. The fluidization conditions are shown in Table 3-6. The ULS fluidization was varied (0.8, 1.5 and 2 $Nm^3 \cdot h^{-1}$). For every set of conditions three measurements were accomplished and the solids circulation rate for every variation was determined too. After a change of the fluidization rate of the ULS the bag filters of the two cyclones were weighed and the amount of the elutriated particles was refilled.

Table 3-6: Fluidization conditions for the variation of the ULS fluidization.

Component	**Fluidization rate [$Nm^3 \cdot h^{-1}$]**
AR	20
FR	15
LLS	1
ILS	0.75
ULS	varied (0.8, 1.5, 2)

3.6.2 Variation of the global solids circulation rate

Another point of the thesis was the investigation of the particle residence time distribution in the fuel reactor depending on the global solids circulation rate, while the internal loop was not fluidized (Chapter 3.3). Thus, the particles were not carried out of the fuel reactor in the cyclone of the FR. The fluidization rate of the air reactor was varied from 10 to 20 $Nm^3 \cdot h^{-1}$, the rate of the ILS was zero and the rate of the FR was kept below 4 $Nm^3 \cdot h^{-1}$, to avoid an elutriation of the particles in the internal loop. The two loops are illustrated in *Figure 3-6*. The fluidization rate of the ULS and LLS was 1 $Nm^3 \cdot h^{-1}$.

For every variation of the solids circulation rate three measurements were accomplished and the corresponding circulation rates were determined. After every change of the fluidization rate, the bag filter of the AR cyclone had been weighed out and the amount of the particles elutriated was refilled.

When the global solids circulation rate was decreased, the amount of the fluidized particles in the FR was decreasing too. Therefore the pressure drop from the top to the bottom of the fuel reactor was measured by pressure cells and the recorded values were stored in Microsoft Excel files. If the pressure drop between the bottom and the top of the fuel reactor would be nearly equal, the amount of bronze particles in the reactor was assumed to be the same. To achieve nearly the same bed inventory in the fuel reactor for every experiment and an equal pressure drop respectively, a particle injection system was installed at the LLS (*Figure 3-23*), which was filled with bronze particles. If the pressure drop decreased due to the decrease of the solids circulation rate and the lack of the particles in the reactor, the particle injection system lifted the pressure drop to the starting level, by adding bronze particles to the system.

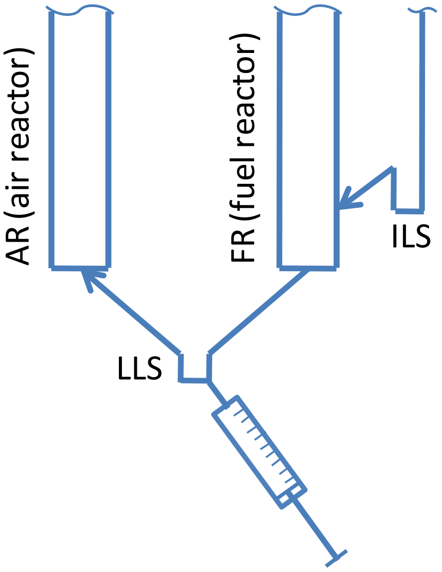

Figure 3-23: Sketch of the CFM with the device for adjusting the particle inventory.

3.6.3 Variation of the FR fluidization velocity

The influence of the FR fluidization on the residence time in the main loop was also investigated. The fluidization rate of the air reactor was varied from 10 to 20 $Nm^3 \cdot h^{-1}$ and the rate of the FR was kept again below 4 $Nm^3 \cdot h^{-1}$, to avoid an elutriation of the particles in the internal loop.

For every variation of the fuel reactor fluidization (2 $Nm^3 \cdot h^{-1}$ and 4 $Nm^3 \cdot h^{-1}$) three measurements were accomplished and the corresponding solids circulation rates were determined. After every change of the fluidization conditions, the bag filter of the AR cyclone had been weighed out and the amount of the elutriated particles was refilled.

When the fluidization rate of the fuel reactor was increased from 2 to 4 Nm³/h, a negligibly small amount of the particles was flowing through the cyclone of the FR towards the internal downcomer. Therefore the ILS was shortly fluidized just before the measurements were started, to move the elutriated material from the ILS to the fuel reactor and provide the same bed inventory for every experiment.

3.6.4 Signal processing

The signal converting process is described on the basis of one measurement (AR = 20 $Nm^3 \cdot h^{-1}$, FR = 15 $Nm^3 \cdot h^{-1}$, LLS = 1 $Nm^3 \cdot h^{-1}$, ULS = 0.8 $Nm^3 \cdot h^{-1}$, ILS = 0.75 $Nm^3 \cdot h^{-1}$). When the program for the measurement was started in LabVIEW, a file with the extension ".tdms" was created, which contained the recorded signals of the coils. This file was imported in the calculation program Microsoft Excel and saved as an Excel file.

In the first step a time column from zero in 0.05 s steps until the end of the signal column was created because the program recorded every 0.05 s the corresponding voltage values. Then the signals could be drawn, against the absolute time (*Figure 3-24*).

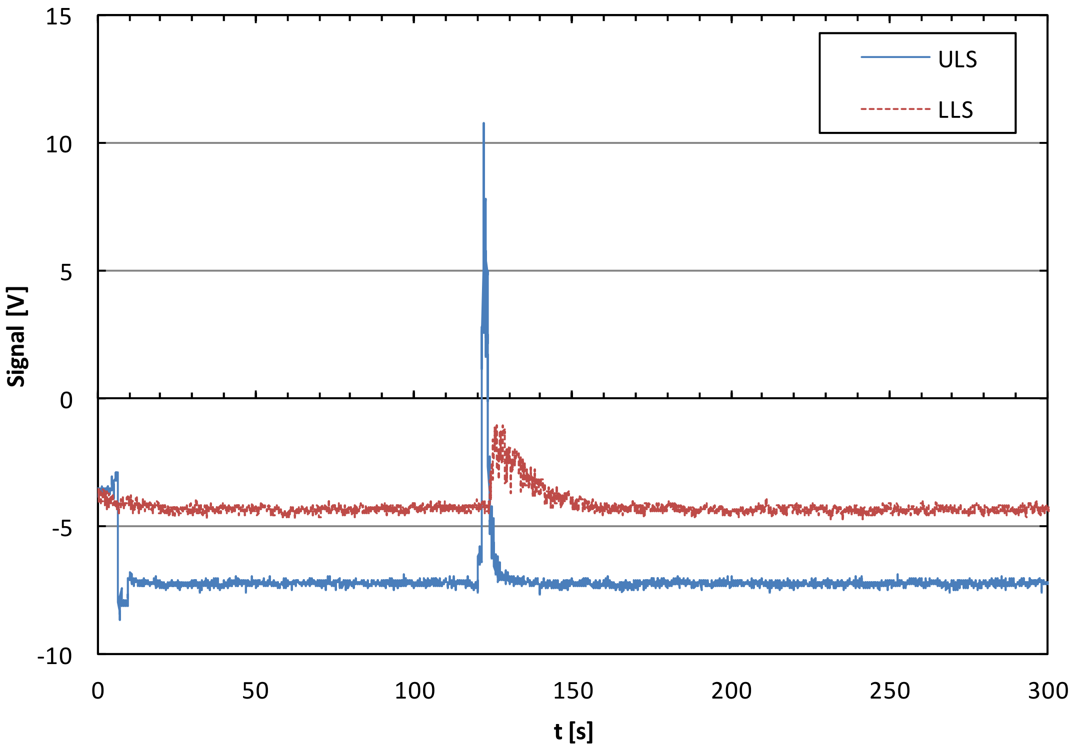

Figure 3-24: ULS and LLS signal curves of an ULS fluidization variation experiment.

An offset corrector was arranged in the second step. The average voltage value in a certain range of the recorded signals was calculated and subtracted from every voltage value of the measurement. This shifted the signals on an equal level (*Figure 3-25*). The range was chosen with respect to the signal characteristic. For example, the first 20 seconds of this measurement were not used for the offset correction, due to the inconstant trend caused by the adjustment of the measurement system. The calculation of the average voltage value was done, where the voltage values show a constant trend.

The measured signals showed when no ferromagnetic particles were passing through the coils a constant characteristic (=offset) but as well a background noise in a small range of about +/- 0.1 V. As the ferromagnetic particles were passing through the coils the measured signals showed a significant increment (*Figure 3-25*).

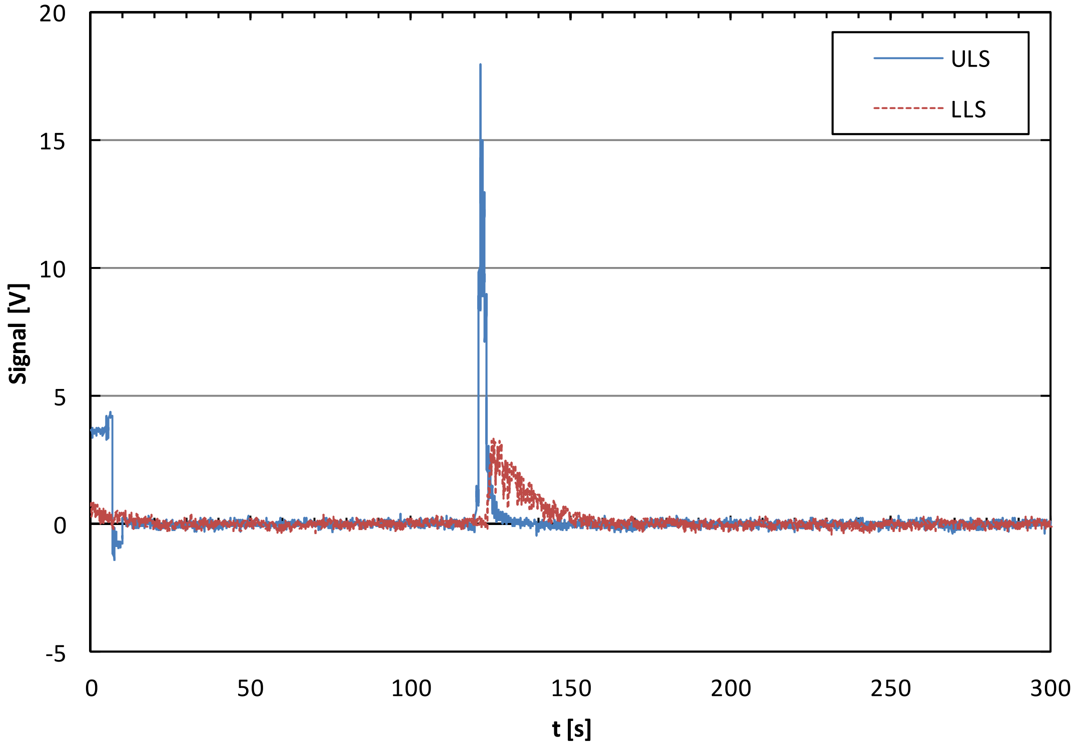

Figure 3-25: ULS and LLS signal curves after the offset correction.

In the next step, a certain section was chosen which started from the first increment of the signal and ended where the measured signals decreased and reached the level of the offset again (Figure 3-26).

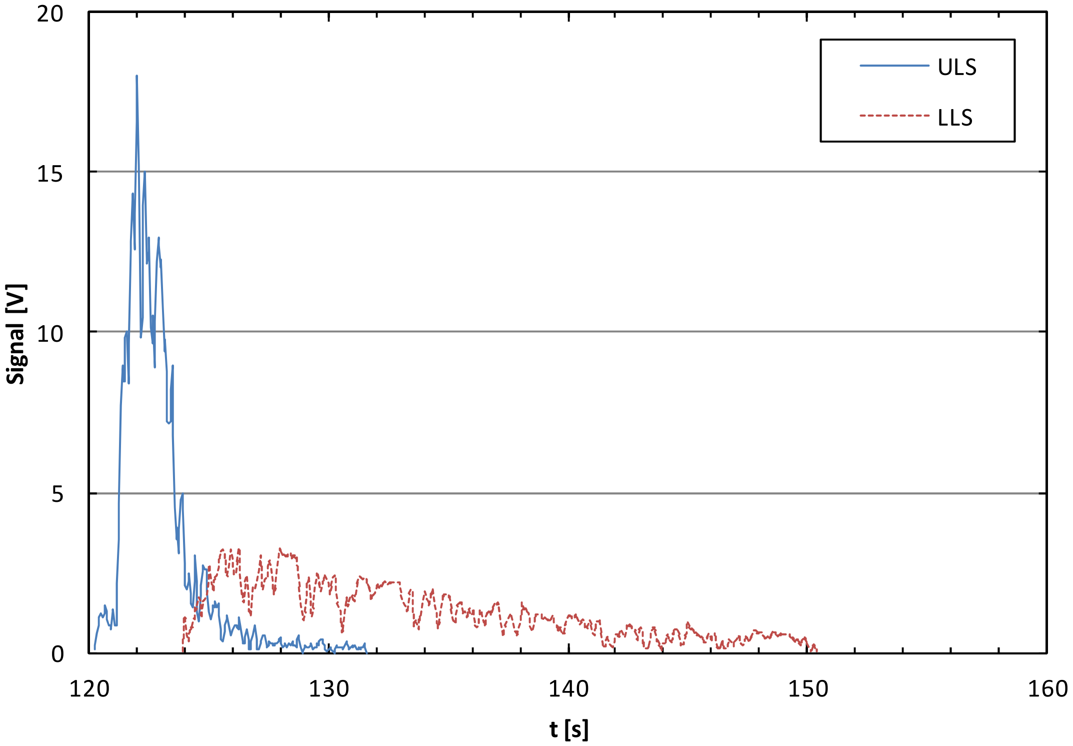

Figure 3-26: *Section of the injection and LLS signal curves.*

For the calculation of the mean residence time, the output response curve is usually based on the Dirac delta input function (discussed in Chapter 2.4.1). As a Dirac delta function is just feasible in electrical engineering, the recorded input signals showed deviation of the Dirac delta function. Therefore in the last step the centres of the areas under both curves were determined according to equation (3.1) and shown in *Figure 3-27*. The difference between the centres of the areas of the output (LLS signal) and the input (ULS signal) signals was the particle mean residence time for the fuel reactor in the main loop of the CFM.

The normalized curves for every measurement were calculated as well, by dividing the signals by the area below the curve, according to equation (3.2). Then the areas below the normalized curves became unity.

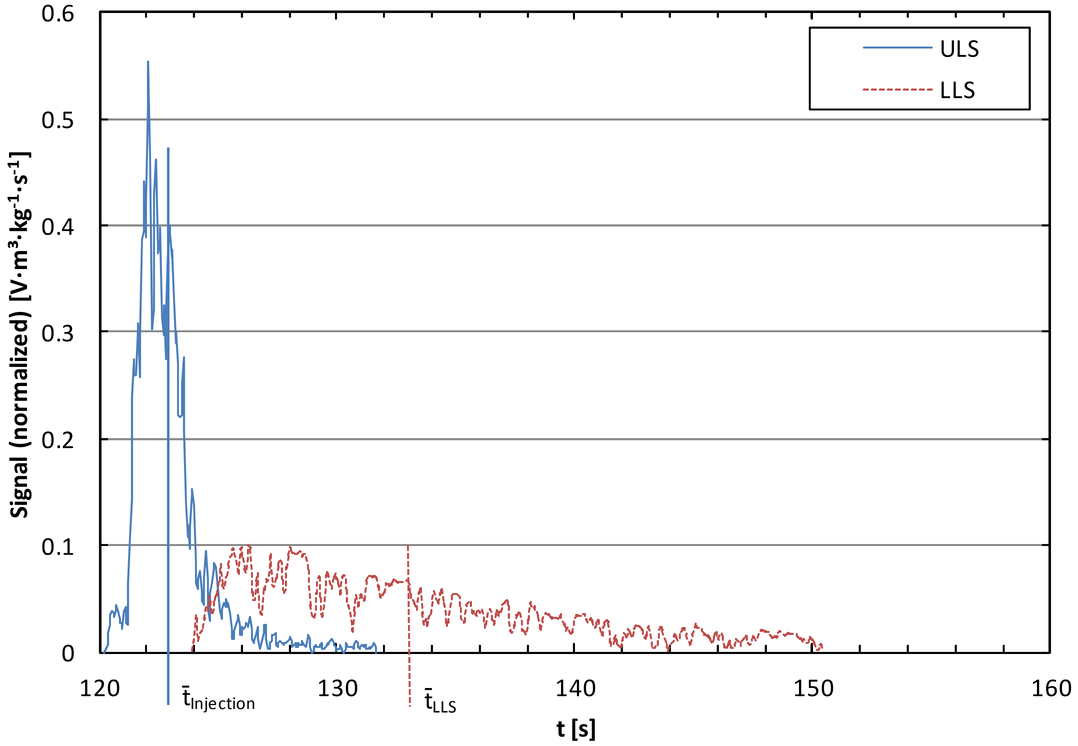

Figure 3-27: Normalized signal curves of the injection and LLS signal.

Moreover, the variances of the input and output signals were determined according to (3.3). The calculation steps explained in this chapter were done for every measurement. In Appendix A five other measurements with the corresponding normalized curves are shown.

3.6.5 Evaluation of the residence time distribution, the normalized curve and the variance

The mean residence time was calculated from the recorded voltage values and the corresponding times, as discussed in Chapter 2.4, with the equation:

$$\tau = \bar{t}_{out} - \bar{t}_{in} = \frac{\int_0^\infty t_{out} \cdot C_{out} \cdot dt}{\int_0^\infty C_{out} \cdot dt} - \frac{\int_0^\infty t_{in} \cdot C_{in} \cdot dt}{\int_0^\infty C_{in} \cdot dt} \tag{3.1}$$

$$\cong \frac{\sum_i t_{i,out} \cdot C_{i,out}}{\sum_i C_{i,out}} - \frac{\sum_i t_{i,in} \cdot C_{i,in}}{\sum_i C_{i,in}}, [\Delta t = constant].$$

The normalized curve $C_n(t)$ was given by dividing the C_{pulse} signals by the area under the measured curve:

$$C_n(t) = \frac{C_{pulse}}{\sum C_i \cdot \Delta t_i} \tag{3.2}$$

The variance was defined as

$$\sigma^2 = \frac{\int_0^\infty (t - \bar{t}_S)^2 \cdot C \cdot dt}{\int_0^\infty C \cdot dt} \cong \frac{\sum (t_i - \bar{t}_S)^2 \cdot C_i \cdot \Delta t_i}{\sum C_i \cdot \Delta t_i} \tag{3.3}$$

and was determined for every input and output signal as well.

The vessel dispersion numbers were calculated according to equation (2.21). In a range from 0.01 to 1 are no analytic expressions available for the calculation of the variance (Levenspiel, 1999). Therefore equation (2.19) was used to approximate the timeless variance for closed boundaries, what leaded to the following equation:

$$\sigma_{\theta cc}^2 = \frac{\sigma_{out}^2 - \sigma_{in}^2}{(\bar{t}_{out} - \bar{t}_{in})^2} = \frac{\sigma^2}{(\tau)^2} = 2 \cdot \left(\frac{\boldsymbol{D}}{\mathrm{u} \cdot L}\right) - 2 \cdot \left(\frac{\boldsymbol{D}}{\mathrm{u} \cdot L}\right)^2 \cdot \left[1 - e^{-\frac{u \cdot L}{\boldsymbol{D}}}\right]. \tag{3.4}$$

4 RESULTS AND DISCUSSION

A study of the dependence of the mean particle residence time in the fuel reactor on three different variables has been accomplished:

- ULS fluidization velocity.
- Global solids circulation rate.
- Fuel reactor fluidization velocity.

In Chapter 4.3 a PFR and CSTR connection in series model is correlated to the output voltage signals and the mean residence time of these ideal reactors was investigated as well.

According to Rupanovits, 2007, the LLS fluidization rate has no significant influence on the solids circulation rate, when it is increased above a value of 1 $Nm^3 \cdot h^{-1}$. The influence of the ULS fluidization velocity is discussed in Chapter 4.1. Since the internal loop was not fluidized, the influence of the ILS fluidization velocity is not discussed.

The mean residence times and the variances of the input and output signals according to (3.1) and (3.3) were calculated for every fluidization variation. As the downcomer of a circulating fluidized bed and the fuel reactor of the CFM respectively exhibit different flow conditions at the entrance and the exit of the reactor, the dimensionless variances with the corresponding vessel dispersion number are calculated according to equation (3.4).

4.1 Variation of the ULS fluidization

The ULS fluidization was varied from 0.8 to 2 $Nm^3 \cdot h^{-1}$. The calculated values are listed in Table 4-1.

Table 4-1: Residence times, variances and VDNs according to the ULS fluidization variation.

ULS [$Nm^3 \cdot h^{-1}$]	τ [s]	**Average τ [s]**	σ^2_{ULS} [s^2]	σ^2_{LLS} [s^2]	σ^2_{θ} [-]	$\frac{D}{u \cdot L}$ [-]	**Average $\frac{D}{u \cdot L}$ [-]**
0.8	10.19	**10.19**	2.50	42.21	0.38	0.25	**0.29**
	10.16		3.18	49.87	0.45	0.33	
	10.21		1.93	44.70	0.41	0.28	
1.5	10.13	**9.95**	2.64	47.24	0.43	0.31	**0.26**
	11.33		2.83	55.72	0.41	0.28	
	8.38		5.81	27.43	0.31	0.19	
2	10.75	**10.55**	4.38	51.51	0.41	0.28	**0.34**
	11.41		3.65	74.14	0.54	0.45	
	9.49		4.52	40.81	0.40	0.28	

It can be said, that the ULS fluidization had no influence on the particle residence time since all the values of the calculated residence times showed no significant difference, the vessel dispersion numbers are very similar as well. The variances of the output signals showed no significant difference for each variation as well. With increasing ULS fluidization rate it was expected, that the variances would take smaller values, due to the higher velocity of the fluidization fluid in the ULS and the assumption of a plug flow regime through the ULS, but the variances of the injection signals increased with the fluidization rate. It can be concluded, that at higher ULS fluidization rates higher turbulences are achieved and thus the particle movement was increasing and lead to a broader injection signal. As the fluidization velocity of the ULS had no significant influence on the particle residence time, the rate was set to 1 $\mathrm{Nm^3 \cdot h^{-1}}$ for the following measurements.

4.2 Variation of the global solids circulation rate and the fuel reactor fluidization

The global solids circulation rate was varied by the air reactor fluidization (10 to 20 $\mathrm{Nm^3 \cdot h^{-1}}$) and the values for the mean residence time, the variances of the input and output signals and the vessel dispersion numbers were determined. In Table 4-2 and Table 4-3 the values are listed.

Table 4-2: Determined values for the variation of the solids circulation rate (FR = 2 $\mathrm{Nm^3 \cdot h^{-1}}$).

AR [$\mathrm{Nm^3 \cdot h^{-1}}$]	**Solids circulation rate [$\mathrm{kg \cdot m^{-2} \cdot s^{-1}}$]**	**FR = 2 $\mathrm{Nm^3 \cdot h^{-1}}$**						
		τ [s]	**Average τ [s]**	σ^2_{ULS} [s^2]	σ^2_{LLS} [s^2]	σ^2_{θ} [-]	$\frac{D}{u \cdot L}$ [-]	**Average** $\frac{D}{u \cdot L}$ [-]
10	**22.10**	22.76	**22.47**	27.13	227.78	0.39	0.26	**0.23**
		23.86		26.36	245.72	0.39	0.26	
		20.80		20.80	138.22	0.27	0.16	
15	**42.38**	11.64	**12.39**	4.92	43.97	0.29	0.17	**0.20**
		12.92		5.23	60.52	0.33	0.21	
		12.60		5.16	61.15	0.35	0.23	
20	**64.15**	8.82	**9.37**	4.36	25.94	0.28	0.17	**0.17**
		9.79		5.11	32.43	0.29	0.17	
		9.49		4.07	29.71	0.28	0.17	

Table 4-3: Determined values for the variation of the solids circulation rate (FR = 4 $\mathrm{Nm^3 \cdot h^{-1}}$).

AR [$\mathrm{Nm^3 \cdot h^{-1}}$]	**Solids circulation rate [$\mathrm{kg \cdot m^{-2} \cdot s^{-1}}$]**	**FR = 4 $\mathrm{Nm^3 \cdot h^{-1}}$**						
		τ [s]	**Average τ [s]**	σ^2_{ULS} [s^2]	σ^2_{LLS} [s^2]	σ^2_{θ} [-]	$\frac{D}{u \cdot L}$ [-]	**Average** $\frac{D}{u \cdot L}$ [-]
10	**20.92**	20.92	**19.53**	23.12	164.05	0.32	0.20	**0.21**
		18.96		23.08	146.79	0.34	0.22	
		18.71		29.76	139.81	0.31	0.19	
15	**42.71**	10.83	**11.72**	6.16	41.50	0.30	0.18	**0.18**
		12.28		5.88	51.32	0.30	0.18	
		12.04		7.12	47.14	0.28	0.17	
20	**60.17**	7.45	**7.95**	4.10	18.13	0.25	0.15	**0.15**
		7.76		5.13	18.73	0.23	0.13	
		8.63		4.60	25.17	0.28	0.17	

According to Levenspiel, 1999, the space-time (discussed in Chapter 2.4.1) is defined as

$$\tau = \frac{V_R}{\dot{V}} = \frac{Volume\ of\ the\ reactor}{Volume\ flow}, [s]. \tag{4.1}$$

In the case of constant density systems, the mean residence time is equal to the space time and it can be assumed that the volumetric flow is equal to the mass flow as well. Therefore the space-times can be written as follows:

$$\tau = \frac{m_R}{\dot{m}} = \frac{Mass\ of\ particles\ in\ the\ reactor}{Mass\ flow}, [s]. \tag{4.2}$$

The density of the particles used and the fluidization fluid in the CFM did not change and thus it can be supposed that the space-time was equal to the mean residence time. Consequently the residence time should reciprocally dependent on the solids circulation rate. The results obtained confirmed this behaviour, as shown in *Figure 4-1*.

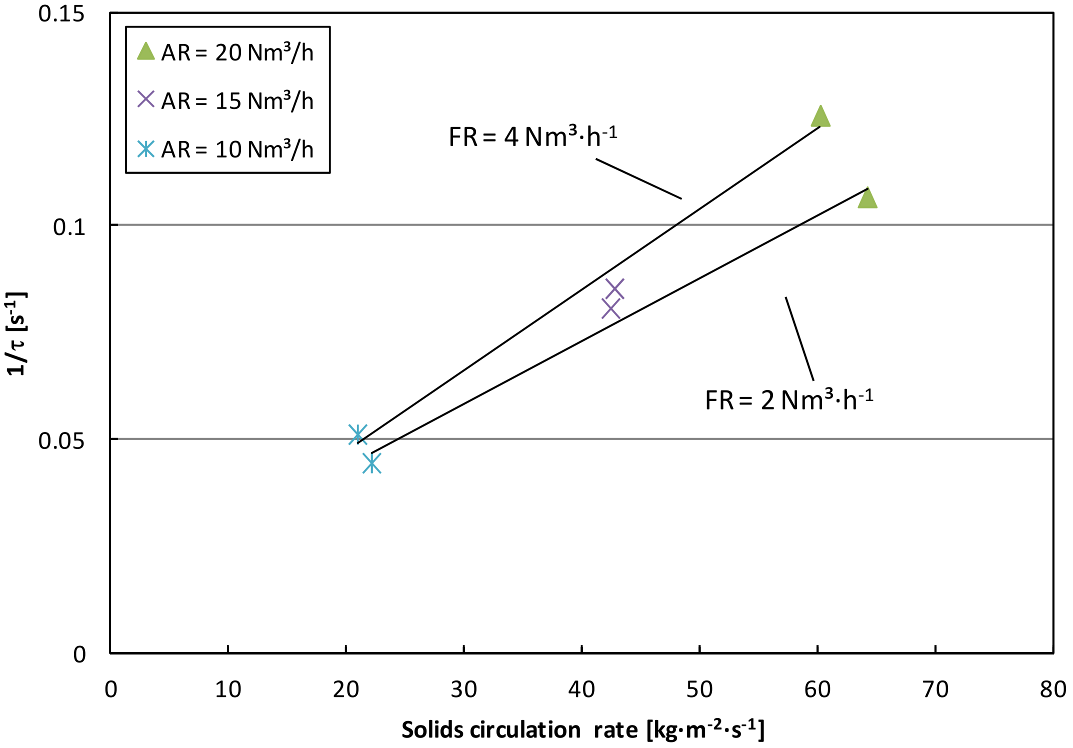

Figure 4-1: Residence times according to the solids circulation rates (FR = 2 and 4 Nm³·h⁻¹; ULS and LLS = 1 Nm³·h⁻¹; ILS = 0 Nm³·h⁻¹).

At a higher solids circulation rate the particles passed faster through the loop seals and for this reason narrower input and output signals were expected. The lower solids circulation rates leaded to wider signal curves and to higher values of the variances respectively, due to the longer particle residence time in the loop seals.

As shown in *Figure 4-2*, the vessel dispersion number decreased with increasing solids circulation rates. This indicates that the flow pattern approaches in a larger extent the plug flow model.

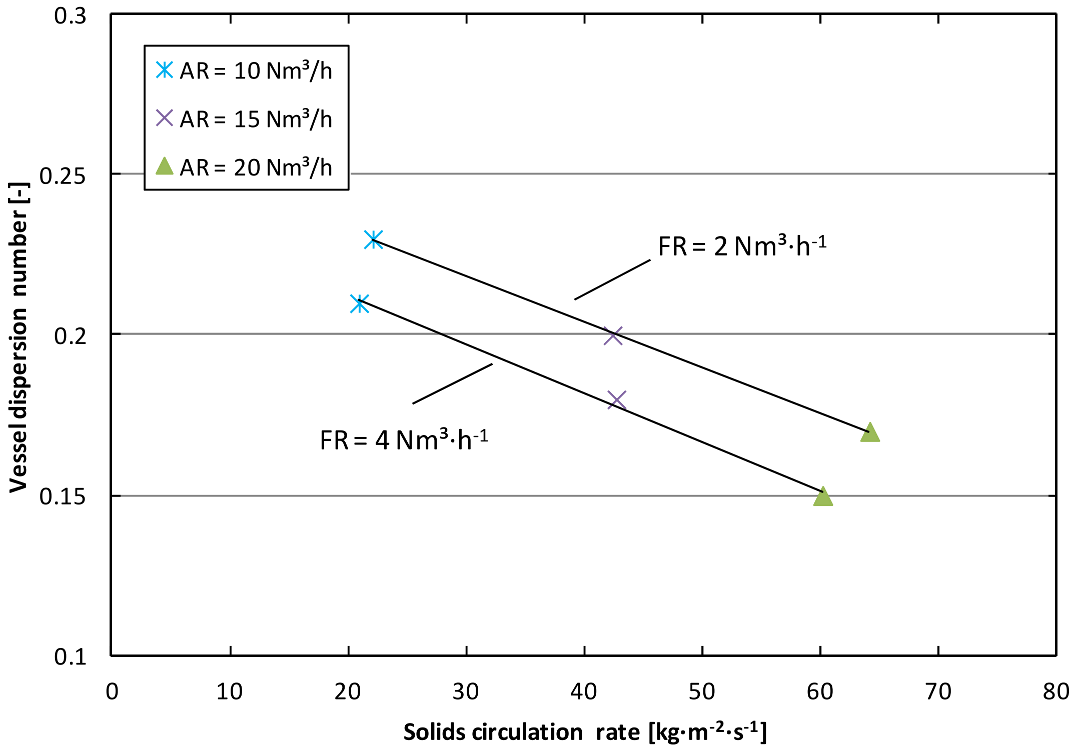

Figure 4-2: Vessel dispersion numbers according to the solids circulation rates (FR = 2 and 4 Nm³·h⁻¹; ULS and LLS = 1 Nm³·h⁻¹; ILS = 0 Nm³·h⁻¹).

The fuel reactor fluidization was varied from 2 to 4 $Nm^3 \cdot h^{-1}$. The mean residence times, variances and vessel dispersion numbers of the variation of the fuel reactor fluidization are listed in Table 4-2 and Table 4-3 as well. It was expected that for higher fluidization rates of the fuel reactor the mass of the particles in the reactor would increase, as well as the residence time.

As shown in Table 4-2 and Table 4-3 the mean residence times of the particles for the experiments operated at FR = 2 $Nm^3 \cdot h^{-1}$ were in general slightly higher than for the experiments performed at FR = 4 $Nm^3 \cdot h^{-1}$. In both cases the fluidization conditions lead to a bubbling bed in the fuel reactor but the pressure difference between the top and the bottom of the fuel reactor was a little higher at the former conditions than at the latter (Table 4-4). This difference indicated a higher mass of the particles in the fuel reactor and therefore according to equation (4.2), higher residence times were achieved (*Figure 4-1*). The experiments carried out at FR = 2 $Nm^3 \cdot h^{-1}$ leaded to wider signal curves of the coil placed at the LLS and to higher values of the variances respectively, in comparison to the higher fluidized fuel reactor.

The values for the vessel dispersion numbers were in general slightly higher for the experiments carried out at the lower fluidization velocity of the fuel reactor (*Figure 2-2*). As mentioned above, the pressure difference indicated a higher particle mass for the experiments carried out at the lower fluidized fuel reactor. Therefore, the dispersion of the particles increased and lead to higher values of the VDN for the lower fluidized fuel reactor.

Table 4-4: Pressure difference between top and bottom of FR.

AR [$Nm^3 \cdot h^{-1}$]	**Average τ [s]**	**FR = 2 $Nm^3 \cdot h^{-1}$** Pressure difference between top and bottom of the FR [mbar]	AR [$Nm^3 \cdot h^{-1}$]	**Average τ [s]**	**FR = 4 $Nm^3 \cdot h^{-1}$** Pressure difference between top and bottom of the FR [mbar]
10	**22.47**	**27.70**	10	**19.53**	**24.02**
15	**12.39**	**27.05**	15	**11.72**	**23.04**
20	**9.37**	**27.13**	20	**7.95**	**23.77**

4.3 Comparison of the simulated PFR and CSTR model to the calculated residence times

The signals obtained from the measurement were extracted into a program, which calculated the residence time assuming a connection in series of a PFR and a CSTR, shown in *Figure 4-3*. Both ideal reactors are described in Chapter 2.4.1. The program calculated an appropriate ***E*** curve based on the measured and normalized input and output signals, according to equation (2.18). Then an appropriate output curve was simulated by the simple RTD model using the measured input signal and fitted to the measured output curve, until the square distance of both output curves reached a minimum. The varying parameters for the adaption on the measured signals were the mean residence time of the PFR and CSTR in the RTD model (*Figure 4-3*). An example of a simulated output curve and a measured input and output curve is illustrated in *Figure 4-4*. In APPENDIX B more simulated curves are shown. They agree well with the measured output curves.

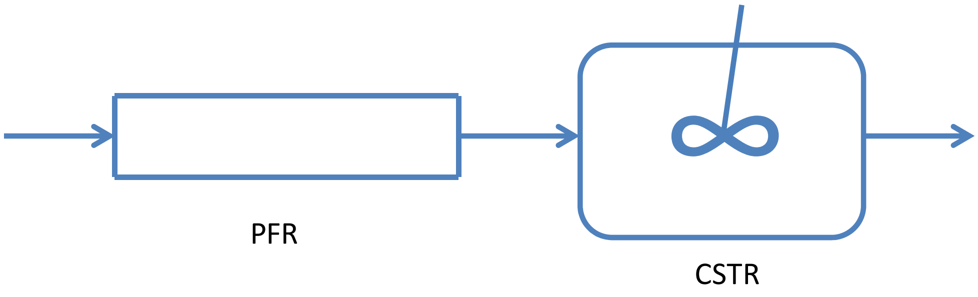

Figure 4-3: Simple RTD model featuring a PFR and CSTR in series.

The calculated residence times of the RTD model are shown in Table 4-5 to Table 4-7 and are composed of a residence PFR time and a residence CSTR time. In general, the residence times added together were larger than the calculated residence times according to Chapter 3.6.5. The differences are probably resulting from the statistic error of the calculation method and the rough signal characteristic, since the error is getting bigger with increasing values of the X axis (time) (see equation (3.1)).

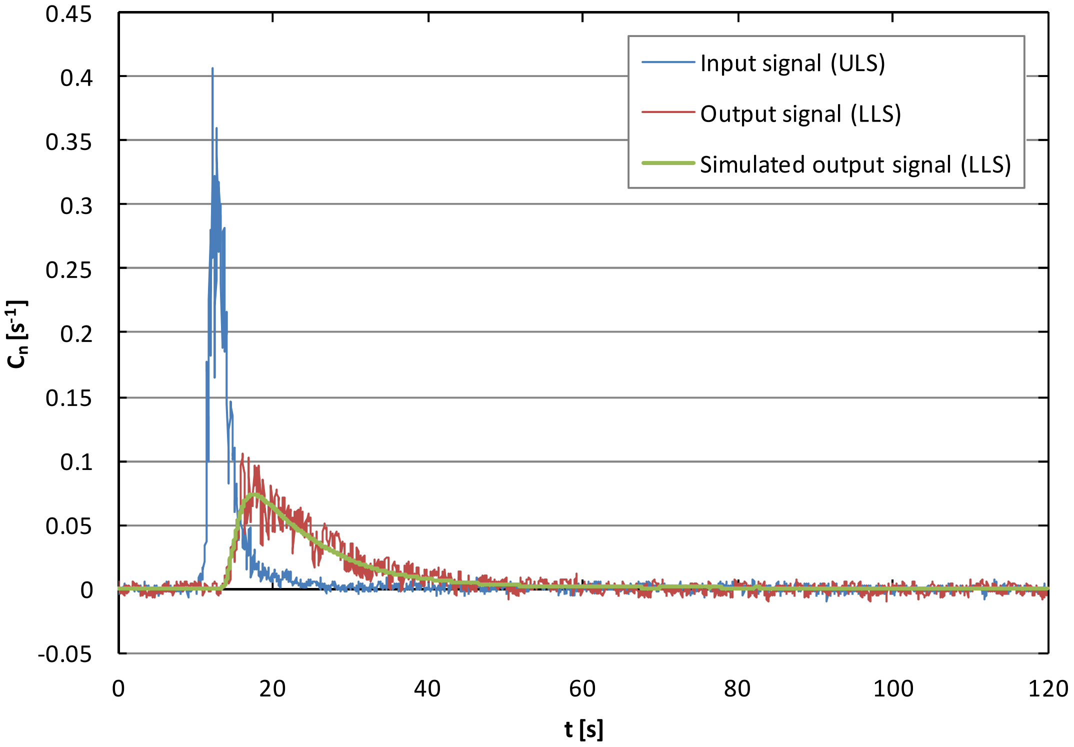

Figure 4-4: Example of simulated output curve with the corresponding measured input and output signals (AR = 20 $Nm^3 \cdot h^{-1}$, FR = 4 $Nm^3 \cdot h^{-1}$, ULS and LLS = 1$Nm^3 \cdot h^{-1}$, ILS = 0 $Nm^3 \cdot h^{-1}$).

The variation of the ULS fluidization had no significant influence on either of the computed residence times (PFR and CSTR) (Table 4-5). The contributions of the PFR and CSTR can be determined from their fraction regarding to the total residence time. The fractions of the residence PFR and CSTR time stayed nearly equal.

Table 4-5: Simulated residence times for the variation of the ULS fluidization.

ULS [$Nm^3 \cdot h^{-1}$]	τ_{PFR} [s]	τ_{CSTR} [s]	$\tau_{PFR}+\tau_{CSTR}$ [s]	**Average $\tau_{PFR}+\tau_{CSTR}$ [s]**
0.8	2.11 1.36 1.92	11.30 13.50 11.48	13.41 14.86 13.40	**13.89**
1.5	1.81 1.76 2.20	10.71 14.62 8.34	12.52 16.38 10.54	**13.12**
2	2.06 1.40 2.39	12.34 14.11 7.42	14.40 15.51 9.81	**13.24**

The variation of the solids circulation rate, the variation of the FR fluidization and the corresponding simulated values are listed in Table 4-6, Table 4-7 and shown in *Figure 4-5*.

Table 4-6: Simulated residence times for different solids circulation rates (FR = 2 $Nm^3 \cdot h^{-1}$).

AR [$Nm^3 \cdot h^{-1}$]	**Solids circulation rate [$kg \cdot m^{-2} \cdot s^{-1}$]**	τ_{PFR} [s]	τ_{CSTR} [s]	$\tau_{PFR}+\tau_{CSTR}$ [s]	**Average $\tau_{PFR}+\tau_{CSTR}$ [s]**
10	**22.10**	4.66	22.60	27.26	**27.37**
		5.30	20.85	26.15	
		6.20	22.49	28.69	
15	**42.38**	3.39	11.13	14.52	**14.58**
		3.79	11.84	15.63	
		3.66	9.92	13.58	
20	**64.15**	2.83	6.82	9.65	**10.31**
		3.45	7.39	10.84	
		3.59	6.84	10.43	

Table 4-7: Simulated residence times for different solids circulations rates (FR = 4 $Nm^3 \cdot h^{-1}$).

AR [$Nm^3 \cdot h^{-1}$]	**Solid circulation rate [$kg \cdot m^{-2} \cdot s^{-1}$]**	τ_{PFR} [s]	τ_{CSTR} [s]	$\tau_{PFR}+\tau_{CSTR}$ [s]	**Average $\tau_{PFR}+\tau_{CSTR}$ [s]**
10	**20.92**	5.29	20.12	25.41	**24.83**
		4.54	19.51	24.05	
		4.36	20.66	25.02	
15	**42.71**	3.24	9.94	13.18	**14.31**
		3.55	10.57	14.12	
		3.58	12.04	15.62	
20	**60.17**	2.90	6.10	9.00	**9.17**
		3.05	6.44	9.49	
		3.61	5.42	9.03	

For increasing solids circulation rates the residence PFR time decreased, as well as the residence CSTR time but the fraction of the residence PFR time did not proportionally decrease in comparison to the residence CSTR time. The latter showed proportionally higher residence time values for lower solids circulation rates. It can be concluded, that the first appearance time of the particles through the fuel reactor stayed nearly the same for every solids circulation variation. Furthermore, the particles remain longer in the fuel reactor with decreasing solids circulation rates, what would explain the higher fraction of the residence CSTR time. The reciprocal correlation between the residence time and the mass flow according to Levenspiel, 1999 and (4.2) seems to be fulfilled.

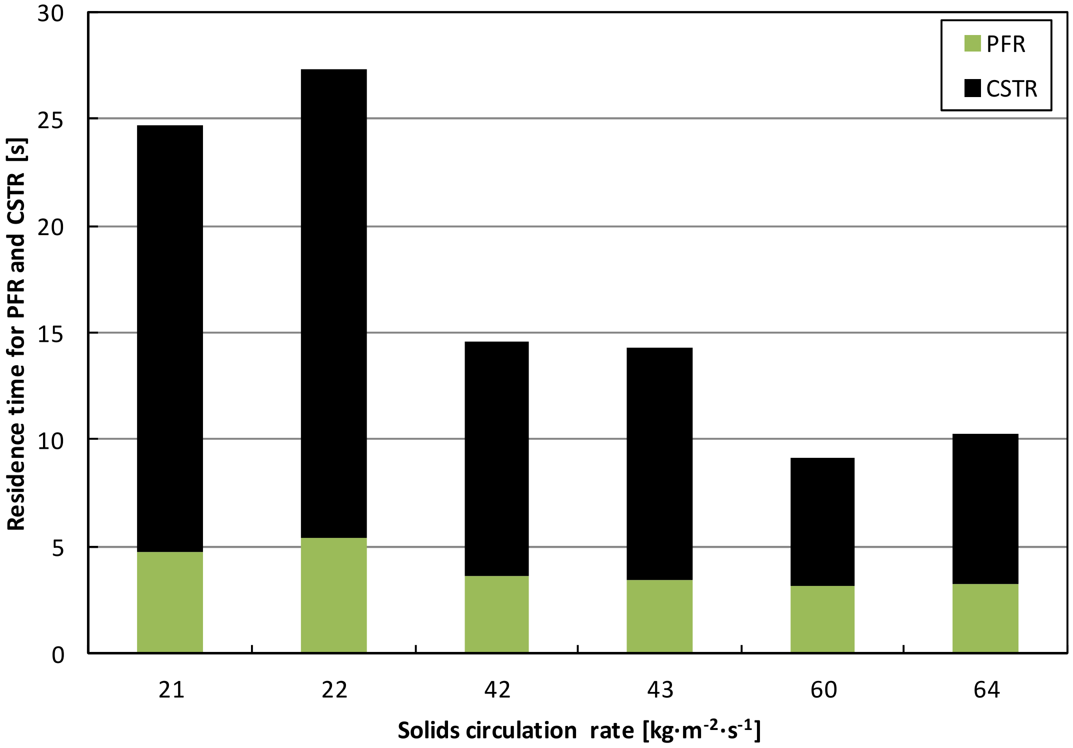

Figure 4-5: Residence PFR and CSTR time for different solids circulation rates.

The variation of the fuel reactor fluidization showed a difference in the residence PFR and CSTR time as well. The calculated residence times are also shown in Table 4-6 and Table 4-7. For the experiments accomplished at the fluidization rate of FR = 4 $Nm^3 \cdot h^{-1}$ of the fuel reactor, the simulated residence time values for each reactor were lower than for the experiments performed at the fluidization rate of FR = 2 $Nm^3 \cdot h^{-1}$ (*Figure 4-6*). This can be explained by the lower particle mass in the fuel reactor for the former experiments, as discussed in Chapter 4.2.

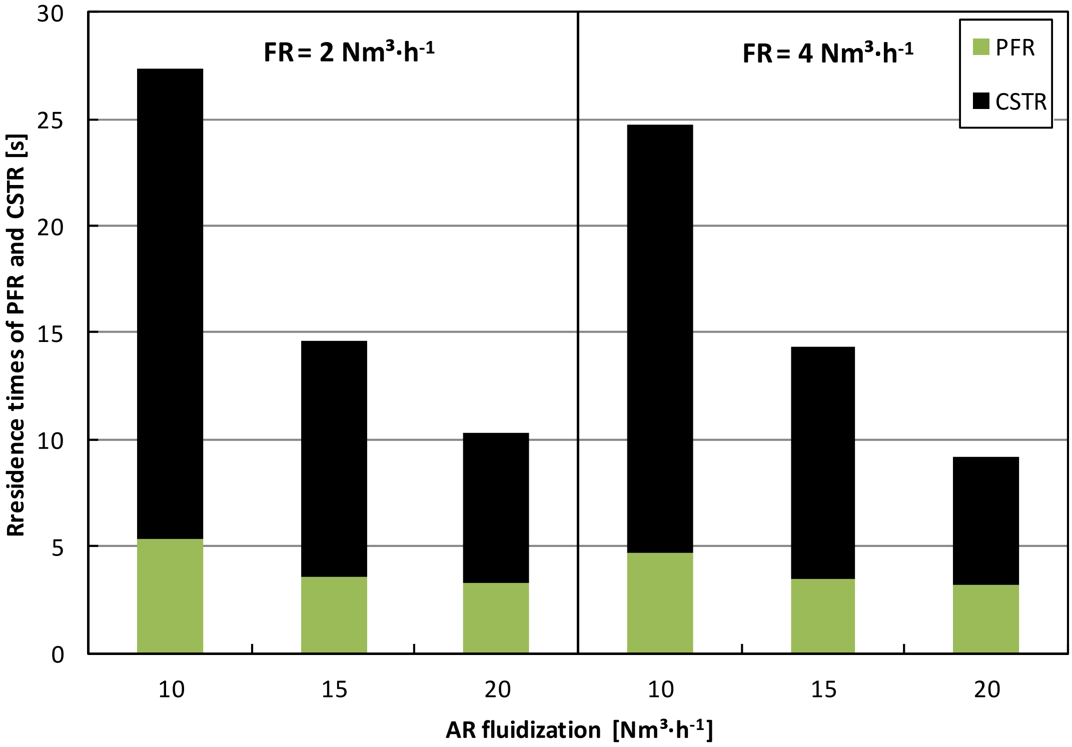

Figure 4-6: Residence PFR and CSTR at different solids circulation rates (AR fluidization) and two different FR fluidization rates.

5 CONCLUSIONS AND OUTLOOK

A study of the dependence of the mean particle residence time in the fuel reactor on three different variables has been accomplished:

- ULS fluidization velocity.
- Global solids circulation rate.
- Fuel reactor fluidization velocity.

In addition a PFR and CSTR connection in series model was correlated to the measured signals and the mean residence time of these ideal reactors was investigated as well.

The study was started with the variation of the ULS fluidization velocity. This variation had no significant influence on either of the mean residence time or the variance of the measured LLS signals. Whereas at a higher fluidized ULS, the variances of the measured signals were increasing likely due to the higher turbulences in the ULS.

The variation of the solids circulation rate had an influence on the residence time: With increasing solids circulation rate, the mean residence time decreased. This agrees with theory. The lower the circulation rates, the higher were the variances of the obtained signals, maybe due to the less homogeneous particle flow through the loop seals.

When the fluidization rate of the FR was increased the mean residence time decreased. It was found that the mass of the particles in the fuel reactor was smaller and thus the residence time decreased. The variances of the input signals showed no significant difference for each variation as expected. Whereas the variances of the signals in the LLS for the higher fluidized fuel reactor took smaller values. It is concluded that particle mixing was improved for the higher fluidization velocity.

The vessel dispersion number (VDN) for each fluidization variation was determined as well. The ULS fluidization variation had no significant influence on it. With increasing solids circulation rates the flow pattern slightly tends to the plug flow model. For the experiments carried out at the lower fluidization velocities of the fuel reactor the VDN showed in general higher values, in contrast to higher fluidization velocities. The increment of the bed mass in the fuel reactor for decreasing fluidization velocities as mentioned above could have lead to higher particle dispersion in the fuel reactor and to higher values of the vessel dispersion number.

The input signals were provided to a simulation model, especially designed for this purpose, which calculated the corresponding output signal based on an assumed configuration of ideal models (connection in series of a PFR and a CSTR). It was found that the model describes the system very well for the conditions studied.

Further investigations need to be done to find out the influence of the secondary loop (internal loop) on the residence time of the fuel reactor.

6 BIBLIOGRAPHY

- Avidan, A., Yerushalmi, J. (1985), Solids Mixing in an Expanded Top Fluid Bed, AIChE Journal, Vol 31, pp. 835-841
- Guío-Pérez, D.C., Marx, K., Pröll, T., Hofbauer, H., (2011), Fluid dynamic affects of ring-type internals in a dual circulating fluidized bed system, In: Proceedings of the 10th International Conference on Circulating Fluidized Beds, Sunriver Resort, Oregon, USA.
- Glicksman, L.R. (1984), Scaling Relationships for fluidized beds, Chemical Engineering Science, Vol 39, pp. 1373 - 1379
- Goldblatt, W.M. (1990), Electromagnetic induction sensing of individual tracer particles in a circulating fluidized bed, Chemical Engineering Department of british colombia university
- Grace, J.R., Avidan, A.A., Knowlton, T.M. (1997), Circulating Fluidized Beds, Chapman & Hall
- Harris, A. T., Davidson, J. F., Thorpe, R. B. (2002), A novel method for measuring the residence time distribution in short time scale particulate systems, Chemical Engineering Journal, Vol 89, pp. 127-142
- Harris, A. T., Davidson, J. F., Thorpe, R. B. (2003), Particle residence time distributions in circulating fluidised beds, Chemical Engineering Science, Vol 58, pp. 2181-2202
- Kolbitsch, P. (2009), Chemical looping combustion for 100% carbon capture - Design, operation and modeling of a 120kW pilot rig, Vienna University of Technology
- Kunii, D., Levenspiel, O. (1991), Fluidization Engineering, Butterworth-Heinemann
- Levenspiel, O. (1999), Chemical reaction engineering, John Wiley & Sons
- Li, Y., Kwauk, M. (1980), the dynamics of fast fluidization, Fluidization III, pp. 537 - 544
- Mahmoudi, S., Seville, J. P. K., Baeyens, J. (2010), The residence time distribution and mixing of the gas phase in the riser of a circulating fluidized bed, Powder Technology, Vol 203, pp. 322-330
- Nauman, E.B. (2008), Chemical reactor design, optimization, and scaleup, John Wiley & Sons
- Reh, L. (1971), Fluidized Bed Processing, Chemical Engineering Progress, Vol 67, pp. 58-63
- Rupanovits, K. (2007), Auslegung, Aufbau und fluiddynamische Untersuchungen an einem Wirbelschicht -Kaltmodell für Chemical Looping Prozesse, Vienna University of Technology
- Smolders, K., Baeyens, J. (2000), Overall solids movement and solids residence time distribution in a CFB-riser, Chemical Engineering Science, Vol 55, pp. 4101-4116
- Pröll, T., Todinca, T., Şuta, M., Friedl, A. (2007), Acid gas absorption in trickle flow columns – Modelling of the residence time distribution of a pilot plant, Chemical Engineering and Processing, Vol 46, pp. 262-270

Westphalen, D., Glicksman, L. (1995), Lateral Solid Mixing Measurements in Circulating Fluidized-Beds, Powder Technology, Vol 82, pp. 153-167

7 NOTATION

Abbreviations

AR	air reactor
CFB	circulating fluidized bed
CFM	cold flow model
CLC	chemical looping combustion
CSTR	continuous flow stirred tank reactor
FR	fuel reactor
ILS	internal loop seal
LLS	lower loop seal
PFR	plug flow reactor
RTD	residence time distribution
ULS	upper loop seal
VDN	vessel dispersion number

Symbols

A	cross section	[m^2]
B	magnetic flux density	[T]
c, C	concentration	[mol·m^{-3}]
$\boldsymbol{C}$	capacitance	[F]
d, D	diameter	[m]
$\boldsymbol{D}$	axial dispersion coefficient	[m^2·s^{-1}]
$\mathfrak{D}$	molecular diffusions coefficient	[m^2·s^{-1}]
e	electromotive force	[V]
E	electrical field intensity	[V·m^{-1}]
$\boldsymbol{E}$	exit age distribution	[s^{-1}]
F	feed rate	[mol/s]
F	force	[N]
f	frequency	[Hz]
g	gravitation constant (9.81)	[m·s^{-2}]
h, z, s	height, distance	[m]
H	magnetic field intensity	[A·m^{-1}]
$\boldsymbol{I}$	electrical current	[A]
L	inductance	[H]
l, L	length	[m]

M	introduced tracer particles	[kg]
n	amount of substance	[mol]
Q	charge carriers	[C]
p	pressure	[Pa]
P	specific resistance of a conductor material	[$\Omega\cdot mm^2\cdot m^{-1}$]
r	rate of reaction	[-]
R	electrical resistance	[Ω]
t	time	[s]
$\bar{t}$	centre of area at time $\bar{t}$	[s]
u	velocity	[$m\cdot s^{-1}$]
U	electric tension	[V]
U	superficial velocity	[$m\cdot s^{-1}$]
$u_S(t)$	signal voltage	[V]
$u_T(t)$	carrier frequency voltage	[V]
$u_M(t)$	modulator output voltage	[V]
$u_U(t)$	demodulator transfer function	[V]
$u_D(t)$	output voltage of demodulator	[V]
V	volume	[m^3]
$\dot{V}$	volumetric flow	[$m^3\cdot s^{-1}$]
X	conversion	[-]
X_L	inductive reactance	[$H\cdot s^{-1}$]
$\underline{Z}$	impedance	[-]

Greek symbols

δ	Dirac delta function	[-]
ε	voidage	[-]
η	dynamic viscosity	[$kg\cdot m^{-1}\cdot s^{-1}$]
μ	magnetic permeability	[$H\cdot m^{-1}$]
μ_0	magnetic constant ($4\cdot\pi\cdot 10^{-7}$)	[$H\cdot m^{-1}$]
μ_r	relative permeability	[-]
ρ	density	[$kg\cdot m^{-3}$]
σ^2	variance	[s^2]
τ	space-time, mean residence time	[s]
Φ, Φ	magnetic flux	[Wb]
Ψ	sphericity	[-]

Subscripts

A	tracer A
B	bed
c	conductor
e	exit
G, g	gas
i	in
o	out
P, p	particle
r	relative
R	reactor
s	solid
S	signal
x	measured
$\theta = \frac{t}{\tau}$	dimensionless time unit

APPENDIX

A: Examples of signal curves of different experiments

The signal curves of five different fluidization conditions are graphically represented, according to the four signal processing steps described in Chapter 3.6.4:

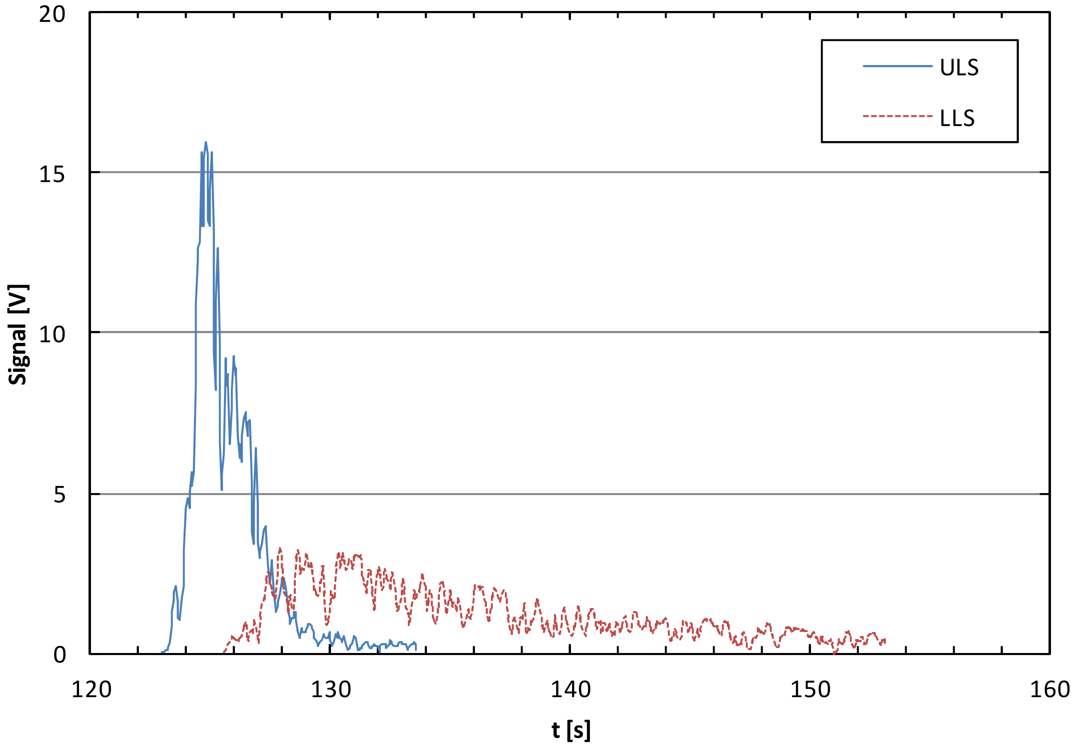

Section of the injection and LLS signal curves of the variation of the ULS fluidization (AR = 20 Nm³/h, FR = 15 Nm³/h, LLS = 1 Nm³/h, ILS = 0.75 Nm³/h, ULS = 1.5 Nm³/h).

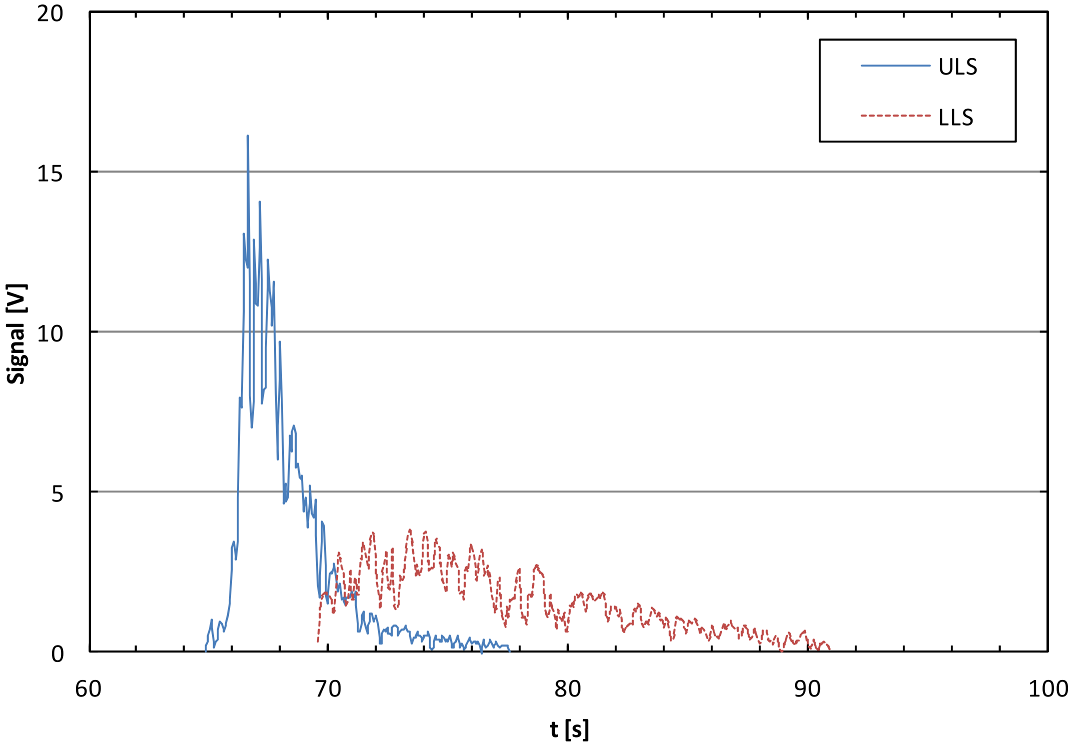

Section of injection and LLS signal curves of the variation of the solids circulation rate (AR = 20 Nm³/h, FR = 2 Nm³/h, ULS and LLS = 1 Nm³/h, ILS = 0 Nm³/h).

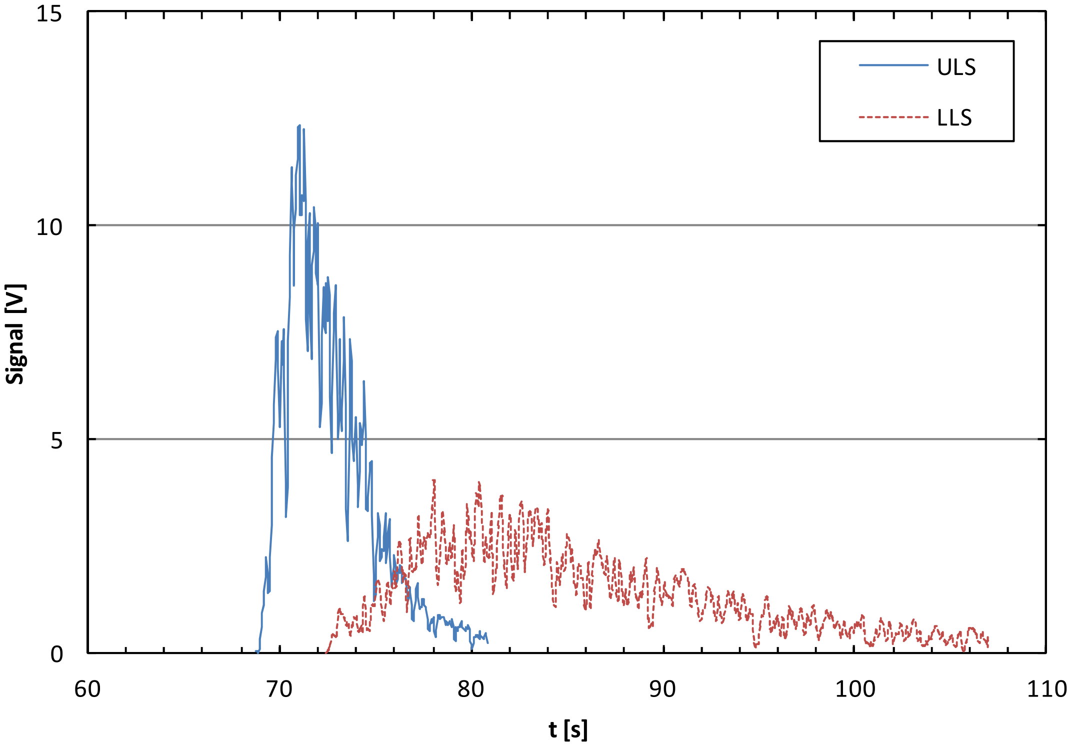

Section of the injection and LLS signal curves of the variation of the solids circulation rate (AR = 15 Nm³/h, FR = 2 Nm³/h, ULS and LLS = 1 Nm³/h, ILS = 0 Nm³/h).

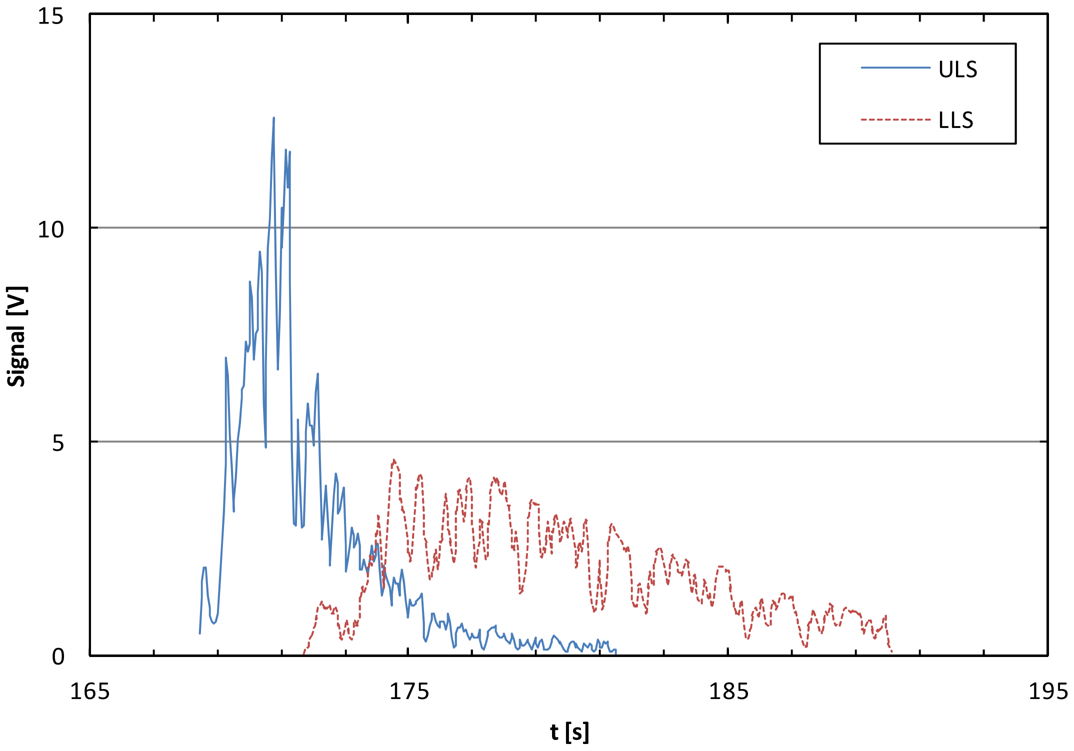

Section of the injection and LLS signal curves of the variation of the solids circulation rate (AR = 20 Nm³/h, FR = 4 Nm³/h, ULS and LLS = 1 Nm³/h, ILS = 0 Nm³/h).

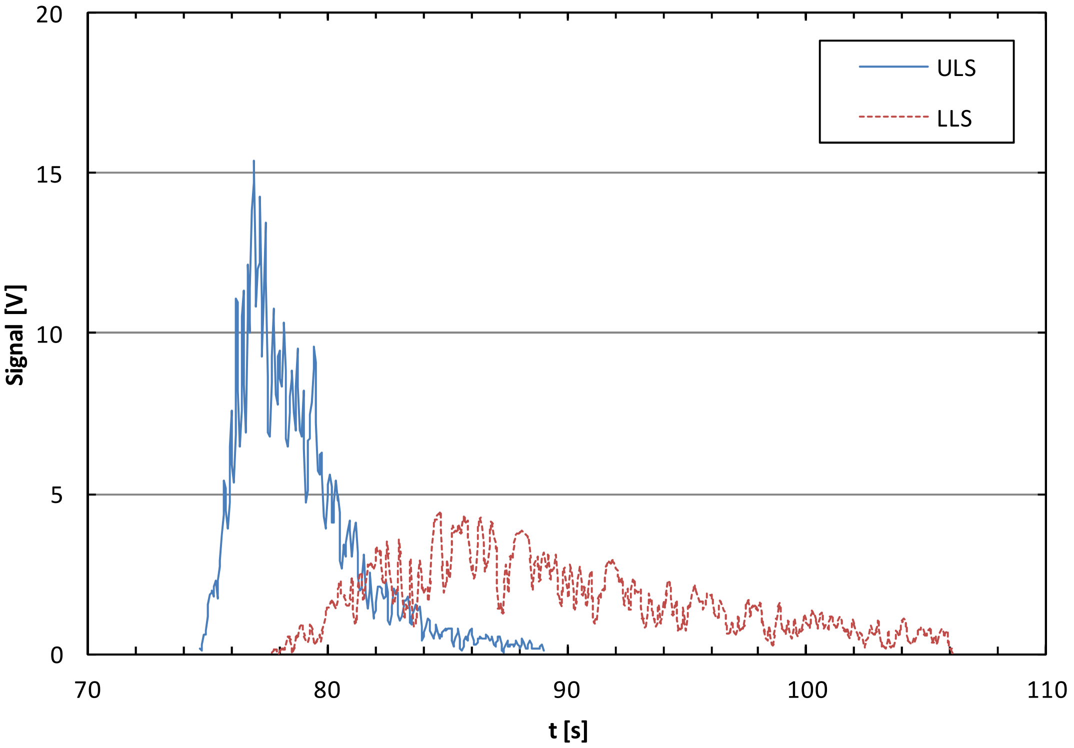

Section of the injection and LLS signal curves of the variation of the solids circulation rate (AR = 15 Nm³/h, FR = 4 Nm³/h, ULS and LLS = 1 Nm³/h, ILS = 0 Nm³/h).

B: Examples of simulated output curves

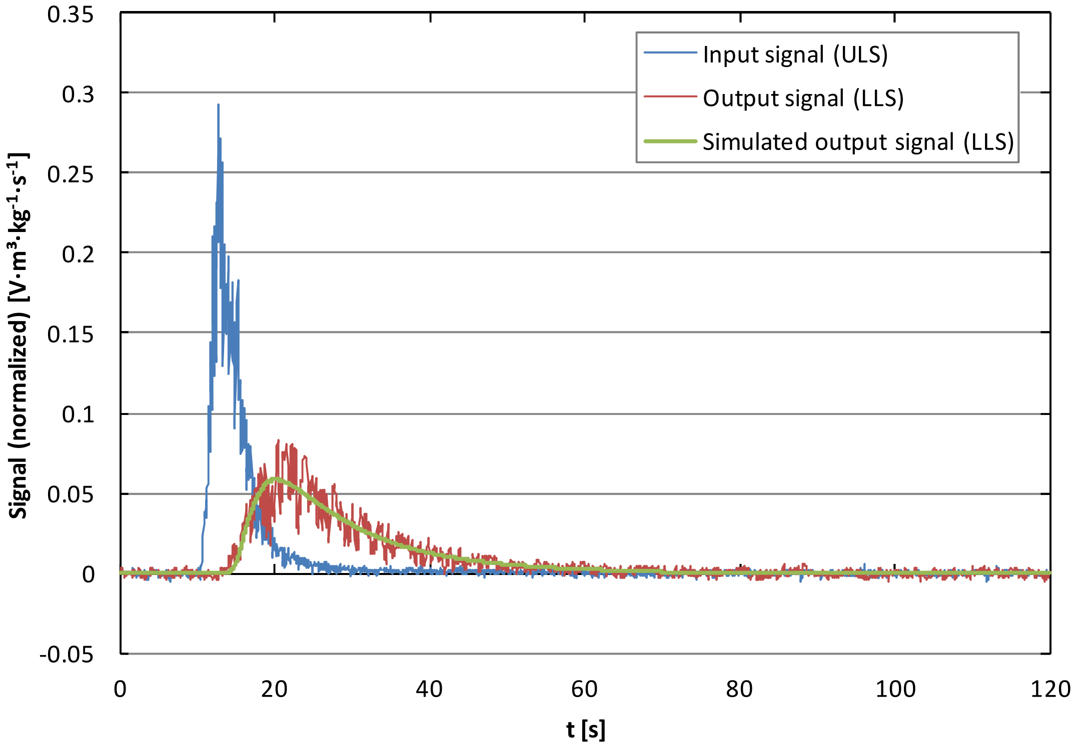

Simulated output curve and the corresponding measured input and output curves (AR = 15 Nm³/h, FR = 4 Nm³/h, ULS and LLS = 1 Nm³/h, ILS = 0 Nm³/h).

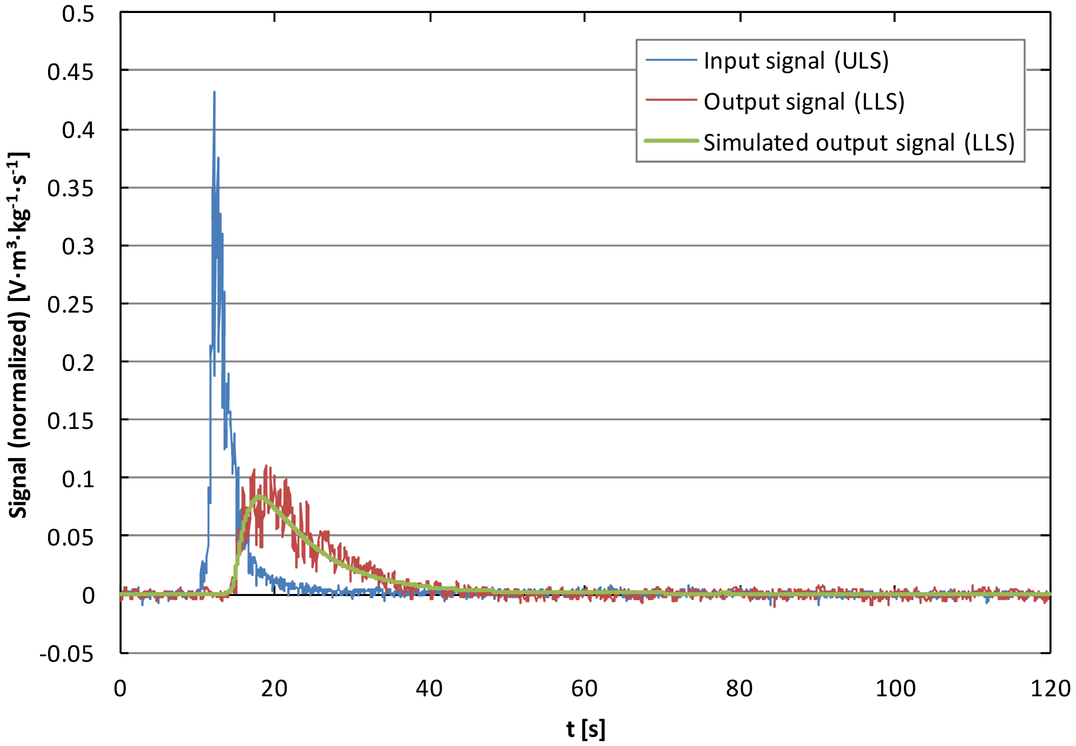

Simulated output curve and the corresponding measured input and output curves (AR = 20 Nm³/h, FR = 2 Nm³/h, ULS and LLS = 1 Nm³/h, ILS = 0 Nm³/h).

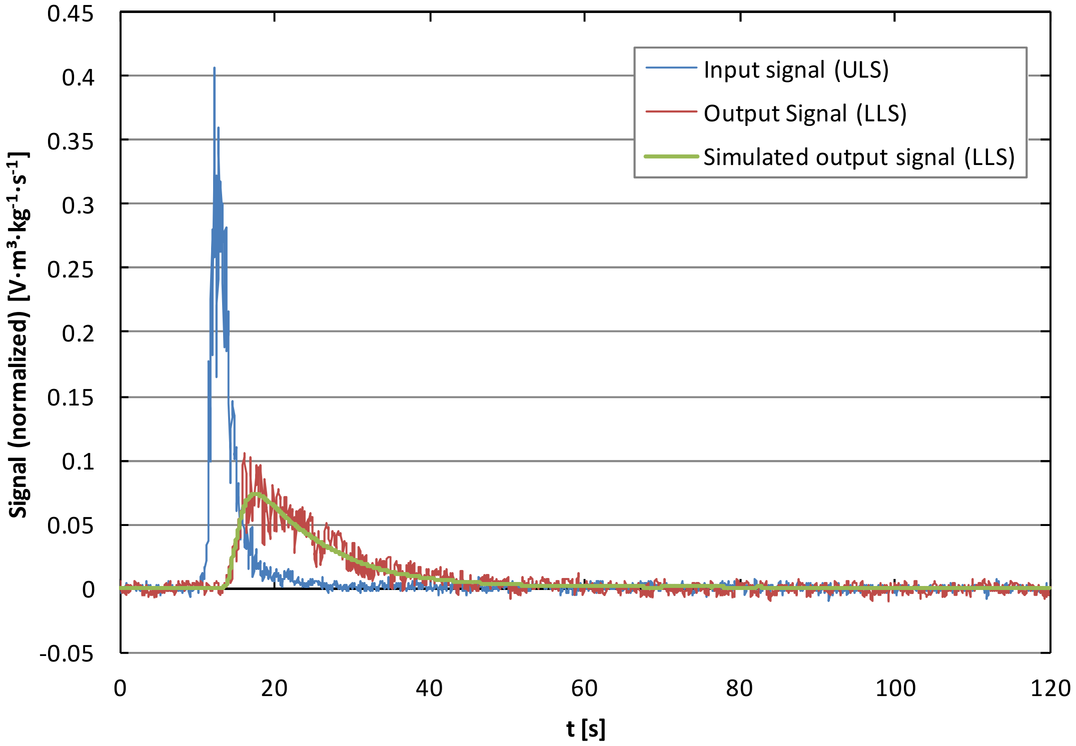

Simulated output curve and the corresponding measured input and output curves (AR = 15 Nm³/h, FR = 2 Nm³/h, ULS and LLS = 1 Nm³/h, ILS = 0 Nm³/h).

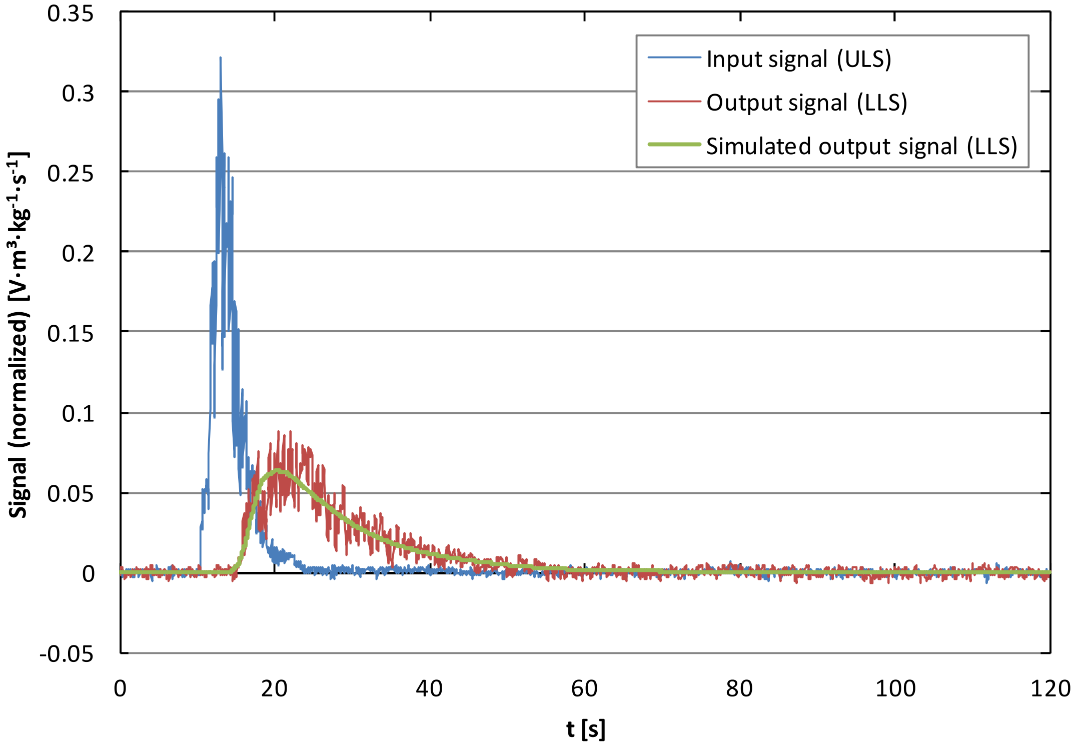

Simulated output curve and the corresponding measured input and output curves (AR = 20 Nm³/h, FR = 15 Nm³/h, ULS = 1.5 Nm³/h, LLS = 1 Nm³/h, ILS = 0.75 Nm³/h).